



저작자표시-비영리-변경금지 2.0 대한민국

이용자는 아래의 조건을 따르는 경우에 한하여 자유롭게

- 이 저작물을 복제, 배포, 전송, 전시, 공연 및 방송할 수 있습니다.

다음과 같은 조건을 따라야 합니다:



저작자표시. 귀하는 원저작자를 표시하여야 합니다.



비영리. 귀하는 이 저작물을 영리 목적으로 이용할 수 없습니다.



변경금지. 귀하는 이 저작물을 개작, 변형 또는 가공할 수 없습니다.

- 귀하는, 이 저작물의 재이용이나 배포의 경우, 이 저작물에 적용된 이용허락조건을 명확하게 나타내어야 합니다.
- 저작권자로부터 별도의 허가를 받으면 이러한 조건들은 적용되지 않습니다.

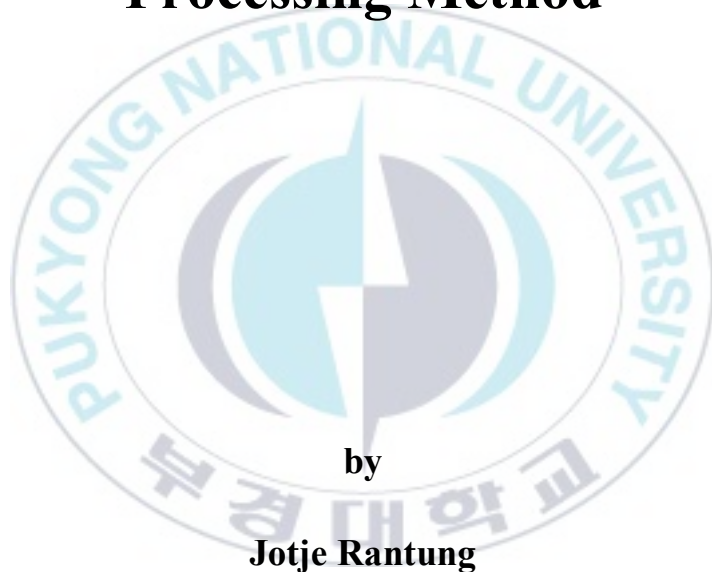
저작권법에 따른 이용자의 권리는 위의 내용에 의하여 영향을 받지 않습니다.

이것은 [이용허락규약\(Legal Code\)](#)을 이해하기 쉽게 요약한 것입니다.

[Disclaimer](#)

**Thesis for the Degree of Doctor of Philosophy**

**A Measurement Method for Fish  
Surface Area and Volume Based on  
3D-Coordinate Using Image  
Processing Method**



by

**Jotje Rantung**

**Department of Mechanical Design Engineering**

**The Graduate School**

**Pukyong National University**

**August 2019**

**A Measurement Method for Fish  
Surface Area and Volume Based on  
3D-Coordinate Using Image  
Processing Method**

**영상처리법을 이용한 3D 좌표기반 어류**

**표면적 및 부피 측정법**

by

**Jotje Rantung**

**Advisor: Prof. Sang Bong Kim**

**A thesis submitted in partial fulfillment of the requirements for  
the degree of Doctor of Philosophy**

**In Department of Mechanical Design Engineering,  
The Graduate School,  
Pukyong National University**

**August 2019**

**A Measurement Method for Fish Surface Area and  
Volume based on 3D-Coordinate Using Image  
Processing Method**

**A dissertation  
by  
Jotje Rantung**


Approved as to styles and contents by:



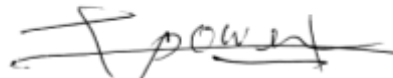
**(Chairman) Yeon Wook Choe**



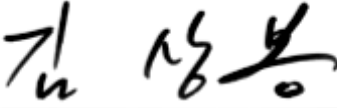
**(Member) Young Bok Kim**



**(Member) Jin Ho Suh**



**(Member) Ill Yeong Lee**



**(Member) Sang Bong Kim**

May 22, 2019

# Acknowledgments

First and foremost, I would like to express my deepest appreciation to my thesis advisor, Professor Sang Bong Kim, whose inspiration, support and perseverance made this dissertation become possible. For the past few years, Prof. Kim has been the advisor, mentor and guardian to me. His insight, suggestions and instructions helped me to establish the direction of my research, and finish this thesis. Furthermore, he also provided excellent equipment for my experiments. I will always cherish these years in CIMEC Lab with his leading.

I would like to thank the members of my thesis committee: Prof. Yeon Wook Choe, Prof. Yeon Bok Kim, Prof. Ill Yeong Lee, and Prof. Jin Ho Suh who have provided wonderful feedback on my work and great suggestions for better contribution of my dissertation.

I would like to thank Prof. Hak Kyeong Kim for his great helps and advice to research and complete this dissertation. I could not finish my dissertation on time without his great help and advice.

I would like to thank all members of CIMEC Lab. for giving me a comfortable and active environment to achieve my work: Dr. Dae Hwan Kim, Dr. Huy Hung Nguyen, Mr. Minh Thien Tran, Mr. Jong Min Oh, Mr. Chang Kyu Kim, Mr. Lanh Van Nguyen, Mr. Sung Won Kim, Mr. Chetan Chunilal Patel, Mr. Sung Rak Kim, Mr. Dong Yong Kim, Miss Jeong Lim Son, and all other foreign friends.

Finally, I would like to thank to my wife, Grace Lumingkewas, my sons, Gabriel Yosua Rantung and Gideon David Rantung, and all my close relatives support for me not only in the dissertation time but also

in the whole of my life. And lastly, thank you to all the people who cannot be mentioned here for the help and support.

Pukyong National University, Busan, Korea

May 22, 2019

Jotje Rantung



# Contents

Acknowledgments.....	i
Contents .....	iii
Abstract .....	vii
국문요약서 .....	x
List of Figures.....	xiii
List of Tables .....	xvii
Nomenclatures.....	xviii
<b>Chapter 1: Introduction .....</b>	<b>1</b>
1.1 Background and motivation .....	1
1.2 Objective and researching method.....	10
1.3 Problem statements .....	11
1.4 Outline of dissertation and summary of contributions.....	11
<b>Chapter 2: Mathematical Modeling and Image Processing Methods.....</b>	<b>14</b>
2.1 Mathematical modeling to measure fish surface area and volume.....	15
2.1.1 Analytical method .....	15
2.1.2 Partition method applied for an image processing method .....	24
2.2 Image processing methods .....	32
2.2.1 Pre-processing of image .....	32

2.2.2	Region labelling .....	33
2.2.3	Binary morphology.....	34
2.2.4	Image edge detection.....	39
2.3	Stereo camera .....	43
2.3.1	Pinhole camera model .....	43
2.3.2	Extrinsic camera parameters.....	45
2.3.3	Intrinsic camera parameters.....	46
2.3.4	Two pinhole camera model.....	47
2.4	Moving object tracking with Kalman filter.....	51
2.4.1	Typical Kalman filter .....	51
2.4.2	Multi-object tracking using Kalman filter .....	54
<b>Chapter 3: System Description.....</b>		<b>58</b>
3.1	Structure hardware of a proposed analytic and partition measurement methods.....	58
3.2	Structure hardware of a proposed real-time measurement method.....	60
3.3	Structure hardware of a proposed real-time measurement method for moving objects.....	62
<b>Chapter 4: Analytic and Partition Measurement Method for Fish Surface Area and Volume.....</b>		<b>64</b>
4.1	Data acquisition .....	65
4.1.1	Image acquisition .....	66
4.1.2	Image calibration.....	67
4.2	Image processing and analysis .....	70

4.2.1	Preprocessing .....	71
4.2.2	Image segmentation and feature extraction .....	72
4.3	Experimental results.....	75
4.3.1	Image segmentation results.....	75
4.3.2	Contour extraction and region filling .....	78
4.3.3	Surface area and volume calculations .....	81
4.4	Summary .....	83
<b>Chapter 5: Real-time Measurement Method for Fish Surface Area and Volume .....</b>		<b>84</b>
5.1	Camera calibration.....	84
5.1.1	Calibration intrinsic parameter of camera .....	89
5.2	Real-time image segmentation method for fish surface area and volume measurement.....	90
5.2.1	Related work .....	90
5.2.2	Proposed real-time image segmentation method .....	92
5.2.3	Experimental results of real-time image segmentation.....	94
5.3	3D coordinate measurement using stereo camera .....	101
5.3.1	3D Measurement principle.....	102
5.3.2	Distance measurement of an object between stereo camera .....	106
5.3.3	System setup .....	112
5.3.4	Experimental results of fish surface area and volume measurement based on 3D coordinate.....	118
5.4	Summary .....	122

<b>Chapter 6: Real-time Measurement Method of Moving Objects for Fish Surface Area and Volume.....</b>	<b>124</b>
6.1 Proposed measurement method in real-time for moving object.....	124
6.1.1 Real-time image segmentation for moving object detection .....	129
6.1.2 Object classification .....	131
6.1.3 Tracking contour of a moving object .....	132
6.1.4 3D coordinate measurement of a moving object.....	134
6.2 Experimental results for moving objects.....	135
6.2.1 Experimental results of real-time image segmentation .....	135
6.2.2 Experimental results of tracking contour.....	137
6.2.3 3D coordinate measurement results of moving objects .....	139
6.3 Summary .....	141
<b>Chapter 7: Conclusions and Future Works.....</b>	<b>143</b>
7.1 Conclusions .....	143
7.2 Future works.....	148
<b>References .....</b>	<b>149</b>
<b>Publication and Conference .....</b>	<b>159</b>
<b>Appendix A. The proof of Eq. (2.10) ~ Eq. (2.19).....</b>	<b>162</b>
<b>Appendix B. The proof of Eq. (2.21).....</b>	<b>167</b>
<b>Appendix C. The proof of Eq. (2.32).....</b>	<b>169</b>

**A Measurement Method for Fish Surface Area and Volume Based on  
3D-Coordinate Using an Image Processing Method**

**Jotje Rantung**

**Department of Mechanical Design Engineering,  
The Graduate School, Pukyong National University**

**Abstract**

The fish processing industry requires technological solutions that focus on automating the processing task to increase production, and reduce time and costs. In the fish processing industry, measuring the surface area and volume of fish is an important step in the whole process. The technology advances in an image processing method enables the application of new techniques to measure surface area and volume of fish precisely, fast and accurately.

This dissertation presents a measurement method for fish surface area and volume based on 3D-coordinate using an image processing method. Three measurement methods for fish surface area and volume in this dissertation are proposed: an analytic method and a partition measurement method for fish surface area and volume, a real-time measurement method for fish surface area and volume, and a real-time measurement method of moving objects for fish surface area and volume. To do this task, the followings are done.

Firstly, the overview of the measurement methods proposed in this dissertation is provided. This dissertation presents mathematical modeling useful for calculating fish surface area and volume, reviewing image processing methods, stereo camera and moving object tracking. For mathematical modeling, the fish shape is considered to be ellipsoidal. Mathematical modeling consists of an analytic method and a partition method applied for image processing to measure fish surface area and volume. The image processing methods used for this dissertation are focusing on image segmentation by using mathematical morphology and edge detection. The

pinhole camera model is adopted to define the modeling of stereo triangulation for obtaining camera parameters. For moving object tracking, Kalman filter for multi-object tracking is presented.

Secondly, the structure hardwares of the measurement systems used for the above three measurement methods for measuring fish surface area and volume are presented as follows: the measurement system on analytic and partition measurement methods for fish surface area and volume, the measurement system on real-time measurement method for fish surface area and volume, and the measurement system on real-time measurement method of moving object. The structure hardwares are developed with mechanical and electrical parts such as personal computer (PC), monitor screen, LED lamp, HD camera, stereo camera, frame, fixed or moving plywood panel, etc.

Thirdly, an analytic and partition measurement methods for fish surface area and volume are proposed. The measurement method is implemented in offline. The image processing method is built in Matlab programming language. The images are captured by using high density (HD) camera to acquire digital profile images used for image acquisition. The digital profile images are extracted as segmented image and used for measuring fish surface area and volume. The actual length, height, and width of the fish in millimeters are measured. These are used to calibrate the length, height, and width in pixels of a feature extracted from the profile digital image of the fish. Camera calibration constant, image preprocessing, image segmentation and feature extraction are utilized in the algorithm to calculate the fish surface area and volume. The measurement results of the fish surface area and volume of the partition method is compared with those of the analytic method to prove its validity.

Fourthly, a real-time measurement method for fish surface area and volume is proposed. It is shown that the proposed partition measurement method using image processing methods is valid because the difference between experimental results using an image processing method and analytical method was small. However, this method is built in offline. The main problems of an image captured by the video camera result in excessive information, complex disparities, and the change of the shape and appearance of an object due to lighting conditions. Therefore, a method to extract the foreground object image is needed to solve these problems. A real-time

image segmentation method is proposed to solve these problems. To execute this tasks, a stereo camera is used. The real-time image segmentation is developed by using library available in open source computer vision (OpenCV, C++). The real-time image segmentation is done by combining HSV color space, threshold value, mathematical morphological transformations, and contour detection techniques to extract objects in a graph-based image. A 3D coordinate measurement of fish surface area and volume by using stereo camera is used. By using the 3D coordinate measurement, the length, width, and height (mm) of the fish image are obtained. Fish surface area and volume are calculated from the length, width, and height of the fish image.

Fifthly, a real-time measurement method of moving objects for fish surface area and volume is proposed. In this method, an object is moving on a moving plywood panel driven offline by a motor and a stereo camera determines the size of the object. The real-time image segmentation of moving objects is developed by using library available in open source computer vision (OpenCV, C++). To determine the size of objects which cannot be contained within the camera field of view, it is useful to track their contours. To complete this task, the following steps are done. The first step is that the segmented object is shown in the target view. The second step is that each image is classified and stored in computer as image library. The third step is that a stereo camera automatically identifies the targeting object by matching the two views of the contour. The final step is to reposition the stereo camera at the reference position relative to the planar contour, and measure the object centroid and the object size.

Finally, the experimental results are shown to verify the effectiveness and applicability of the proposed three measurement methods.

**Keywords:** Image processing, Image segmentation, Real-time image segmentation, Stereo camera, 3D coordinate measurement, Fish surface area calculations, Fish volume calculations, Moving object.

# 영상처리법을 이용한 3D 기반 어류표면적 및 부피 측정법

조제 란통

부경대학교 대학원 기계설계학과

국문요약서

오늘날, 어류공정산업은 생산증가, 시간과 비용감소를 하기 위한 공정을 자동화하는 것에 중점을 둔 기술적 해결책을 요구한다. 어류공정산업에서는 어류의 표면적과 부피를 측정하는 것이 전공정에 있어서의 중요한 단계이다. 영상처리법에 있어서의 기술진보는 어류의 표면적과 부피를 정밀하고 빠르고 정확하게 측정하는 새로운 기술의 응용을 가능하게 한다.

본 연구는 영상처리법을 이용한 3D 좌표기반 어류 표면적 및 체적 측정법을 제시한다. 이를 위해 다음과 같이 수행한다. 본 연구에서는 어류 표면적과 부피측정을 위해 다음과 같은 세가지 측정법이 제시된다-해석적 측정법과 분할측정법, 실시간 측정법과 이동물체의 실시간 측정법. 이를 위해 다음과 같이 수행한다.

첫째, 본 연구에서 제시된 측정법들에 사용된 수학적 모델링과 영상처리법에 대한 개요가 제시된다. 본 연구는 어류표면적 및 부피계산에 사용되는 수학적 모델링, 영상처리법의 검토, 스테레오카메라의 모델링과 이동물체 추적법이 제시된다. 먼저 어류모양을 타원체형이라 간주한 수학적 모델링이 제시된다. 어류표면적과 체적을 측정하기 위한 영상처리에 적용된 수학적 모델링은 해석적 측정법과 분할측정법으로 구성된다. 영상처리법은 수학적 형태학과 에지탐지를 사용한 영상분할에 집중하고 있다. 핀홀 카메라모델이 카메라 매개변수들을 얻기 위하여 스테레오 삼각법의 모델링을 정의하기 위해 채용된다. 이동 다물체를 추적을 위해 칼만필터가 제시된다.

둘째, 본 연구에 사용되는 어류 표면적과 부피측정용 세가지 측정시스템의 하드웨어구조들이 다음과 같이 제시된다-해석적 측정법과 분할 측정법을 위한 측정시스템들,

실시간 측정법을 위한 측정시스템, 이동물체의 실시간 측정법을 위한 측정시스템. 하드웨어 구조는 컴퓨터, 모니터, LED 램프, HD 카메라, 스테레오카메라, 프레임, 고정 또는 이동 목판 패널 등으로 기구적 및 전기적 부품으로 구성된다.

셋째, 어류 표면적과 부피를 측정하기 위한 오프라인으로 측정되는 해석적 측정법과 분할 측정법이 제시된다. 고밀도(HD)카메라를 사용해 얻어진 디지털 프로파일 영상들이 분할영상으로 추출되며 어류표면적과 부피측정에 사용된다. mm 로 측정된 어류의 실제길이, 높이, 폭은 디지털 프로파일 영상으로부터 추출된 형상의 픽셀로 된 길이, 높이, 폭을 교정하기 위해 사용된다. 카메라 교정상수, 영상처리, 영상분할과 형상추출이 어류표면적과 부피를 계산하기 위한 알고리즘에 사용된다. 어류표면적과 부피에 대한 분할 측정법에 의한 측정결과가 그 유효성을 증명하기 위해 해석적 측정법에 의한 측정결과들과 비교된다.

넷째, 어류표면적과 부피에 대한 실시간 측정법이 제시된다. 영상처리법을 사용한 제안된 분할 측정법과 해석적 측정법을 사용한 실험결과들의 차이가 작기때문에 제안된 분할 측정법이 유효함을 보여준다. 이 측정법 또한 오프라인으로 만들어져 있으며 비디오 카메라에 의해 얻어진 영상의 주된 문제들은 과도한 정보, 복잡한 불균형, 빛의 조건에 기인한 물체의 형태와 외관모양의 변화를 낳는다. 그러므로 이러한 문제들을 해결하기 위해 전경 물체영상을 추출하는 법이 필요하며 실시간 영상분할법이 제시된다. 이러한 일을 수행하기 위해 스테레오카메라가 사용된다. OpenCV 에서 이용할 수 있는 라이브러리를 사용함으로써 실시간 영상분할이 수행된다. 실시간 영상분할은 HSV 칼라공간, 문턱값, 수학적 형태학적 변환들과 그래프기반 영상에서의 목적물들을 추출하기 위해 윤곽탐지기술들을 결합함으로써 수행된다. 스테레오카메라를 사용하여 어류 표면적과 부피를 측정하기 위해 3D 좌표측정이 사용된다. 3D 좌표측정법을 사용해 mm 로 얻어진 어류영상의 길이, 폭, 높이로 어류표면적과 부피가 계산된다.

다섯째, 어류 표면적과 부피를 측정하기 위한 이동물체의 실시간 측정법이 제시된다. 물체는 모터에 의해 오프라인으로 구동되는 이동 목판 패널 위에서 이동된다. OpenCV 에서 이용할 수 있는 라이브러리를 사용함으로써 이동물체의 실시간 영상분할이 수행된다. 카메라 뷰(영상) 내에 포함될 수 없는 물체들의 크기를 결정하기 위해, 그들의 윤곽들을 추적하는 것이 유용하다. 이를 위해 다음과 같은 단계들이 수행된다. 첫 번째 단계는 분할된 물체가 목표 뷰

안에 보이는 것이다. 두 번째 단계는 각 영상이 분리되어 영상 라이브러리로서 컴퓨터 안에 저장되는 것이다. 세 번째 단계는 스테레오카메라가 윤곽의 두 개의 뷰들을 매칭시킴으로써 목표물체를 자동적으로 확인시키는 것이다. 마지막 단계는 스테레오카메라를 평면 윤곽에 상대적인 목표위치에 재위치시키고 물체 도심과 물체크기를 측정하는 것이다. 마지막으로 실험결과들이 제안된 3 개의 측정법의 유효성과 적용가능성을 보여주기 위해 제시된다.

키워드: 영상처리, 영상분리, 실시간 영상분리, 3D 좌표측정, 어류표면적 계산, 어류체적 계산, 이동물체.



## List of Figures

Fig. 1.1 Fish sorting activities performed by human operators with unprotected handling.....	1
Fig. 1.2 A fish plant workers inspecting fish on a conveyor belt .....	2
Fig. 1.3 Image correction.....	7
Fig. 2.1 Ellipsoid model .....	16
Fig. 2.2 ellipsoid at arbitrary orientation .....	18
Fig. 2.3 General standard ellipsoid.....	20
Fig. 2.4 Ellipse and its auxiliary circle .....	20
Fig. 2.5 General ellipsoid partitioned into discs and geometry orientation. ....	26
Fig. 2.6 Partition of left disc $i_1$ and right disc $i_2$ .....	30
Fig. 2.7 Black object pixel with (a) 4-connected and (b) 8-connected neighbours shown in grey. ....	33
Fig. 2.8 Binary image with three labeled objects.....	34
Fig. 2.9 Binary, erosion, and dilation of an image.....	35
Fig. 2.10 Coordinate locations of the black pixels.....	36
Fig. 2.11 Structuring element.....	37
Fig. 2.12 Opening and closing .....	38
Fig. 2.13 A graph and the corresponding cut.....	41
Fig. 2.14 Pinhole camera model.....	44
Fig. 2.15 Two pinhole camera models. ....	48
Fig. 2.16 Triangulation of two pinhole camera models.....	50
Fig. 3.1 Structure hardware of the proposed analytic and partition measurement methods.....	59
Fig. 3.2 Prototype of ZED stereo camera .....	60

Fig. 3.3 Hardware structure of a proposed real-time measurement method.....	61
Fig. 3.4 Hardware structure of the proposed real-time measurement method for moving objects.....	63
Fig. 4.1 Processing step for calculating fish surface area and volume .....	65
Fig. 4.2 Top view and side view of image acquisition.....	67
Fig. 4.3 Fish measured from two sides by using vernier caliper .....	68
Fig. 4.4 Fish image processing results used for image calibration ..	68
Fig. 4.5 Process of forming a resized image.....	71
Fig. 4.6 Flowchart of image segmentation and feature extraction...	73
Fig. 4.7 Results of fish image segmentation shape extraction.....	74
Fig. 4.8 RGB images and HSV images in upview and sideview.....	76
Fig. 4.9 Upview and sideview grayscale images .....	77
Fig. 4.10 Upview and sideview bw images with noise .....	77
Fig. 4.11 Segmented image by edge detection and contour extraction .....	79
Fig. 4.12 Region filling results of the fish image.....	80
Fig. 4.13 Original fish image combined with its contour.....	80
Fig. 5.1 Camera calibration setup (a), and image pattern for calibrating intrinsic parameter (b) .....	86
Fig. 5.2 Set of pairs of close-up RGB images of the checkerboard.	86
Fig. 5.3 Steps of camera calibration.....	87
Fig. 5.4 Image pattern for calibrating intrinsic parameter.....	89
Fig. 5.5 Segmentation of simple objects.....	95
Fig. 5.6 Segmentation of the small object and the large object .....	96
Fig. 5.7 Segmentation of the different shapes of objects .....	97
Fig. 5.8 Segmentation of the fish object with $Th = 255$ .....	99

Fig. 5.9 Segmentation of the fish object with $Th = 126$ .....	99
Fig. 5.10 Segmentation of the fish object with $Th = 0$ and bounding box .....	100
Fig. 5.11 Segmentation of the fish object with $Th = 0$ , bounding box, and graph cut .....	100
Fig. 5.12 Image segmentation results by watershed transformation, threshold value, and the proposed method.....	101
Fig. 5.13 3D measurement principle using stereo camera.....	103
Fig. 5.14 Triangulation of stereo camera model .....	103
Fig. 5.15 Reconstruction of the 3D stereo position.....	104
Fig. 5.16 Object size in function of the distance between the stereo camera and the object .....	106
Fig. 5.17 Schematic representation of a distance estimate with a stereo camera.....	107
Fig. 5.18 Angular aperture of a camera .....	108
Fig. 5.19 Axes and orientation of the ellipse .....	110
Fig. 5.20 Flowchart to determine the 3D coordinate.....	111
Fig. 5.21 Experimental setup of the stereo camera image acquisition system .....	113
Fig. 5.22 Cup target detection.....	114
Fig. 5.23 Fish target detection.....	115
Fig. 5.24 Flowchart to calculate fish surface are and volume. ....	117
Fig. 5.25 Representation of the right camera and left camera .....	118
Fig. 6.1 Examples of the sequence of stereo camera image frames. .....	126
Fig. 6.2 Flowchart of the proposed moving object detection and measurement algorithm.....	128
Fig. 6.3 Image segmentation and contour detection.....	130

Fig. 6.4 Flowchart of the object classification. .... 131

Fig. 6.5 3D coordinate measurement technique of moving object 134

Fig. 6.6 Sample fish image made for segmented in stereo camera  
frame ..... 136

Fig. 6.7 Experimental results of tracking contour using stereo camera  
..... 138

Fig. A.1 General standard ellipsoid and its auxiliary circle ..... 162

Fig. A.2 Ellipse and its auxiliary circle of (Y,Z) coordinate ..... 163

Fig. A.3 Ellipse and its auxiliary circle of (X,U) coordinate..... 163



## List of Tables

Table 4.1 Algorithm to perform fish surface area and volume calculations using Matlab.....	69
Table 4.2 Results of surface area and volume of four fishes.....	82
Table 5.1 Calibration results of the intrinsic camera parameter. ....	90
Table 5.2 Image coordinate of the centroid point .....	120
Table 5.3 Measurement data of 3D coordinate. ....	121
Table 5.4 Measurement results of surface area and volume of four fishes using 3D coordinate.....	121
Table 6.1 2D Image coordinate of the centroid point for moving object measurement .....	140
Table 6.2 Moving object measurement results of surface area and volume of four fishes using 3D coordinate.....	140
Table 6.3 Measurement difference comparison of the proposed offline, real-time, and real-time-moving object methods.	141

## Nomenclatures

Variables	Descriptions	Units
EPI	epipolar-plane image	
$a, b, c$	semi-major axes, semi-intermediate axes, semi-minor axes	mm
$x, y, z$	coordinates	
$A$	elliptic area	mm <sup>2</sup>
$S$	elliptic surface area	mm <sup>2</sup>
$V$	elliptic volume	mm <sup>3</sup>
$\theta$	eccentric angle of the point $P$	rad
$\phi$	eccentric angle of the point $q$	rad
$L, H, W$	elliptic length, width, and height	mm
$RGB$	red-green-blue color image	
$HSV$	hue, saturation, value color space	
$I$	image	
$B$	structuring element	
$I \ominus B$	erosion of an image $I$ by the structure element $B$	

$I \oplus B$	dilation of an image $I$ by a structuring element $B$
$I \ominus B$	opening of an image $I$ by a structuring element $B$
$I \bullet B$	closing of an image $I$ by a structuring element $B$
$F^2$	two-dimensional space of an image
$G$	Sobel operator
$Th$	threshold value
$R$	rotation matrix
$t$	translation matrix between origins of those two coordinate systems
$x_k$	state vector at a present time $k$
$A$	the transition matrix
$w$	the Gaussian process noise
$p(w)$	normal probability distribution
$Q$	process noise covariance matrix
$z_k$	measurement vector at the present time $k$
$H$	measurement matrix
$v_k$	measurement noise vector with the Gaussian measurement noise

$K_k$	Kalman gain
$x_{0,k}, y_{0,k}$	horizontal and vertical coordinate centroid
$l_k, h_k$	half-width and half-height of the tracking window
$v_{x,k}, v_{y,k}$	coordinate centroid speed
$v_{l,k}, v_{h,k}$	tracking window speed
$i^{\text{th}}$	moving object at frame $k^{\text{th}}$
$D(i, j)$	distance function between the $i^{\text{th}}$ object in the $k^{\text{th}}$ frame and the $j^{\text{th}}$ object in the $(k+1)^{\text{th}}$ frame
$A(i, j)$	the area difference between the $i^{\text{th}}$ object in the $k^{\text{th}}$ frame and the $j^{\text{th}}$ object in the $(k+1)^{\text{th}}$ frame
$S_k^i$	area of the tracking window $k^{\text{th}}$ frame of the $i^{\text{th}}$ object
$V(i, j)$	cost function
HD	high density camera
SE	morphology structuring element
bw	black and white image
PM	partition method
AM	analytic method

ZED	stereo camera
OpenCV	open source computer vision
2D	two dimension
3D	three dimension
$\sigma_x$	standard deviation of the prediction error in $x$ direction
$\sigma_y$	standard deviation of the prediction error in $y$ direction
$\beta$	learning rate
XYZ	absolute coordinate
LIBSVM	library for support vector machines
GRPSO	golden ratio particle swarm optimization
EPI	epipolar-plane image
GPS	global positioning system

# Chapter 1: Introduction

## 1.1 Background and motivation

The heavy duty of the tasks conducted in the fish sorting activities is operations performed by human operators. The operations are highly time-consuming and prone to produce stress and fatigue to their human operators due to the nature of the conditions under which they take place. Fig. 1.1 shows fish sorting activities to produce ergonomic hazards due to high speed conveyor belt, repetitive work, long-standing, and abnormal posture [1].



Fig. 1.1 Fish sorting activities performed by human operators with unprotected handling.

Fig. 1.2 shows a fish plant workers inspecting fish on a conveyor belt.



Fig. 1.2 A fish plant workers inspecting fish on a conveyor belt

In food processing industry, a volume is useful for size sorting, quality grading, and microbial concentration [2]. If volume of a food product can be determined, the other physical properties such as mass and density can be easily estimated. In egg, volume is related to many important things in bird life such as female mass, egg composition, nesting success, hatchling size, and nestling survival. In bread, volume is a good indicator for gas retention properties of dough, quality of flour. In fish shape, the important physical properties are their surface area and volume [3, 4]. Their surface area and volume are an essential part of fish processing problems. The surface area of the fish affects the salting process, i.e. the area and the thickness of the salt.

Furthermore, knowledge of surface area of fish shape is required as an integral part in heat and mass transfer calculations and in determination of physical properties such as gas permeability, weight per unit surface area, and respiration rates. Fish volume is one of the important issues in the production and processing of food product. Volume together with other physical properties plays an important role in calculating water loss, heat transfer, quantity of pesticide applications, respiration rates, etc. Similarly, the volume of the fish affects the speed of cooling and freezing which is ultimately useful for the determination of load and cooling costs [5, 6].

To measure the surface area and volume of food product had become an issue in measurement technique. Theoretical estimations based on product principal dimensions and weights were investigated for eggs in [7], apples, carrots, oranges and lemons in [8]. In [9], experimental methods were developed to measure surface area and volume of pears and plums. The tape method for surface area calculations, gas displacement and water displacement method for volume measurement were most commonly used [10]. However, the tape method is labor-intensive and subject to human error. Similarly, volume measurement cannot be performed for fish shape by using a gas displacement method and water displacement method because of the shape of the fish with cavities in the gills and mouth.

Because of these increasingly stringent requirements in food processing, and a result of advances in the available digital hardware and in image processing techniques, there has recently been much interest in using digital image analysis for grading systems [11]. A first step toward image processing methods was implemented when a

photographic method was proposed to estimate surface area and volume of eggs [12]. In this method, the top and bottom of the eggs were considered as segments of spheres and the sections were considered as cylinders. Even though it had good results, this method was very time-consuming and it was not practical for a large number of measurements.

Nowadays, the use of image processing is gaining interest for determining the surface area and volume of fruit. Sabliov et al. [13] used an image processing algorithm to determine surface area and volume of axisymmetric agricultural products. In [14], the methodology developed by Sabliov et al. [13] was used to measure the surface area and the volume of agricultural products. Two methods to predict the volume of Alaskan Pollock by image analysis were developed by [15]. In this proposed methods, the first method used dimensional measurement from images and correlated it to experimental volume. The second method used the cubic splines technique [16] and applied it to Alaskan pollock images. For the accuracy of volume prediction, this proposed method was compared to the volume measured experimentally. However, for effectiveness in calculations of fish surface area and volume, the image processing method in this proposed method is needed to be improved.

Prior to the calculations of fish surface area and volume, object detection and image segmentation is applied. The images captured by the video camera results in excessive information and complex disparities. The main problem is that shape and appearance of regions change significantly for images of scenes obtained from different viewpoints or different lighting conditions. Therefore, a new method

to extract the foreground object image is needed. Image segmentation is the initial task of analyzing images. Because of the gray color, texture, color, and different shapes, the image is divided into different regions with consistent characteristics. A threshold segmentation method was proposed in [17]. In this work, a novel method of Particle Swarm Optimization, called Golden Ratio Particle Swarm Optimization (GRPSO), was based on Golden Ratio. GRPSO was used for determining optimal thresholds to improve image segmentation. Generalizing edge detection to contour detection for image segmentation was proposed in [18]. In this approach, an extended image partition of image segmentation by requiring that the image model was sharply decreased in its energy. A novel method concerning image transition region extraction and segmentation was proposed in [19]. In this proposed method, the local variance of different areas of an image was employed for transition region extraction and segmentation. Fish contour extraction from images was proposed in [20]. In this proposed method, the fish image segmentation was obtained through a combination of the K-means clustering segmentation algorithm and mathematical morphology. Those proposed methods above aimed to improve the quality of image segmentation. But in the application, the image was taken first and processed. To solve this problem, real-time image segmentation is done. The real-time image segmentation method consists of two parts, the pre-processing method and the segmentation method.

The accuracy of applying stereo camera for 3D coordinate measurement is closely related to the accuracy of the camera calibration, and especially correction of camera distortion. Improper distortion models produce distortion residues which will be directly

projected back to the reconstructed 3D scene. This inaccuracy can be a serious problem in 3D measurement applications such as stereographic reconstruction. A method for recognizing an object of feature descriptor for being texture-less was proposed [21]. This method performed an initial dense descriptor computation to capture 2D and 3D gradient image information and aggregate the point-based information into local histograms. However, the image histogram was not suitable for real-time image segmentation. Many computer vision techniques have been investigated to produce complete 3D models. The computer vision techniques based on combining multi-view range images into complete 3D models were proposed in [22-24]. In [25-26], complete 3D models were proposed based on photographic image processing using volumetric reconstruction techniques such as voxel coloring and shape-of-silhouette. However, those methods require a lot of cameras, thus making it difficult to adjust the device. A multi-view 3D modeling system based on stereo camera techniques was proposed in [27]. This work presented a computer vision system to automatically generate 3D computer models by combining multi-view range images of real objects. 3D measurement using a fish-eye camera based on Epipolar-Plane Image (EPI) analysis was proposed in [28]. This paper proposed a method for taking 3D measurements using multiple fish-eye images acquired with one fish-eye camera. However, this work could cause distortion in the fish-eye image.

In this dissertation, a 3D coordinate measurement method using a stereo camera system is used. The stereo camera system based on real-time image segmentation is designed to develop automatic measurement systems.

To obtain exact position of the object using the stereo camera is very important for measuring the 3D coordinate. Prior to calculation of fish surface area and fish volume, the image geometric distortions must be in correct position. Fig. 1.3 shows the image correction result from the distorted image (a).

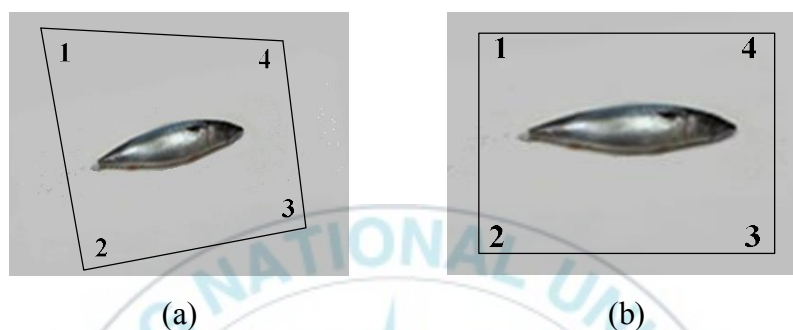


Fig. 1.3 Image correction. (a) Distorted image, (b) Corrected image

To bring the stereo camera in the precise position for measuring the target object, a vision direction system is used. 3D metrology and tracking systems including laser tracker and laser radar were introduced in [29]. Positioning sensing of the industrial robot was introduced in [30]. A comprehensive convergence method was introduced. Indoor GPS (Global Positioning System) was introduced in [31]. This proposed method presented the development of state-of-the-art, high speed, high accuracy, 3D laser radar technology. However, these systems were highly limited in terms of speed and workspace, and generally very expensive. The fast 3D position measurement with two unsynchronized cameras was proposed in [32]. This work described a vision system with two normal unsynchronized cameras for calculating the 3D position of objects at the rate of 60 fps. The 3D position was measured as center point in 3D through the detected

position on the image at the latest frame, and a 3D position was estimated by calculating previous frames. However, the synchronization in shutter timing of cameras should be used to process more images per second than a synchronized camera system. In [33], a measurement method for object distance by utilizing a camera was proposed. In this proposed method, a distance measurement method was done by using a mirror based on a camera. A sequence of reflected images was captured by a camera in front of a mirror. The images are then analyzed to obtain distance information. The distance measurement is based on the idea that the corresponding pixel of an object point at a long distance moves at a higher speed in a sequence of images. In [34], the distance and size estimation of an object was proposed by implementing a real-time stereo camera system. In this proposed method, before applying a connected component analysis method and a blob extraction technique, the object was firstly detected in both images, and then segmented. This method provides accurate distance and size estimations. In [35], a method for evaluating the three-dimensional measurement accuracy with parameter sets using a pair of stereo images was proposed. The pair of stereo images were acquired by REAL-3D-W1. This proposed method applied the concept of offline measurement. In [36], a stereoscopy technique for measuring distance was proposed. This algorithm was implemented using Matlab program. The distance measurement was done by representing stereoscopic images in offline method. C. Igathinathane et al. [37] proposed an application of 3D scanned imaging methodology for volume, surface area, and density evaluation of densified biomass. In this proposed method, a 3-D laser scanner as a measurement device was used, and to analyze 3D images were using image processing

software. Development of a simple three-dimensional machine-vision measurement system for in-process mechanical parts was proposed in [38]. In this method, a machine-vision was used to build a three-dimensional measurement system using a perspective transformation. The feature points in the world coordinate system were used to calculate the measurement data. In [39], a method for reconstructing 3D environment using fish-eye images based on EPI analysis was proposed. This proposed method enabled easy and stable matching of feature points. In EPI analysis, the movement of the camera was restricted to make fixed epipolar constraints between images, which facilitated the search for corresponding points.

K. Shimada et al. [40] proposed a high-speed 3D measurement method of a moving object using stereo vision. This proposed method used a high-speed 3D sensing system with active target-tracking, and a high-speed projector mounted on a two-axis active vision system. M. J. Kang et al. [41] proposed a distance and velocity measurement method of a moving object using a stereo camera system. In this proposed method, the stereo camera system was considered similar to the human eye. The distance and velocity of the moving object were measured using the disparity of two camera images acquired from the stereo camera.

Technological advances using image processing procedures have been mentioned above. A few of novel techniques were implemented using an image processing method useful for many tasks. There are several issues to be associated with using image processing methods used for measurements such as size, volume, distance and velocity of a moving object, and 3D measurement. However, none of the methods

mentioned above developed a measurement method for surface area and volume based on a 3D coordinate, neither the real-time nor moving objects were done. Therefore, a new measurement method for surface area and volume are needed. The new measurement method needs to be designed based on the 3D coordinate using an image processing method.

## **1.2 Objective and researching method**

The objective of this dissertation is to present mathematical modeling and image processing methods used for calculating fish surface area and volume, the system description used for calculating fish surface area and volume, a partition measurement method using image processing, a real-time measurement method, and a real-time measurement method for moving objects.

To develop a partition measurement method using image processing, the followings are done. Firstly, image acquisition and image calibration are done. Secondly, fish image shape is segmented to determine surface area and volume for computation. Thirdly, surface area and volume of fish are calculated by image processing technique. Finally, the fish surface area and volume with experimental results of the proposed partition measurement method using image processing method are compared to those of analytical measurement method.

To develop a real-time measurement method, the followings are done. Firstly, the stereo camera is calibrated to correct its intrinsic parameters and distortion parameters. Secondly, real-time image segmentation is done by combining threshold value, mathematical morphological transformation, and contour detection techniques to

extract objects in a graph-based image. Finally, the object coordinate, surface area and volume of the fish are measured.

To develop a real-time measurement method for moving object, the followings are done. Firstly, segmented object is shown in the target view. Secondly, a selected contour is automatically extracted and its image shape is stored. Thirdly, a stereo camera automatically identifies the targeting object by matching the two views of the contours. Finally, the stereo camera is repositioned at the reference position relative to the planar contour, and measure the object centroid and the object size.

### **1.3 Problem statements**

The problem statements considered to design a measurement method for fish surface area and volume based on 3d-coordinate using an image processing method are described as follows:

1. To derive mathematical model useful for calculating fish surface area and volume.
2. To design a partition measurement method using image processing.
3. To design a real-time measurement method based on 3D coordinate.
4. To design a real-time measurement method for moving objects.

### **1.4 Outline of dissertation and summary of contributions**

#### **Chapter 1: Introduction**

This chapter presents background and motivation, Objective and researching method, problem statements, and the outline of contents and the summary of contributions of this dissertation.

## **Chapter 2: Mathematical Modeling and Image Processing Methods**

This chapter presents the mathematical modeling useful for calculating fish surface area and volume. For mathematical modeling, the fish shape is considered to be ellipsoidal. The mathematical modeling consists of an analytical measurement method and a partition measurement method applied for image processing for calculating fish surface area and volume. This chapter also presents the overview of image processing methods used for image segmentation, the main principle of stereo camera used for real-time image segmentation and 3D coordinate measurement, and moving object tracking using Kalman filter.

### **Chapter 3: System Description**

This chapter describes the structure hardware used for the proposed measurement methods. The first one is structure hardware used for analytic measurement method and partition measurement method using image processing. The second one is structure hardware used for a proposed real-time measurement method. The third one is structure hardware used for a proposed real-time measurement method for moving objects.

### **Chapter 4: Analytic and partition measurement methods for fish surface area and volume**

This chapter presents an analytic and partition measurement method. For the fish digital profile images are obtained by stereo camera. The profile images are extracted using image segmentation for calculating surface area and volume. For image calibration, the actual

dimension of the fish is measured and used to get a calibration constant to calculate surface area and volume from shape features extracted from the profile images of the fish. Image processing and analysis consists of preprocessing, segmentation and feature extraction. A method to perform fish surface area and volume calculations is presented. To verify validation of the proposed partition measurement method, the experimental results of the proposed partition method are shown compared to those of the analytical measurement method.

### **Chapter 5: Real-time measurement method for fish surface area and volume**

This chapter presents a real-time measurement method for fish surface area and volume. The segmentation process is done in real-time on the video frame by stereo camera. The intrinsic and extrinsic parameters are obtained through the stereo camera calibration. To develop a real-time image segmentation method, a library available in open source computer vision (OpenCV, C++) is used. It is done by combining HSV color space, threshold value, mathematical morphological transformations, and contour detection techniques to extract objects in a graph-based image. A method to perform the real-time image segmentation is presented. The method is designed to perform fish surface area and volume calculations using open source computer vision (OpenCV, C++). This chapter also presents the 3D coordinate and measurement of fish surface area and volume by using stereo camera. To verify the validation of the proposed real-time measurement method, the experimental results of the proposed real-time measurement method are shown compared to those of the analytical measurement method.

## **Chapter 6: Real-time measurement method of fish surface area and volume for moving objects**

This chapter presents a real-time measurement method of moving objects for fish surface area and volume. A stereo camera is used for acquiring 3D information from moving objects and determines its size. The size of the moving object is obtained by tracking its contour. To complete this task, the following steps are done. The first step is that the segmented object is shown in the target view. The second step is that a selected contour is automatically extracted and its image shape is stored. The third step is that a stereo camera automatically identifies the targeting object by matching the two views of the contour. The final step is to reposition the stereo camera at the reference position relative to the planar contour, and measure the object centroid and the object size. To verify the validation of the proposed real-time measurement method of moving objects, the experimental results of the proposed real-time measurement method of moving objects are shown compared to those of the analytical measurement method.

## **Chapter 7: Conclusions and Future Works**

This chapter presents the conclusions for this dissertation and some ideas for future works are presented.

## **Chapter 2: Mathematical Modeling and Image Processing Methods**

This chapter presents the mathematical modeling useful for calculating fish surface area and volume. The fishes are considered as

ellipsoidal shapes to get analytical models for estimating their surface and volume. The mathematical modeling consists of an analytical method and a partition method applied for image processing to calculate fish surface area and volume. Section 2.2 presents image processing methods used for image segmentation. Section 2.3 presents the main principle of stereo camera used for real-time image segmentation and 3D coordinate measurement. Section 2.4 presents a moving object tracking method with Kalman filter.

## **2.1 Mathematical modeling to measure fish surface area and volume**

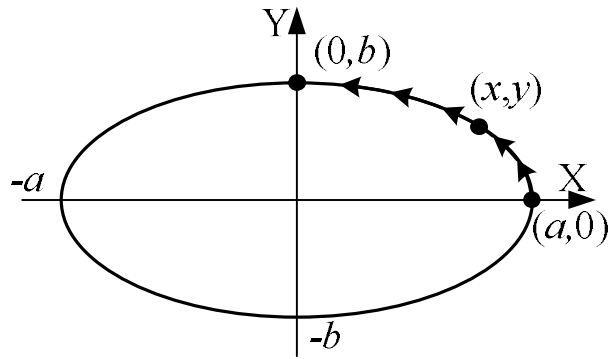
### **2.1.1 Analytical method**

#### **2.1.1.1 Surface area of ellipsoid**

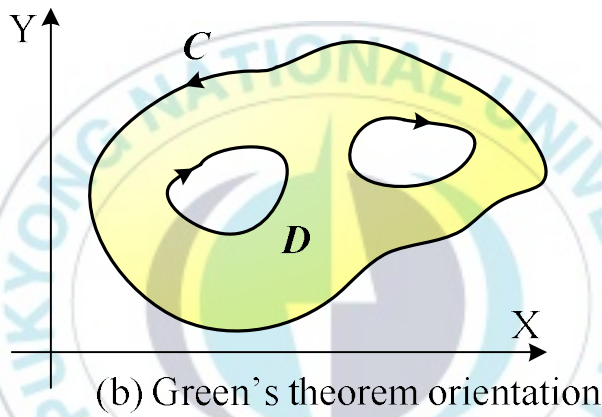
Equation of a standard ellipse on an arbitrary point  $(x,y)$  as shown in Fig. 2.1 is as follows:

$$\frac{x^2}{a^2} + \frac{y^2}{b^2} = 1 \quad (2.1)$$

where  $a$  is the semi-major axes, and  $b$  is the semi-intermediate axes as shown in Fig. 2.1.



(a) Ellipsoid model



(b) Green's theorem orientation

Fig. 2.1 Ellipsoid model

$$A = \iint_D 1 \, dA \quad (2.2)$$

where  $A$  is the area of the region  $D$  bounded by a standard ellipse.

According to Green's Theorem, if  $\frac{\partial Q}{\partial x} - \frac{\partial P}{\partial y} = 1$ , area of Eq. (2.2) is represented by taking line integral as follows:

$$A = \iint_D \left( \frac{\partial Q}{\partial x} - \frac{\partial P}{\partial y} \right) dA = \oint_C (Pdx + Qdy) \quad (2.3)$$

where  $C$  is a boundary of the region  $D$ ,  $P$  and  $Q$  are the continuous vector field defined on a region  $D$  in  $\mathbb{R}^2$ .

Putting  $P=0$  and  $Q=x$  in Eq. (2.3) yields:

$$A = \oint_C xdy = \iint_D \frac{\partial x}{\partial x} dA = \iint_D dA = A \text{ or } A = \oint_C xdy \quad (2.4)$$

Putting  $Q=0$  and  $P=-y$  in Eq. (2.3) yields:

$$A = \oint_C -ydx = -\iint_D \frac{\partial(-y)}{\partial y} dA = \iint_D dA = A \text{ or } A = -\oint_C ydx \quad (2.5)$$

From Eq. (2.4) and Eq. (2.5), the followings are obtained as

$$\therefore 2A = \oint_D (xdy - ydx), \text{ or}$$

$$A = \frac{1}{2} \left[ \oint_D (xdy - ydx) \right] = \frac{1}{2} \oint_D (xy - yx) = \frac{1}{2} \oint_D (-y, x) \cdot (\dot{x}, \dot{y}) \quad (2.6)$$

From Eq. (2.1), the ellipse can be parameterized as follows:

$$\frac{x^2}{a^2} + \frac{y^2}{b^2} = \cos^2(t) + \sin^2(t) = 1, \text{ or } \frac{x^2}{a^2} = \cos^2(t) \rightarrow x = a \cos(t) \text{ and}$$

$$\frac{y^2}{b^2} = \sin^2(t) \rightarrow y = b \sin(t).$$

The ellipse can be parameterized by  $\varphi(t) = (x, y) = (a \cos t, b \sin t)$  with  $0 \leq t \leq 2\pi$ . The elliptic area is obtained from Eq. (2.6) as follows:

$$\begin{aligned}
A &= \frac{1}{2} \int_0^{2\pi} (-b \sin(t), a \cos(t)) \cdot (-a \sin(t), b \cos(t)) dt \\
&= \frac{1}{2} \int_0^{2\pi} (ab \sin^2 t + ab \cos^2 t) dt = \pi \cdot ab
\end{aligned}
\tag{2.7}$$

The estimation of ellipsoid at arbitrary orientation is shown in Fig. 2.2.  $S$  is ellipsoid surface area, and  $V$  is ellipsoid volume. General equation of a standard ellipsoid on an arbitrary point  $(x,y,z)$  is as follows:

$$\frac{x^2}{a^2} + \frac{y^2}{b^2} + \frac{z^2}{c^2} = 1
\tag{2.8}$$

where  $a$  is the semi-major axes,  $b$  is the semi-intermediate axes and  $c$  is semi-minor axes.

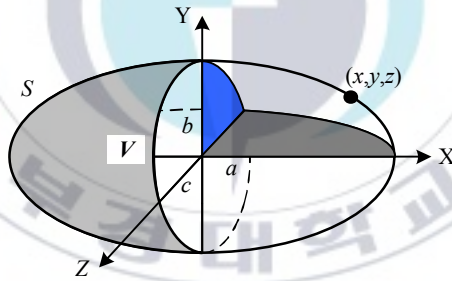


Fig. 2.2 ellipsoid at arbitrary orientation

From Eq. (2.8), partial derivatives  $\partial z / \partial x$  and  $\partial z / \partial y$  are obtained as follows:

$$\frac{\partial z}{\partial x} = - \frac{\frac{c^2}{a^2} x}{\sqrt{1 + \left(\frac{x^2}{a^2}\right) + \left(\frac{y^2}{b^2}\right)}}
\tag{2.9}$$

$$\frac{\partial z}{\partial y} = -\frac{\frac{c^2}{a^2}y}{\sqrt{1+\left(\frac{x^2}{a^2}\right)+\left(\frac{y^2}{b^2}\right)}} \quad (2.10)$$

Surface area of any three-dimensional object represented by  $z=f(x,y)$  is given by

$$S = \iint_R \sqrt{1+\left(\frac{\partial z}{\partial x}\right)^2+\left(\frac{\partial z}{\partial y}\right)^2} dx dy \quad (2.11)$$

where  $S$  is the surface area and  $R$  is the orthogonal projection of the object  $z=f(x,y)$  in the  $XY$ -plane as shown in Fig. 2.3.  $R$  is the elliptic disc represented by  $((x^2/a^2)+(y^2/b^2)) \leq 1$  in the  $XY$ -plane.

Fig. 2.3 shows the general standard ellipsoid, where  $x$ ,  $y$ , and  $z$  are coordinates,  $a$  is the semi-major axes,  $b$  is the semi intermediate axes, and  $c$  is the semi-minor axes.  $k$  is the perpendicular distance between the elliptic sections of  $(y^2/b^2)+(z^2/c^2)=1$  and

$$\frac{y^2}{b^2(1-k^2/a^2)} + \frac{z^2}{c^2(1-k^2/a^2)} = 1.$$

A point  $q$  in Fig. 2.3 is a point of centroid of two ellipses of  $\frac{x^2}{a^2} + \frac{u^2}{b^2 \cos^2 \theta + c^2 \sin^2 \theta} = 1$  and  $\frac{y^2}{b^2(1-k^2/a^2)} + \frac{z^2}{c^2(1-k^2/a^2)} = 1$ ,  $(-a < k < a)$ , and  $\phi$  is the eccentric angle of the point  $q$ .  $\theta$  is the eccentric angle of the point  $P$  in Fig. 2.4.

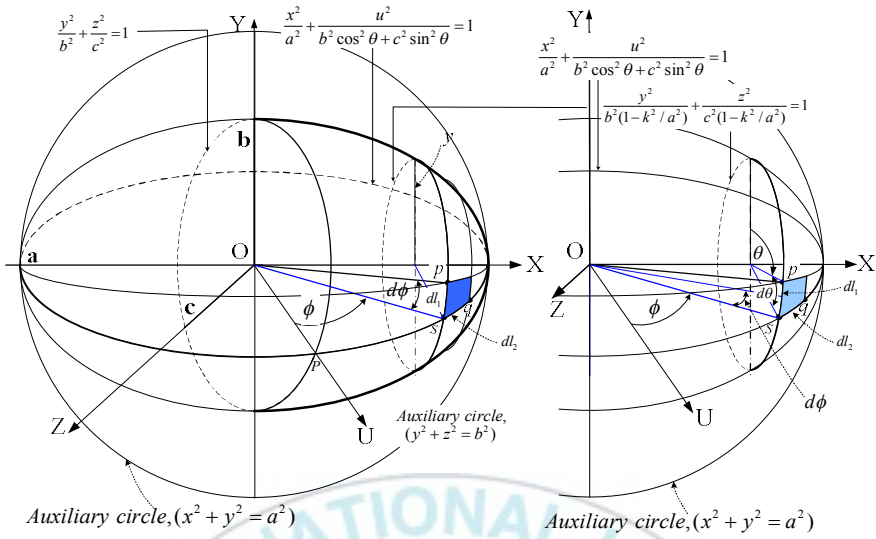


Fig. 2.3 General standard ellipsoid

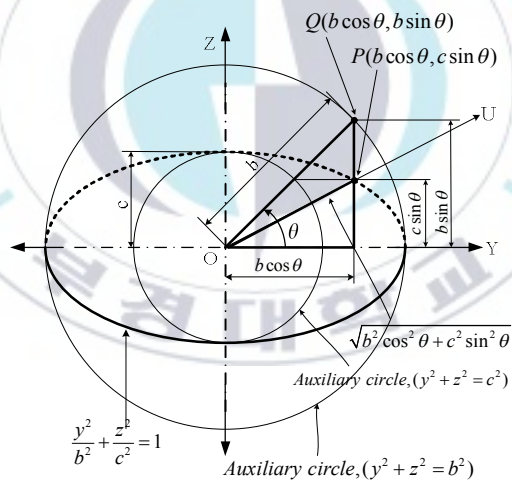


Fig. 2.4 Ellipse and its auxiliary circle

$d_{l1}$  and  $d_{l2}$  are defined as the lengths of  $\overline{qp}$  and  $\overline{qs}$  in Fig. 2.3 respectively. By putting  $x = a \cos \phi$ ,  $y = b \cos \theta$ ,  $z = c \sin \theta$ , and  $dx / dy = \sin \phi$ ,  $dl_1$  and  $dl_2$  are as follows:

$$\begin{aligned}
dl_1 &= \sqrt{1 + \left(\frac{dz}{dy}\right)^2} dx = \frac{dx}{dy} \sqrt{dy^2 + dz^2} \\
&= \sin \phi \sqrt{b^2 \sin^2 \theta + c^2 \cos^2 \theta} d\theta = ud\theta
\end{aligned} \tag{2.12}$$

$$\begin{aligned}
dl_2 &= \sqrt{1 + \left(\frac{du}{dx}\right)^2} dx = \sqrt{dx^2 + du^2} \\
&= \sqrt{(b^2 \cos^2 \theta + c^2 \sin^2 \theta) \cos^2 \phi + a^2 \sin^2 \phi} d\phi
\end{aligned} \tag{2.13}$$

A surface element in the surface area of the ellipsoid is written as  $(dl_1, dl_2)$ . Since the ellipsoid is symmetrical about the coordinate planes, the total surface area  $S$  is given by:

$$S = 8 \int_0^{\pi/2} \int_0^{\pi/2} (dl_1)(dl_2) \tag{2.14}$$

Substituting the values of Eqs. (2.12) and (13) into Eq. (14) and putting  $t = \cos \phi$  yields:

$$\begin{aligned}
S &= 8 \int_0^{\pi/2} \int_0^{\pi/2} \left( \sin \phi \sqrt{b^2 \sin^2 \theta + c^2 \cos^2 \theta} \right) \\
&\quad \times \left( \sqrt{(b^2 \cos^2 \theta + c^2 \sin^2 \theta) \cos^2 \phi + a^2 \sin^2 \phi} \right) d\theta d\phi \\
&= 8 \int_0^{\pi/2} \int_0^{\pi/2} \left( \sin \phi \sqrt{b^2 \sin^2 \theta + c^2 \cos^2 \theta} \right) \\
&\quad \times \left( \sqrt{(b^2 \cos^2 \theta + c^2 \sin^2 \theta - a^2) \cos^2 \phi + a^2} \right) d\theta d\phi \\
&= 8 \int_0^{\pi/2} \int_0^1 \left( \sqrt{b^2 \sin^2 \theta + c^2 \cos^2 \theta} \right) \times \left( \sqrt{a^2 - At} \right) dt d\theta
\end{aligned} \tag{2.15}$$

where  $A = a^2 - (b^2 \cos^2 \theta + c^2 \sin^2 \theta)$ .

Taking  $B = \sqrt{A} / a$ , and substituting in Eq. (2.15) and simplifying yields:

$$S = 4 \int_0^{\pi/2} \left( \sqrt{b^2 \sin^2 \theta + c^2 \cos^2 \theta} \right) \times \sqrt{b^2 \cos^2 \theta + c^2 \sin^2 \theta} d\theta + 4a \int_0^{\pi/2} \left( \sqrt{b^2 \sin^2 \theta + c^2 \cos^2 \theta} \right) \times \left( \frac{\arcsin(B)}{B} \right) d\theta \quad (2.16)$$

where

$$B = \sqrt{\frac{A}{a^2}} = \sqrt{1 - \left( \frac{b^2 \cos^2 \theta + c^2 \sin^2 \theta}{a^2} \right)} \quad (2.17)$$

The proof of Eq. (2.15) is shown in Appendix A.

The eccentricity of standard ellipse  $\varepsilon$  is obtained by putting  $\theta = 0$  in the prolate ellipsoid from Eq. (2.17) as follows:

$$\varepsilon = \sqrt{1 - \left( \frac{b}{a} \right)^2} = \frac{\sqrt{a^2 - b^2}}{a} = B \quad (2.18)$$

where  $\varepsilon$  is the eccentricity of the ellipse  $(x^2 / a^2) + (y^2 / b^2) = 1$ .

The surface area of the general ellipsoid can be computed using Eq. (2.18). To evaluate the surface area of the general ellipsoid depends on the parameters  $a$ ,  $b$ , and  $c$ . The semi-intermediate axis and semi-minor axis are equal for the prolate. By inserting  $c \approx b$  and by substituting the value of  $B$  into Eq. (2.18), the surface area of the prolate ellipsoid is obtained as follows:

$$S = 2\pi b^2 + 2\pi \left( \frac{ab}{\varepsilon} \right) \arcsin(\varepsilon) \quad (2.19)$$

The proof of Eq. (2.19) is shown in Appendix A.

Thus, the surface area of the general ellipsoid can be computed using Eq. (2.19) with ellipse eccentricity  $\varepsilon$ . The developed expression depends only on the parameters  $a = L/2$ ,  $b = W/2$ ,  $c = H/2$ , where  $L$ ,  $W$ ,  $H$ , respectively, as length, width, and height of ellipsoid.

### 2.1.1.2 Volume of an ellipsoid using triple integral.

Equation of the ellipsoid is Eq. (2.8). It is easier to calculate the volume of the ellipsoid using generalized spherical coordinate by taking  $x = a\rho \cos\varphi \sin\theta$ ,  $y = b\rho \sin\varphi \sin\theta$ , and  $z = c\rho \cos\theta$ .  $x$ ,  $y$ , and  $z$  are coordinates,  $a$  is the semi-major axes,  $b$  is the semi intermediate axes,  $c$  is the semi-minor axes. Based on mathematics convention, the symbols for the radial, azimuth, and zenith angle coordinates are taken as  $\rho$ ,  $\varphi$  and  $\theta$ , respectively.

$$dxdydz = |I| d\rho d\varphi d\theta \quad (2.20)$$

where  $|I| = abc\rho^2 \sin\theta$

The generalized spherical coordinate ranges within the limits:

$$0 \leq \rho \leq 1, \quad 0 \leq \varphi \leq \frac{\pi}{2}, \quad 0 \leq \theta \leq \frac{\pi}{2}$$

The volume of the ellipsoid is

$$\begin{aligned}
V &= 8 \iiint_R dx dy dz \\
&= 8abc \int_0^{\pi/2} d\varphi \int_0^1 \rho^2 d\rho \int_0^{\pi/2} \sin \theta d\theta = \frac{4}{3} \pi abc
\end{aligned} \tag{2.21}$$

where parameters  $a = L/2$ ,  $b = W/2$ ,  $c = H/2$ , as  $L, H, W$  are the length, width, and height of ellipsoid, respectively.

The proof of Eq. (2.21) is shown in Appendix B.

In order to calculate the volume of fish that is considered to be ellipsoidal, the analytical volume Eq. (2.22) of an ellipsoid is used as follows:

$$V = \frac{\pi}{6} \cdot L \cdot W \cdot H \tag{2.22}$$

### 2.1.2 Partition method applied for an image processing method

To evaluate the edge surface area of an elliptical disc, a representative edge length is obtained by three different technique (Fig. 2.5). The first one is the edge length parallel to the major axis such that when all such discs are assembled, they provide a step-ladder or staircase-like appearance for a smooth ellipsoid as shown in Fig. 2.5(a). The second one is the edge length inclined to the major axis where the curves connecting the edges of the two discs are assumed to be inclined straight lines. When such elliptic frustum discs are assembled, the outline is a series of inclined lines, which approximates the elliptical arc. The third one is the elliptic arc edge length, where the disc thickness is considered as equivalent to the length of the original itself.

Consider a partition disc on Fig. 2.5(b). By rearranging  $(x^2/a^2+y^2/b^2)=1$  for  $y$ , the following are given. In Fig. 2.5(e), if  $\Delta x$  and  $\Delta y$  is small enough, the curvature in the segment  $\Delta p$  can be derived as

$$\Delta p = \sqrt{\Delta x^2 + \Delta y^2} \quad (2.23)$$

By taking limitation of Eq. (2.23), the following is obtained.

$$dp = \sqrt{1 + \left(\frac{dy}{dx}\right)^2} dx \quad (2.24)$$

The Cartesian equation for an ellipse centered at origin is

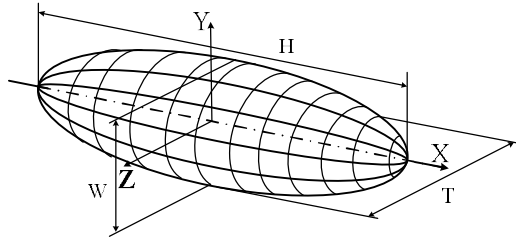
$$\frac{x^2}{a^2} + \frac{y^2}{b^2} = 1 \quad (2.25)$$

where  $a$  and  $b$  being the semi-major and semi-minor axes of ellipse.

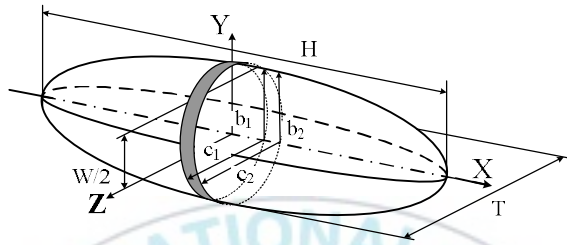
By take differentiating Eq. (2.25) and substituting Eq. (2.24), the followings are obtained:

$$\frac{2x dx}{a^2} + \frac{2y dy}{b^2} = 0 \rightarrow \frac{dy}{dx} = \frac{-b^2 x}{a^2 y}$$

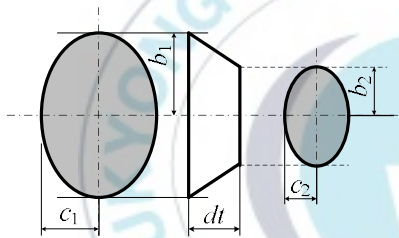
$$dp = \sqrt{1 + \frac{b^4 x^2}{a^4 y^2}} dx = \sqrt{1 + \frac{b^4 x^2}{a^4 y^2}} dx = \sqrt{1 + \frac{b^2 a^2}{a^2 (a^2 - x^2)}} dx \quad (2.26)$$



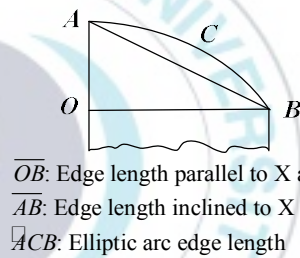
(a) Prolate spheroid orientation



(b) General ellipsoid

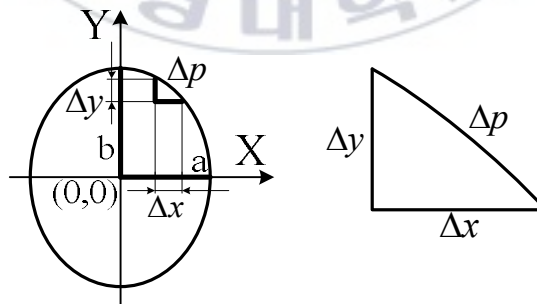


(c) Details of elliptical disc section details



$\overline{OB}$ : Edge length parallel to X axis  
 $\overline{AB}$ : Edge length inclined to X axis  
 $\overline{ACB}$ : Elliptic arc edge length

(d) Details of disc edge length



(e) Disc element

Fig. 2.5 General ellipsoid partitioned into discs and geometry orientation.

From Eq. (2.26), the perimeter of an ellipse  $p$  can be obtained by taking the integral of this expression over the domain of the ellipse in interval  $[-a, a]$  as follows:

$$\begin{aligned} \left(\frac{dp}{dx}\right)^2 &= 1 + \left(\frac{dy}{dx}\right)^2 = 1 + \frac{b^2 x^2}{a^2(a^2 - x^2)} = \frac{a^2(a^2 - x^2) + b^2 x^2}{a^2(a^2 - x^2)} \\ &= \frac{a^2 - x^2 \varepsilon^2}{a^2 - x^2} \end{aligned} \quad (2.27)$$

where an eccentricity of ellipse  $\varepsilon$  is given by Eq. (2.18).

By taking  $z = x/a$ , thus  $dx = a dz$  Eq. (2.27) become

$$dp = a \sqrt{\frac{1 - \varepsilon^2 z^2}{1 - z^2}} dz \quad (2.28)$$

Taking  $z = \sin \theta$ , the  $dz = \cos \theta d\theta$  and substituting them into Eq. (2.28) yields:

$$\begin{aligned} dp &= a \sqrt{\frac{1 - \varepsilon^2 \sin^2 \theta}{1 - \sin^2 \theta}} \cos \theta d\theta = a \sqrt{\frac{1 - \varepsilon^2 \sin^2 \theta}{\cos \theta}} \cos \theta d\theta \\ &= a \sqrt{1 - \varepsilon^2 \sin^2 \theta} d\theta \end{aligned} \quad (2.29)$$

By taking integral of Eq. (2.29), the perimeter of an ellipse ( $p$ ) is

$$p = 4a \int_0^{\pi/2} \sqrt{1 - \varepsilon^2 \sin^2 \theta} d\theta = 4a \int_0^{\pi/2} (1 - x)^{\frac{1}{2}} d\theta \quad (2.30)$$

where  $x = \varepsilon^2 \sin^2 \theta$ .

Unfortunately, the result of the Eq. (2.30) cannot be given in the usual analytic function. Therefore, the perimeter ( $p$ ) of the ellipse can

only be calculated using the sum of the series or the approximation formula. By using Binomial solution, perimeter of an ellipse is obtained approximately as follows:

$$\begin{aligned}
 (1-x)^n &= 1 - nx + \frac{n(n-1)x^2}{2!} - \frac{n(n-1)(n-2)x^3}{3!} \\
 &+ \frac{n(n-1)(n-2)(n-3)x^4}{4!} \\
 &- \frac{n(n-1)(n-2)(n-3)(n-4)x^5}{5!} \\
 &+ \frac{n(n-1)(n-2)(n-3)(n-4)(n-5)x^6}{6!} \dots \\
 &\approx 1 - nx
 \end{aligned} \tag{2.31}$$

For  $n=1/2$  and from Eqs. (2.30) and (2.31), perimeter of an ellipse is given approximately by

$$\begin{aligned}
 p &= 4a \int_0^{\pi/2} \sqrt{1 - \varepsilon^2 \sin^2 \theta} d\theta = 4a \int_0^{\pi/2} (1-x)^{\frac{1}{2}} d\theta \\
 &\approx 4a \int_0^{\frac{\pi}{2}} \left(1 - \frac{1}{2}x\right) d\theta = 4a \int_0^{\frac{\pi}{2}} \left(1 - \frac{1}{2}\varepsilon^2 \sin^2 \theta\right) d\theta \\
 &= 2\pi a \left(1 - \frac{\varepsilon^2}{(1)} \left(\frac{1}{2}\right)^2\right)
 \end{aligned} \tag{2.32}$$

The proof of Eq. (2.32) is shown in Appendix C.

For a normalized ellipse,  $\varepsilon^2 = 1 - \frac{b^2}{a^2} = 1 - \frac{(1-h)^2}{(1+h)^2}$  and  $h = \frac{a-b}{a+b}$ ,

by using Gauss-Kummer series, the ellipse perimeter is obtained as follows:

$$p = \pi(a+b) \left( 1 + \left( \frac{1}{2} \right)^2 h^2 \right) \quad (2.33)$$

The proof of Eq. (2.33) is shown in Appendix C.

The perimeter of an ellipse can be simplified [42]. Because  $h^2$  is very small, the perimeter of an ellipse in Eq. (2.33) can be written as  $p \approx \pi(a+b)$ .

### 2.1.2.1 Surface area and volume of an ellipsoid.

Next, consider a partition disc on Fig. 2.6(a, b and c) as follows:

For the  $i^{\text{th}}$  partitioned disc, the following equation is given as:

$$\frac{y^2}{b_i^2} + \frac{z^2}{c_i^2} = 1, \quad \text{for } i = 2, 3, \dots, n/2 \quad (2.34)$$

where  $b_i = \frac{b}{a} \sqrt{a^2 + k_i^2}$ ,  $c_i = \frac{c}{a} \sqrt{a^2 + k_i^2}$ ,  $k_i$  is the distance from standard  $x$ -axis to the  $i^{\text{th}}$  disc.

Perimeter the  $i^{\text{th}}$  partitioned ellipse is given as  $p_i = \pi(c_i + b_i)$ . Furthermore,  $i$  is defined as  $i_1$  and  $i_2$  set as disc of the left and right, respectively.

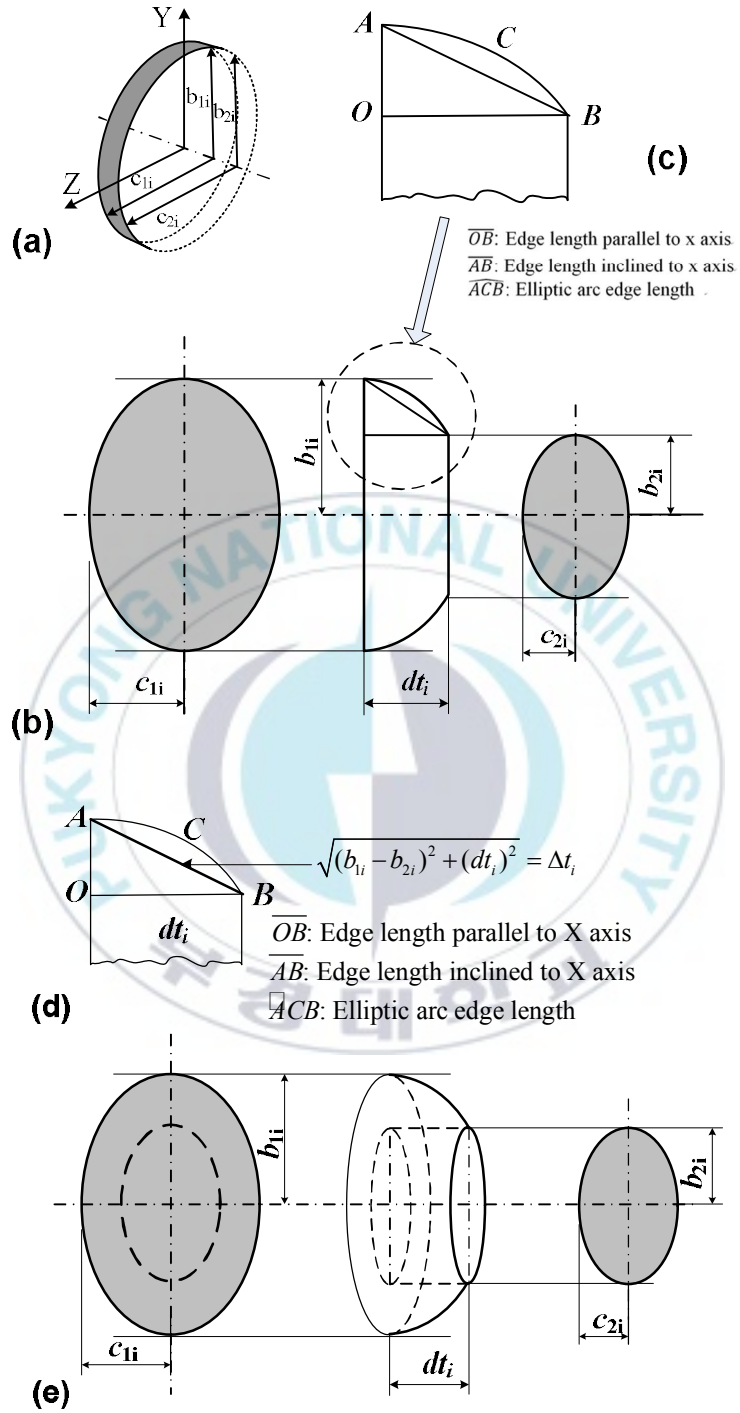


Fig. 2.6 Partition of left disc  $i_1$  and right disc  $i_2$

In Fig. 2.6(d) and Fig. 2.6(e), line  $\overline{OA}$  is very small (as pixel of an image) and approximated as  $\overline{OA} = (b_{1i} - b_{2i}) \approx (c_{1i} - c_{2i})$  as prolate ellipsoid, and  $\overline{OB} = dt_i$  is obtained. For very small length of  $\overline{AB}$ , it is approximated as  $\square ACB = \overline{AB}$  as follows:

$$\Delta t_i = \overline{AB} = \sqrt{(b_{1i} - b_{2i})^2 + (dt_i)^2} \quad (2.35)$$

The surface area and volume of each disc can be calculated as follows:

$$S_i = \pi (b_i + c_i) \Delta t_i \quad (2.36)$$

$$S = \sum_i^{n/2} S_i \text{ for } i = 2, 3, \dots, n/2 \quad (2.37)$$

Area of each disc is calculated as average area of left and right planes, and  $dt_i$  is very thin and set as a pixel. The volume of each disc can be calculated as follows:

$$V_i = \pi \Delta t_i (b_i c_i) \quad (2.38)$$

$$V = \sum_i^{n/2} V_i \text{ for } i = 2, 3, \dots, n/2 \quad (2.39)$$

where  $b_{1i} = W_{1i} / 2$  and  $b_{2i} = W_{2i} / 2$  denote heights of the discs of the left and right planes in top view,  $c_{1i} = H_{1i} / 2$  and  $c_{2i} = H_{2i} / 2$  denote widths of the discs of left and right planes in side view, respectively,  $dt_i$  denotes as the thickness between disc of the left and right planes, and  $n$  denotes the number of boundary point of the fish contours.

## 2.2 Image processing methods

### 2.2.1 Pre-processing of image

From RGB color image, it is transformed to HSV color space. H, S, and V components are obtained using transformation equations described as follows [43]:

Hue calculation:

$$H = \begin{cases} 0^\circ & \text{for } C_{\max} - C_{\min} = 0 \\ 60^\circ \times \frac{G' - B'}{C_{\max} - C_{\min}} & \text{for } C_{\max} = R' \\ 60^\circ \times \frac{B' - R'}{C_{\max} - C_{\min}} & \text{for } C_{\max} = G' \\ 60^\circ \times \frac{R' - G'}{C_{\max} - C_{\min}} & \text{for } C_{\max} = B' \end{cases} \quad (2.40)$$

Saturation calculation:

$$S = \begin{cases} 0 & \text{for } C_{\max} = 0 \\ \frac{C_{\max} - C_{\min}}{C_{\max}} & \text{for } C_{\min} \neq 0 \end{cases} \quad (2.41)$$

Value calculation:

$$V = C_{\max} \quad (2.42)$$

where  $R' = \frac{R}{255}$ ,  $G' = \frac{G}{255}$ , and  $B' = \frac{B}{255}$ .

The object can be easily separated from its background in  $S$  and  $V$  components. Gaussian filter is applied to reduce noises to both  $S$  and

$V$  components. A grayscale image is then constructed by calculating the average of  $S$  and  $V$  component.

### 2.2.2 Region labelling

Region labelling is the division of an image into objects or sets of connected pixels [44]. Generally, the 1's in a binary image form the objects, and the 0's form the background. Two object pixels are directly connected to one another if they are neighbours of one another. Pixel neighborhoods can be defined in terms of 4-connectivity in which the two pixels share a common side, or of 8-connectivity in which the two pixels share either a common side or a common corner (see Fig. 2.7).

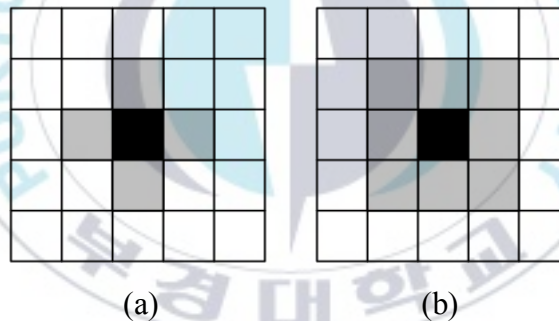


Fig. 2.7 Black object pixel with (a) 4-connected and (b) 8-connected neighbours shown in grey.

The region labeling process begins by scanning the binary image for the first instance of an object pixel. A search algorithm is then implemented to locate all pixels connected to the initial pixel so that the connected pixels can be assigned to the same region, namely region one. After this, region one may be removed from the binary image (by setting each of its pixels to the value of the background) and the

process of locating another object pixel and its connected pixels may be repeated. The process continues until all object pixels have been labeled.

Fig. 2.8 shows an example of a binary image (a) with three labeled objects if connectivity is defined as 4-connectivity (b), or two labeled objects if connectivity is defined as 8-connectivity (c). In this dissertation, 4-connectivity is used for the purposes of region labeling.

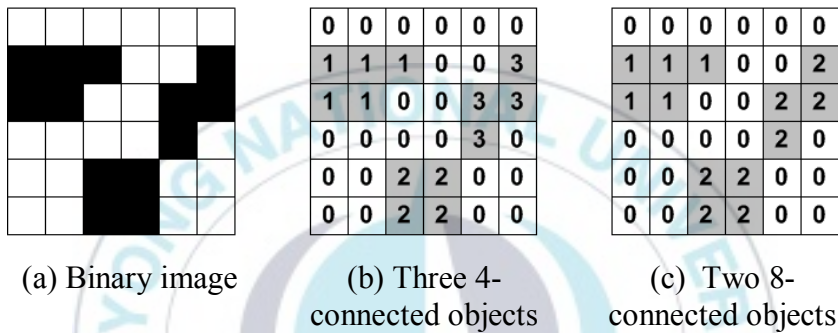


Fig. 2.8 Binary image with three labeled objects.

### 2.2.3 Binary morphology

Binary morphology [45,46] is a non-linear branch of image processing that is used to alter the geometrical structure of a binary image. The two fundamental processes of morphology are erosion and dilation. These processes are used for the alteration of an image with another image called a structuring element. The structuring element is usually smaller than the image. Fig. 2.9 shows an example of erosion and dilation of an image.

Erosion uses a structuring element to reduce the number of 1's or non-zero pixels in an image. The origin of the structuring element is overlaid over each pixel in the original image. Only if every non-zero

value of the structuring element is contained in the original image, the corresponding pixel in the resultant image should be set to 1. The erosion of an image  $I$  by a structuring element  $B$  is written as  $I \ominus B$ .  $I$  and  $B$  are treated as the sets of non-zero pixels in the images. Fig. 2.8(a) shows an example of a binary image with ‘ones’ shown as black color.

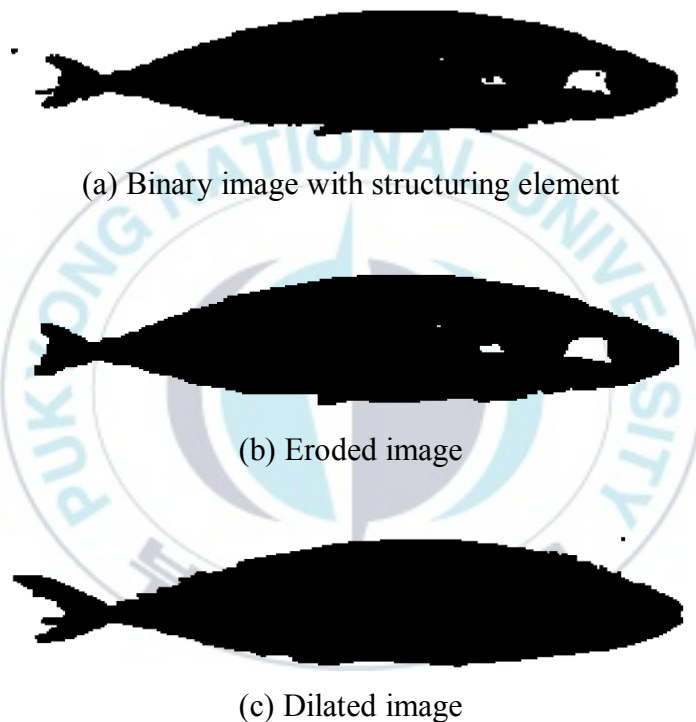
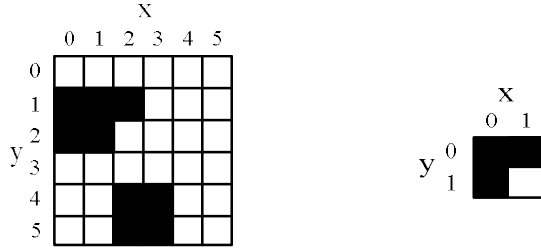


Fig. 2.9 Binary, erosion, and dilation of an image.

Fig. 2.10 shows the coordinate locations of the black pixels from the set of  $I$  which completely describes the binary object. Fig. 2.10(a) shows the  $6 \times 6$  binary image and expressed in Eq. (2.41), and  $B$  in Fig. 2.10(b) describes  $2 \times 2$  structuring element of the binary object and expressed in Eq. (2.44).

$$I = \{(0,1), (0,2), (1,1), (1,2), (2,1), (2,4), (2,5), (3,4), (3,5)\} \quad (2.43)$$

$$B = \{(0,0), (0,1), (1,0)\} \quad (2.44)$$



(a)  $6 \times 6$  binary image  $A$       (b)  $2 \times 2$  structuring element  $B$ .

Fig. 2.10 Coordinate locations of the black pixels.

Erosion of an image  $I$  by the structure element  $B$  is given by the set operation of  $I \ominus B$  is defined as follows:

$$I \ominus B = \{p \in F^2 \mid (p + q) \in I, \text{ for every } q \in B\} \quad (2.45)$$

where  $F^2$  is the two-dimensional space of an image, and  $p$  and  $q$  are pixel location. The erosion is the centroid of the translations of  $I$  by  $-B$ . In the case of Fig. 2.9,  $-B$  is as follows:

$$-B = \{(0,0), (0,-1), (-1,0)\} \quad (2.46)$$

Since  $-B$  has 3 elements, in this case there are 3 translations of  $I$  as follows:

$$I_{(0,0)} = \{(0,1), (0,2), (1,1), (1,2), (2,1), (2,4), (2,5), (3,4), (3,5)\}$$

$$I_{(0,-1)} = \{(0,0), (0,1), (1,0), (1,1), (2,0), (2,3), (2,4), (3,3), (3,4)\}$$

$$I_{(-1,0)} = \{(-1,1), (-1,2), (0,1), (0,2), (1,1), (1,4), (1,5), (2,4), (2,5)\}$$

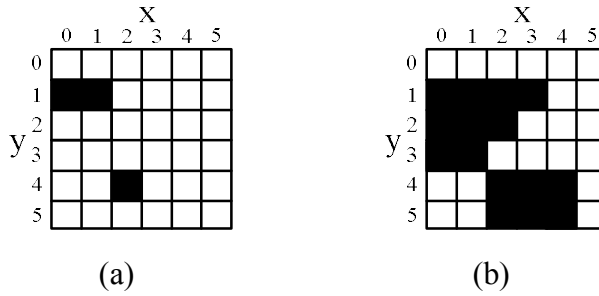


Fig. 2.11 Structuring element. (a) Erosion, (b) Dilation of the binary image shown in Fig. 2.10(a) using the structuring element shown in Figure 2.10(b).

The centroids of  $I_{(0,0)}$ ,  $I_{(0,-1)}$ , and  $I_{(-1,0)}$  are the set of the pixels in the eroded object as shown in Fig. 3.10(a). This centroid consists of three pixel coordinates: (0,1), (1,1), and (2,4).

Dilation uses the structuring element to increase the number of non-zero pixels in an image. The origin of the structuring element is overlaid over each pixel in the image in turn. If the image pixel is non-zero, then each pixel is added to the resultant image. The dilation of an image  $I$  by a structuring element  $B$  mathematically defined as follows:

$$I \oplus B = \{(p+q) | p \in I, q \in B\} \quad (2.47)$$

Thus, dilation is the union of the translations of  $I$  by  $B$ . In this case, a structuring element of  $B$  has three elements, the three translations of  $I$  as follows:

$$\begin{aligned} I_{(0,0)} &= \{(0,1), (0,2), (1,1), (1,2), (2,1), (2,4), (2,5), (3,4), (3,5)\} \\ I_{(0,1)} &= \{(0,2), (0,3), (1,2), (1,3), (2,2), (2,5), (2,5), (3,5), (3,5)\} \\ I_{(1,0)} &= \{(1,1), (1,2), (2,1), (2,2), (3,1), (3,4), (3,5), (4,4), (4,5)\} \end{aligned}$$

The union of the sets of  $I_{(0,0)}$ ,  $I_{(0,1)}$ , and  $I_{(1,0)}$  gives the coordinate of the pixels in the dilated object as shown in Fig. 2.11(b).

The morphological operations of opening and closing are defined as combinations of erosions and dilations of a binary image [47]. The opening of an image  $I$  by a structuring element  $B$  is defined as follows:

$$I \circ B = (I \ominus B) \oplus B \quad (2.48)$$

Opening a binary image smoothes the contours of objects within it, by eliminating small islands and sharp spikes in image.

The closing of an image  $I$  by a structuring element  $B$  is as follows:

$$I \sqcap B = (I \oplus B) \ominus B \quad (2.49)$$

Closing a binary image smoothes the contours of the objects within it by eliminating small holes and fusing narrow break lines.

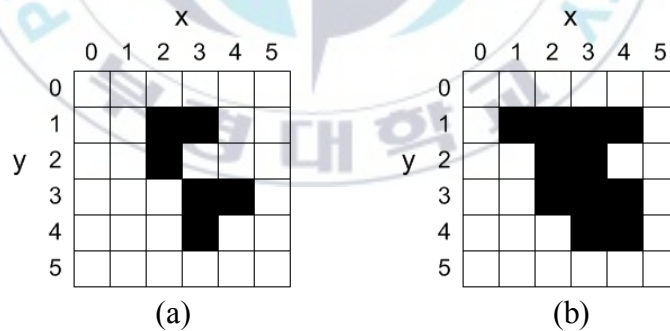


Fig. 2.12 Opening and closing (a) Opening, (b) Closing of the binary image shown in Fig. 2.10(a) using the structuring element shown in Figure 2.10(b).

## 2.2.4 Image edge detection

### 2.2.4.1 Sobel operator

In the edge detection, to detect solid shape is a very special thing. It has a strong edge that can quickly change brightness and color. In using colored images, the edge detection has to be applied on each channel of the image. Most of the simple edge detectors like Sobel can identify strong edges.

The edge of an object was obtained by convoluting the grayscale image  $G$  with Sobel operator [45]. Sobel operator performs edge detection by determining the gradient of the grayscale image  $G$  with respect to horizontal and vertical directions. The gradient of a pixel in  $G$  is calculated by using operators of Eq. (2.50). A pixel in  $G$  is an edge if  $(G_x^2 + G_y^2)^{1/2} \geq Th$  in the pixel for some threshold value  $Th$ .

$$G_x = \begin{bmatrix} -1 & -2 & -1 \\ 0 & 0 & 0 \\ 1 & 2 & 1 \end{bmatrix}, \quad G_y = \begin{bmatrix} -1 & 0 & 1 \\ -2 & 0 & 2 \\ -1 & 0 & 2 \end{bmatrix}, \quad (2.50)$$

### 2.2.4.2 Kernel design

The robustness of noise is important because the algorithms applied should also work with automatic systems. To reduce noise can be done by smoothing filters with the kernel size. To design 2-D filter kernel can be written in the form as follows [48]:

$$H(\rho, \theta) = H_\rho(\rho)H_\theta(\theta) \quad (2.51)$$

$$H_{\rho}(\rho) = \begin{cases} 1 & \text{if } 0 \leq \rho \leq \pi / 2 \\ 0 & \text{else} \end{cases} \quad (2.52)$$

where  $H$  indicates polar frequency response,  $\rho$  is the radial frequency, and  $\theta$  is the angular frequency.

The radial component of the low-pass filter kernel is an approximation of the ideal 1-D low-pass filter with a cutoff at  $\pi/2$  radians by assuming 2:1 subsampling in each spatial dimension between successive pyramid levels.

#### 2.2.4.3 Graph cut

Graph cut is a technique based on powerful graph cut algorithms from combinatorial optimization [49, 50]. In the graph cut algorithm, the image to be inspected is represented as a 2D weighted graph like in the live wire segmentation technique [51]. Every node in this graph can be in one of two states: an object pixel and a background pixel. Therefore, an internal probabilistic color model is needed [52], which is initialized based on the user input. The weights on the links are defined by an energy function which consists of both region and boundary information. The approach uses the min-cut/max-flow algorithm to find a binary (object/background) segmentation of the image.

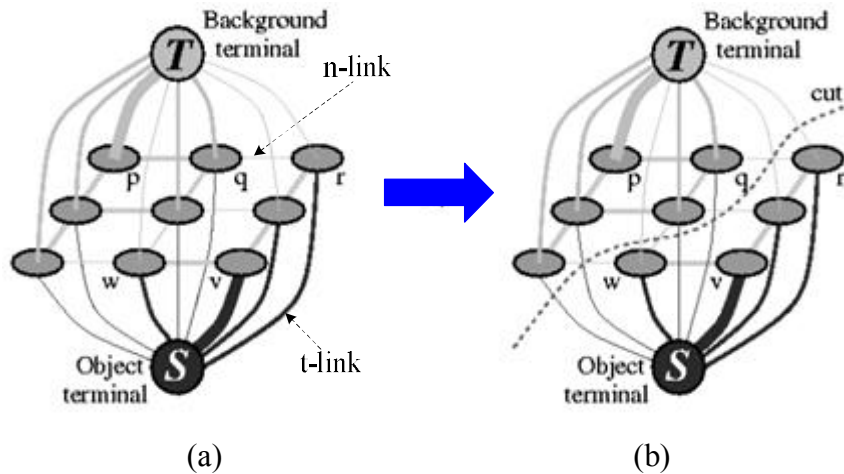


Fig. 2.13 A graph and the corresponding cut.

(a) Graph, (b) Cutting through the graph

The graph cut algorithm is based on a graph  $\mathcal{G}(v, \varepsilon)$  which consists of nodes  $v = I \cup \{s, t\}$  directly connected by two-way direction of weighted edge  $\varepsilon$ . The nodes correlate to the pixels of an image  $I$  except for two additional terminal nodes  $\{s, t\}$  which are called source  $s$  and sink  $t$ . Each graph edge is assigned as some nonnegative weight, cost or energy  $\omega(q, p)$ , where the inverse direction  $\omega(p, q)$  can have a different weight. Edges connecting only nodes from  $I$  are called  $n$ -links, whereas the edges from nodes to terminal nodes are called  $t$ -links. Nodes of  $I$  are only connected to their direct neighbors  $N$  and to both terminal nodes  $S$  and  $T$  as shown in Fig. 2.13(a).

The minimum cut or min-cut of this graph can then be used to minimize certain energy functions. A cut partition is a graph into two distinct subsets  $S$  and  $T$  such that the terminal nodes  $s$  and  $t$  are elements of the sets  $S$  and  $T$ , respectively. The cut is, therefore, also called  $s$ - $t$ -cut. Fig. 2.13(b) shows such a cut through a graph.

A cut-set  $C_i \in C$  is a set of edges  $(p, q)$  such that  $p \in S$  and  $q \in T$ . The cost  $|C_i|$  of a cut is the sum of the weights or costs  $w_{pq}$  over the edges in the cutset  $C_i$ . The minimum cut problem is to find the cut with the minimum costs among all cuts.

$$|C_{\min}| = \arg \min_C |C_i| \quad (2.53)$$

with

$$|C_i| = \sum_{(p,q) \in C_i} w_{pq} \quad (2.54)$$

Furthermore, the edges in  $C_i$  can be split into  $t$ -links and  $n$ -links. When making a cut, for each node  $p$  the cut contains a  $t$ -link, either the edge  $(p, s)$  or  $(p, t)$ .

Additionally, the cut can also contain  $n$ -links connecting the node  $p$  with its neighbor  $q$ , and such that  $p \in S$  and  $q \in T$ . The selection of the  $t$ -link  $(p, s)$  or  $(p, t)$  at node  $p$  can be modeled using a predicate  $D_p$  ( $f_p$ ) for selecting  $(p, s)$  or  $(p, t)$ , respectively. Therefore, the cost of the cut can now be written as follows:

$$|C_i| = \sum_{p \in I} D_p(f_p) + \sum_{\substack{(p,q) \in N \\ p \in S, q \in T}} w_{pq} \quad (2.55)$$

This formulation is a special case of an energy function. It can be expressed in the generalized form as follows:

$$E(x) = \sum_{p \in I} U_p(x_p) + \lambda \sum_{(p,q) \in N} V_{p,q} \cdot \delta(x_p, x_q) \quad (2.56)$$

$$\delta(x_p, x_q) = \begin{cases} 1 & \text{if } x_p \neq x_q \\ 0 & \text{otherwise} \end{cases} \quad (2.57)$$

where  $U_p(x_p)$  is a function derived from the observed data,  $\lambda$  is a weighting constant between the regional term and data constraint,  $x_p$  and  $x_q$  are binary values of variables  $p$  and  $q$ .  $V_{p,q}$  measures the cost of assigning the labels  $f_p, f_q$  to the adjacent pixels  $p, q$  and is used to impose spatial smoothness. The boundary term or regularizing constraint and the additional sub modularity constraint [53] is as follows:

$$V_{pq}(0,0) + V_{pq}(1,1) \leq V_{pq}(0,1) + V_{pq}(1,0) \quad (2.58)$$

## 2.3 Stereo camera

### 2.3.1 Pinhole camera model

The pinhole model [54], an ideal non-distorted model, is the simplest and most common camera model shown in Fig. 2.14.  $C - X_C Y_C Z_C$  and  $O_W - X_W Y_W Z_W$  are the camera coordinate frame and the world coordinate frame, respectively. A point  $P_W(X_W, Y_W, Z_W)$  on an object in the world coordinate frame is a point  $P_u = (x_u, y_u)$  image on the image coordinate plane.

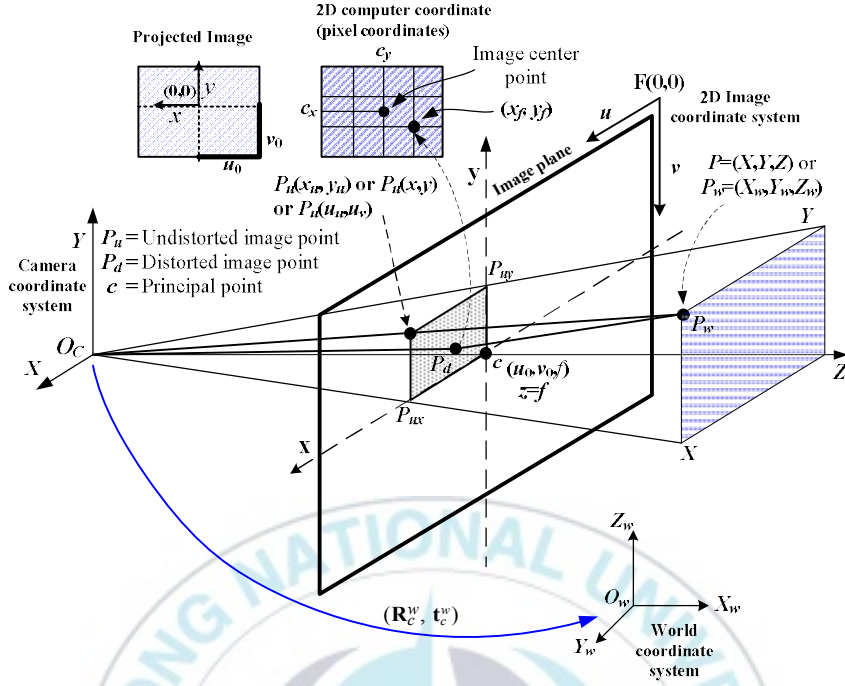


Fig. 2.14 Pinhole camera model

The transformation between the camera coordinate frame and world coordinate frame is represented by  $R_c^w$  and  $t_c^w$ . The  $R_c^w$  is a rotation matrix and  $t_c^w$  is a translation vector from the world coordinate frame to the camera coordinate frame, respectively. The relation between  $P_w$  and  $P_u$  can be written as follows:

$$s \begin{bmatrix} x \\ y \\ z \end{bmatrix} = \begin{bmatrix} f & 0 & 0 \\ 0 & f & 0 \\ 0 & 0 & 1 \end{bmatrix} \begin{bmatrix} R_c^w & t_c^w \end{bmatrix} \begin{bmatrix} X_w \\ Y_w \\ Z_w \\ 1 \end{bmatrix} \quad (2.59)$$

where  $s$  is uncertainty nonzero scale factor of camera, and  $f$  is focal length.

The transformation from the image coordinate to the screen coordinate is obtained as follows:

$$\begin{bmatrix} u \\ v \\ 1 \end{bmatrix} = \begin{bmatrix} P_{ux} & 0 & u_0 \\ 0 & P_{uy} & v_0 \\ 0 & 0 & 1 \end{bmatrix} \begin{bmatrix} x \\ y \\ 1 \end{bmatrix} \quad (2.60)$$

where  $u$  and  $v$  are image projection,  $(u_0, v_0)$  are the principal point, and  $P_{ux}$  and  $P_{uy}$  are the number of pixels per unit distance on the image frame in the  $x$  and  $y$  directions, respectively.

From Eq. (2.59) and Eq. (2.60), Eq. (2.61) is obtained as follows:

$$s \begin{bmatrix} u \\ v \\ 1 \end{bmatrix} = \begin{bmatrix} f_x & 0 & u_0 \\ 0 & f_y & v_0 \\ 0 & 0 & 1 \end{bmatrix} \begin{bmatrix} \mathbf{R}_c^w & \mathbf{t}_c^w \\ Y_w \\ Z_w \\ 1 \end{bmatrix} = \mathbf{A} \begin{bmatrix} \mathbf{R}_c^w & \mathbf{t}_c^w \\ Y_w \\ Z_w \\ 1 \end{bmatrix} \quad (2.61)$$

where  $f_x = P_{ux} f$  and  $f_y = P_{uy} f$  as the focal length of the camera in terms of pixels dimensions in the  $x$  and  $y$  directions, respectively.  $\mathbf{A}$  is the intrinsic parameter matrix of camera, and  $[\mathbf{R}_c^w \ \mathbf{t}_c^w]$  is the extrinsic parameter of the camera.

The pinhole camera model can be defined by providing two sets of parameters: the extrinsic parameters and the intrinsic parameters.

### 2.3.2 Extrinsic camera parameters

The extrinsic parameters of the perspective camera are all the necessary geometric parameters that allow a change from the camera coordinate system to the external coordinate system, and vice versa. From Fig. 2.14, transformation from the camera coordinate system  $C$  to the external world coordinate system  $W$  can be accomplished using

a translation  $\mathbf{t}$  and a rotation  $\mathbf{R}$ . The translation vector  $\mathbf{t}$  is a transformation in position of coordinate 3-dimensional translation vector. The rotation, in turn, transforms the corresponding axes of each system. This rotation transformation  $\mathbf{R}$  is described by the orthogonal matrix with  $3 \times 3$  dimension.

For a given point  $P$ , the camera coordinate  $C$  and the external world coordinate  $W$  are connected by the following equation:

$$P_C = \mathbf{R}(P_W - \mathbf{t}) \quad (2.62)$$

where  $P_c$  is a point  $P$  in the camera coordinate system,  $P_w$  is its point in the world coordinate system,  $\mathbf{R}$  stands for the rotation matrix and  $\mathbf{t}$  is the translation matrix between origins of the two coordinate systems.

The matrices  $\mathbf{R}$  and  $\mathbf{t}$  can be specified as follows:

$$\mathbf{R} = \begin{bmatrix} \mathbf{R}_1 \\ \mathbf{R}_2 \\ \mathbf{R}_3 \end{bmatrix} \begin{bmatrix} R_{11} & R_{12} & R_{13} \\ R_{21} & R_{22} & R_{23} \\ R_{31} & R_{32} & R_{33} \end{bmatrix}, \quad \mathbf{t} = O_w - O_c = \begin{bmatrix} \mathbf{t}_1 \\ \mathbf{t}_2 \\ \mathbf{t}_3 \end{bmatrix} \quad (2.63)$$

where  $R_i$  denotes an  $i^{\text{th}}$  row of the rotation matrix  $\mathbf{R}$ , i.e.  $\mathbf{R} = [R_{i1}, R_{i2}, R_{i3}]$  for  $i=1 \sim 3$ .

### 2.3.3 Intrinsic camera parameters

The intrinsic camera parameters can be summarized as follows:

1. The parameters of the projective transformation itself: For the pinhole camera model, this is given by the focal length  $f$ .
2. The parameters that map the camera coordinate system into the image coordinate system: Assuming that the origin of the image

constitutes a point  $c = (u_0, v_0)$  in a central point and that the physical dimensions of pixels (usually expressed in  $\mu\text{m}$ ) on a camera plane in the two directions are constant and given by  $P_{ux}$  and  $P_{vy}$ , a relation between the image coordinate  $(u, v)$  and the camera coordinate  $(x, y)$  can be stated as follows:

$$\begin{aligned} x &= (u - v_0)P_{ux} \\ y &= (v - u_0)P_{vy} \end{aligned} \quad (2.64)$$

where a point  $(x, y)$  is related to the camera coordinate system  $C$ , whereas  $(v, u)$  and  $(v_0, u_0)$  are related to the system of a camera plane system.

3. The radial distortions can be modelled by providing a nonlinear correction (offset) to the real coordinate of a given image point. This can be accomplished by adding even-order polynomial terms as follows:

$$x_v = \frac{u}{1 + k_1 r^2 + k_2 r^4}, \quad y_v = \frac{v}{1 + k_1 r^2 + k_2 r^4} \quad (2.65)$$

where  $r^2 = x_v^2 + y_v^2$ ,  $k_1$  and  $k_2$  are the new intrinsic parameters of the perspective camera that model the influence of the radial distortions of the optical system;  $u$  and  $v$  are the ideal coordinate with no distortions of a given image point; and  $x_v$  and  $y_v$  are the modified coordinate reflecting the radial distortions.

### 2.3.4 Two pinhole camera model

Fig. 2.15 shows the two pinhole camera models [55].

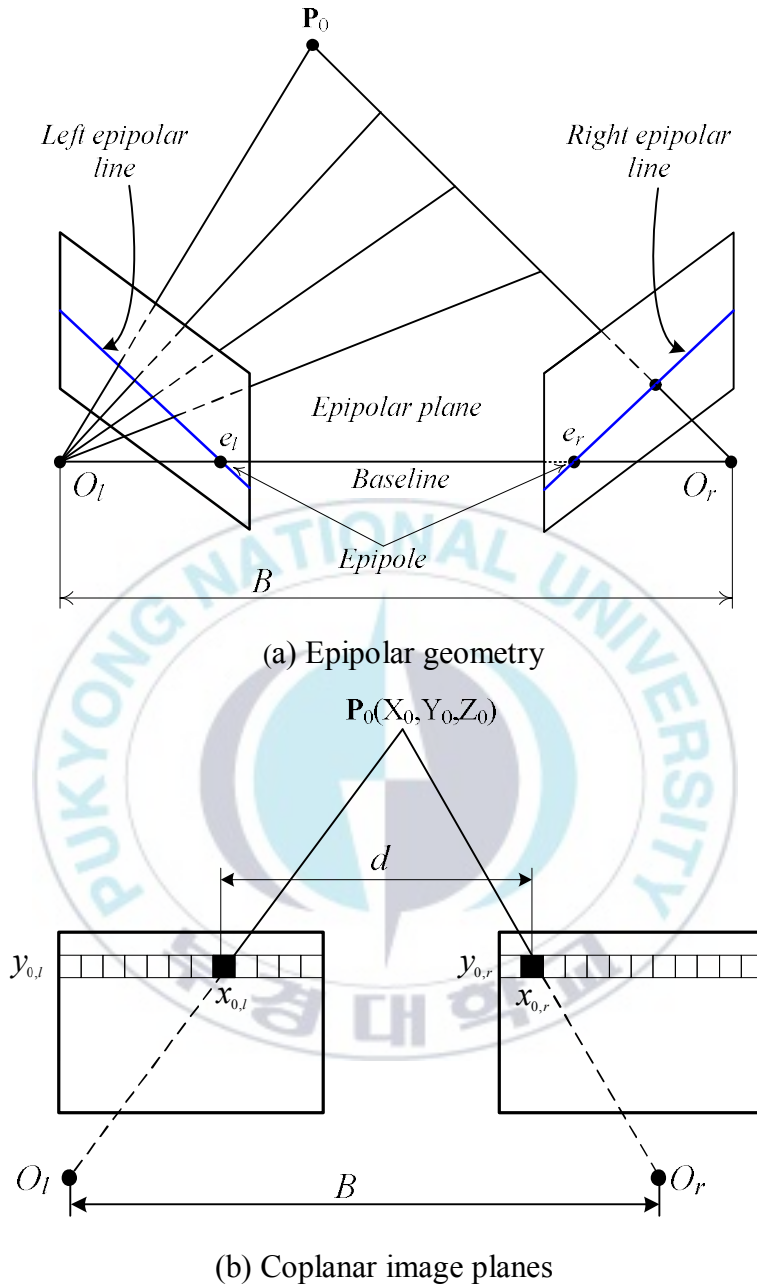


Fig. 2.15 Two pinhole camera models.

Fig. 2.15(a) is a schematic of the epipolar geometry associated with two pinhole camera models. Fig. 2.15(b) is the two cameras that have

coplanar image planes and *co-linear* and *x-axis*. The right camera is arbitrarily chosen as the reference camera. In the figure, left and right cameras do not have coplanar image planes. Nonetheless, this serves as a good opportunity to briefly discuss epipolar geometry. An epipole is defined as the point of centroid of the image planes with the epipolar line joining the optical centers of the left and the right cameras ( $e_l$  and  $e_r$  in Fig. 2.15(a)). When a point is seen in the reference image, its location in the other image could be anywhere along the epipolar line generated by the centroid of the epipolar plane (i.e., the plane formed by the epipoles  $e_l$  and  $e_r$  and the point  $\mathbf{P}_0$ ) with the image plane of the other camera.

Now consider the case of two pinhole cameras which have coplanar image planes, parallel optical axes, and colinear *x-axis* separated by a distance  $B$  as shown in Fig. 2.15(b). In this particular case, the epipolar geometry reduces the epipoles of both cameras to lie on the same rows in each image plane. The epipolar lines coincide with horizontal rows of the image and image point correspondences can be reduced to search along rows. The epipolar line associated with a point  $\mathbf{P}_0$  is reduced to the same horizontal row at which the point was detected in the reference image.

The disparity  $d_0$  is defined as pixel distance between the image point of  $\mathbf{P}_0$  in the reference camera ( $\mathbf{p}_{0,r} = (x_{0,r}, y_{0,r})$ ) and the correspondent point found in the secondary image ( $\mathbf{p}_{0,l} = (x_{0,l}, y_{0,l})$ ) as follows:

$$d_0 = x_{0,l} - x_{0,r} \quad (2.66)$$

By knowing the disparity and the separation distance between cameras (baseline)  $B$  and using similar triangles, the following relation can be used to determine the depth associated with  $\mathbf{p}_{0,r}$ :

$$Z_0 = \frac{f \cdot B}{B - d_0} \quad (2.67)$$

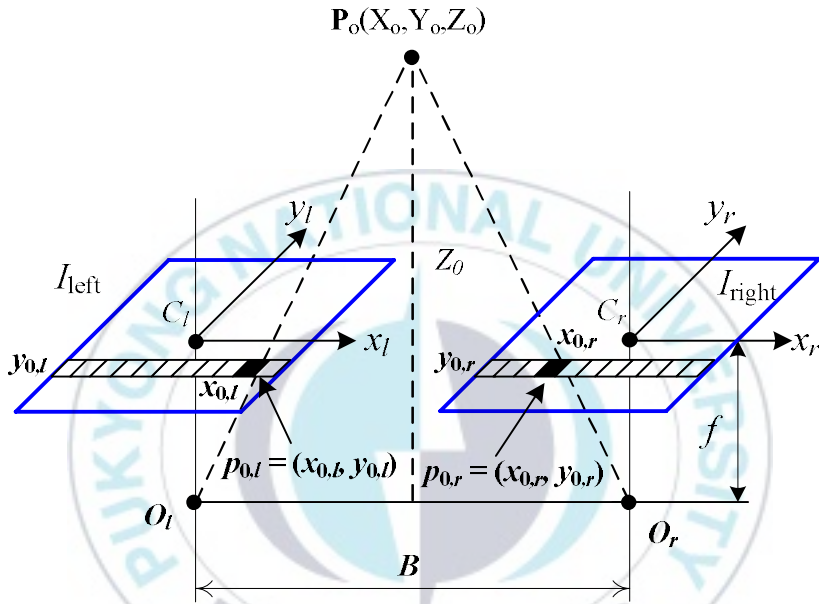


Fig. 2.16 Triangulation of two pinhole camera models.

By using similar triangles from Fig. 2.15(a), a point in 3D Euclidean space  $(X, Y, Z)$  can be transformed into the image coordinate using the following relation:

$$\begin{cases} x = \frac{f \cdot X}{Z} \\ y = \frac{f \cdot Y}{Z} \end{cases} \quad (2.68)$$

With  $Z_0$  known, the distance in  $X_0$  and  $Y_0$  can be deduced from equations as shown in Fig. 2.16.

$$\begin{cases} X_0 = \frac{x_{0,l} \cdot Z_0}{f}, \text{ or } X_0 = \frac{(B + x_{0,r}) \cdot Z_0}{f} - B \\ Y_0 = \frac{y_{0,l} \cdot Z_0}{f}, \text{ or } Y_0 = \frac{y_{0,r} \cdot Z_0}{f} \end{cases} \quad (2.69)$$

By repeating the above calculations for all pixels  $p_{i,r}$  in the reference image, a 3D depth image can be easily produced.

## 2.4 Moving object tracking with Kalman filter

By using the real-time image segmentation algorithm, it can obtain the center positions of moving objects as detected. Because the presence of the noise on the environment, sometimes an object's centroid of a moving object does not indicate its accurate location. The position needs to be determined further to track each object. Through the contour tracking approach described in this section, it is possible to obtain a real position of each object.

### 2.4.1 Typical Kalman filter

Typical Kalman Filter (KF) addressed the problem of extracting the useful signal from noisy measurement variables [56]. Kalman filter is a mathematical estimator that predicts and corrects the states of a wide range of linear processes [57].

In Kalman filter, consider a tracking system, and subscript  $k$  indicates the discrete time. The objective of the typical KF is to estimate a state vector at the present time for the measurement at the

previous time. The mathematical description of the typical Kalman filter is as follows:

### 1. Process equation

By assuming that the velocity is constant during the sampling interval, the process equation is expressed as follows:

$$x_k = \mathbf{A}x_{k-1} + w_{k-1} \quad (2.70)$$

where  $\mathbf{A}$  is the transition matrix and  $x_k$  is the state vector at a present time  $k$ ,  $x_{k-1}$  is the state at the previous time  $k-1$ , and  $w_{k-1}$  is the Gaussian process noise  $N(\cdot)$  with the following normal probability distribution  $p(w)$  as follows:

$$p(w) \sim N(0, Q) \quad (2.71)$$

where  $Q$  is the process noise covariance matrix.

### 2. Measurement equation

$$z_k = \mathbf{H}x_k + v_k \quad (2.72)$$

where  $\mathbf{H}$  is the measurement matrix and  $z_k$  is the measurement vector at the present time  $k$ ,  $v_k$  is a measurement noise vector with the Gaussian measurement noise  $N(\cdot)$  with normal probability distribution  $p(v)$  as follows:

$$p(v) \sim N(0, R) \quad (2.73)$$

where  $R$  is the measurement noise variance matrix.

### 3. Time update equations

Eqs. (2.68) and (2.70) describe a linear model at the present time  $k$ . As  $x_k$  is unmeasurable directly, the measurement vector  $z_k$  is used to update the unknown states  $x_k$ . Apriori estimate state vector  $\hat{x}_k^-$  and a estimate covariance error  $\hat{x}_k$  is obtained for the next time step  $k$  as follows:

$$\hat{x}_k^- = \mathbf{A}\hat{x}_{k-1}^- + w_k \quad (2.74)$$

The estimate variance  $P_k^-$  is the mean squared error in the estimate  $\hat{x}_k^-$  as follows:

$$P_k^- = \mathbf{A}P_{k-1}\mathbf{A}^T + Q \quad (2.75)$$

where  $P_{k-1}$  is a matrix representing error covariance in the state prediction at time  $k-1$  and  $Q$  is the process noise covariance (or the uncertainty in our model of the process).

#### 4. Measurement update equations

These equations are associated with the feedback of the system. The objective is to estimate aposteriori estimating  $\hat{x}_k$  which is a linear combination of a priori estimate  $\hat{x}_k^-$  and the new measurement vector  $z_k$ . The equations are given as follows:

$$K_k = P_k^- \mathbf{H}^T (\mathbf{H}P_k^- \mathbf{H}^T + R)^{-1} \quad (2.76)$$

$$\hat{x}_k = \hat{x}_k^- + K_k (z_k - \mathbf{H}\hat{x}_k^-) \quad (2.77)$$

$$\hat{x}_k = \hat{x}_k^- + K_k (z_k - \mathbf{H}\hat{x}_k^-) \quad (2.78)$$

where  $K_k$  is the Kalman gain computed by measurement update equations at time  $k$ . After that aposteriori state estimate  $\hat{x}_k$  and aposterior error estimate  $P_k$  are computed by the measurement  $z_k$  at time  $k$ . The time and measurement equations are calculated recursively with previous aposteriori estimates to predict new apriori estimate. This recursive behavior of estimating the states is one of the highlights of the Kalman filter.

### 2.4.2 Multi-object tracking using Kalman filter

The geometric of object features include location, shape, and center of mass (centroid) of a moving object, etc. This proposed method uses camera with sampling time 30 fps. Thus the size of the center position and the tracking window of the moving object in the adjacent two frames are little changed. Therefore, the centroid and the size of the tracking window as the feature value to describe a moving object is chosen.

The Kalman filter for the tracking model consists of three sub-modules: the motion model, feature matching, and the model update. These three sub-modules are described as follows:

#### 1. Motion estimation model

The Kalman filter used to track objects is defined in terms of the motion model, and the measurement equation as follows:

$$\mathbf{X}_k = [x_{0,k}, y_{0,k}, l_k, h_k, v_{x,k}, v_{y,k}, v_{l,k}, v_{h,k}]^T \quad (2.79)$$

where,  $x_{0,k}$ ,  $y_{0,k}$  represent horizontal and vertical coordinate centroids,  $l_k$ ,  $h_k$  represent half-width and half-height of the tracking window,

$v_{x,k}, v_{y,k}, v_{l,k}, v_{h,k}$  represent their speeds at time  $k$ , respectively. The next is  $\{(x_k, y_k) | k = 1, \dots, m\}$  represent the location information for the  $k^{\text{th}}$  detected object in  $x$ -axis and  $y$ -axis directions, and  $\{(v_k, v_k) | k = 1, \dots, m\}$  represent the velocity of the  $k^{\text{th}}$  object.

The measurement vector of the system at time  $k$  adopts the following form:

$$z_k = [x_{0,k}, y_{0,k}, l_k, h_k]^T \quad (2.80)$$

The moving model for the  $k^{\text{th}}$  object is defined by a nonlinear system as follows:

$$\begin{cases} x_k(n) = x_k(n-1) + v_{xk}(n-1)dt \\ y_k(n) = y_k(n-1) + v_{yk}(n-1)dt \end{cases} \quad (2.81)$$

where  $n$  is number of objects

In the following,  $A$  is the transition matrix and  $H$  is the measurement matrix of the tracking system along with the Gaussian process  $w_k$  and measurement noise vector  $v_k$ . The noise value is entirely dependent on a tracking object and the settings are adjusted empirically. Accordingly, the transition matrix  $A$  with  $k = 1, \dots, m$  can be represented as follows:

$$A = \begin{bmatrix} A_1 & 0 & \dots & 0 \\ 0 & A_k & & \vdots \\ \vdots & & \ddots & 0 \\ 0 & \dots & 0 & A_m \end{bmatrix} \quad (2.82)$$

where

$$A_i = \begin{bmatrix} 1 & dt & 0 & 0 & 0 & 0 & 0 & 0 \\ 0 & 1 & dt & 0 & 0 & 0 & 0 & 0 \\ 0 & 0 & 1 & 0 & 0 & 0 & 0 & 0 \\ 0 & 0 & 0 & 1 & 0 & 0 & 0 & 0 \\ 0 & 0 & 0 & 0 & 1 & 0 & 0 & 0 \\ 0 & 0 & 0 & 0 & 0 & 1 & dt & 0 \\ 0 & 0 & 0 & 0 & 0 & 0 & 1 & dt \\ 0 & 0 & 0 & 0 & 0 & 0 & 0 & 1 \end{bmatrix} \quad (2.83)$$

where  $dt$  is time step.

Measurement matrix  $H$  can be described as follows:

$$H = \begin{bmatrix} 1 & 0 & 0 & 0 & 0 & 0 & 0 & 0 \\ 0 & 1 & 0 & 0 & 0 & 0 & 0 & 0 \\ 0 & 0 & 1 & 0 & 0 & 0 & 0 & 0 \\ 0 & 0 & 0 & 1 & 0 & 0 & 0 & 0 \end{bmatrix} \quad (2.84)$$

After the state equation and the measurement equation of a motion model are defined in the next frame, Kalman filter can be used to estimate the object's location and size in a small range, and to get trajectories of moving objects.

## 2. Feature matching

A centroid and a tracking window are describing state of each moving object, the horizontal and vertical coordinates centroid and the area of the  $i^{\text{th}}$  object in the  $k^{\text{th}}$  frame are described as  $x_k^i$ ,  $y_k^i$ , and  $S_k^i$ , respectively.

The first one is the centroid distance function between the  $i^{\text{th}}$  object in the  $k^{\text{th}}$  frame and the  $j^{\text{th}}$  object in the  $(k+1)^{\text{th}}$  frame represented as follows:

$$D(i, j) = \frac{\left| \sqrt{(x_k^i - x_{k+1}^j)^2 + (y_k^i - y_{k+1}^j)^2} \right|}{\text{Max} \left| \sqrt{(x_k^i - x_{k+1}^j)^2 + (y_k^i - y_{k+1}^j)^2} \right|} \quad (2.85)$$

The second one is the area difference between the  $i^{\text{th}}$  object in the  $k^{\text{th}}$  frame and the  $j^{\text{th}}$  object in the  $(k+1)^{\text{th}}$  frame is as follows:

$$A(i, j) = \frac{\left| S_k^i - S_{k+1}^j \right|}{\text{Max} \left| S_k^i - S_{k+1}^j \right|} \quad (2.86)$$

where  $S_k^i = 4l_k^i h_k^i$  is the area of the tracking window  $k^{\text{th}}$  frame of the  $i^{\text{th}}$  object.

The smaller the value is, the closer the two objects' shape is. With these definitions, the cost function is defined as follows:

$$V(i, j) = \alpha D(i, j) + \beta A(i, j) \quad (2.87)$$

where  $\alpha + \beta = 1$ ,  $\alpha=0.8$ ,  $\beta=0.2$ . The smaller the cost function's value is, the two objects are more likely to have correspondence.

### 3. Model update

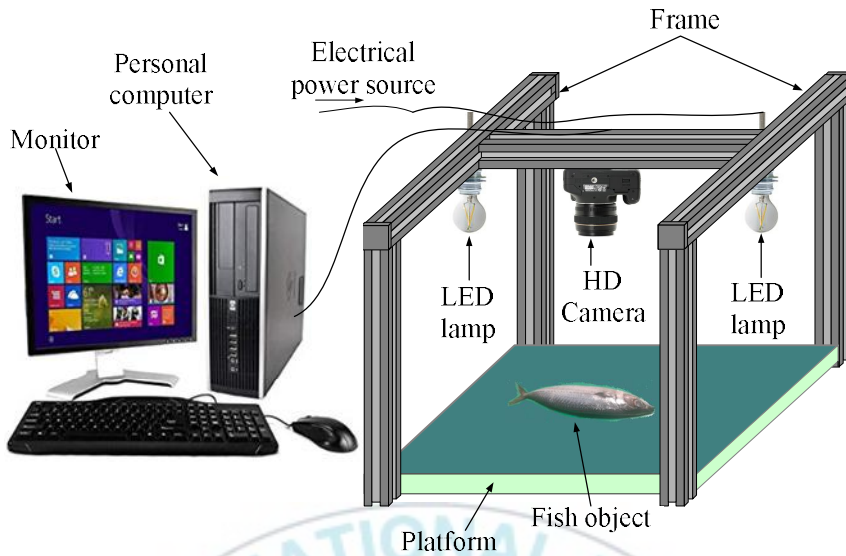
To find the minimum value of the cost function, use the feature of the first frame to update parameters of the Kalman filter motion model. This frame is used as the input in the next frame. The process is done until the moving objects disappeared.

## **Chapter 3: System Description**

This chapter describes the three structure hardwares used for the proposed measurement methods for fish surface area and volume. The first one is structure hardware used for a proposed analytic measurement method and a proposed partition measurement method in chapter 4. The second one is structure hardware used for a proposed real-time measurement method in chapter 5. The third one is structure hardware used for a proposed real-time measurement method for moving object in chapter 6.

### **3.1 Structure hardware of a proposed analytic and partition measurement methods**

The computer vision system used for calculating the fish surface area and volume consists of software and hardware. The software for image processing is designed in Matlab programming language. The structure hardwares of image acquisition is developed to measure a fish shape object. The structure hardwares consists of one personal computer (PC), one monitor screen, two LED lamps, one high density (HD) camera, one platform, and one frame as shown in Fig. 3.1. This structure hardware is used for a proposed analytic and partition measurement methods in chapter 4.



Parts	Descriptions
Personal computer	Intel® Core™ i3-3220 @3.30Hz 8GB
Monitor screen	19" LCD Samsung
LED lamp	8W – 220 V
HD camera	Canon; EOS 550D, Japan
Platform	Plywood
Frame	Aluminum profiles

Fig. 3.1 Structure hardware of the proposed analytic and partition measurement methods

### 3.2 Structure hardware of a proposed real-time measurement method

In this dissertation, the ZED stereo camera as a stereo camera is used. The ZED stereo camera has output resolution of  $4,416 \times 1,242$  pixels at 15 frames per second (fps) and  $3,840 \times 1,080$  pixels at 30 frames per second (fps), the depth range of 0.5 – 20 m, baseline of 120 mm, and field of view  $110^\circ$ . The ZED is a 3D stereo camera for depth sensing, motion, tracking and real-time 3D reconstruction [58]. The prototype of a stereo camera to determine a 3D coordinate is shown in Fig. 3.2.

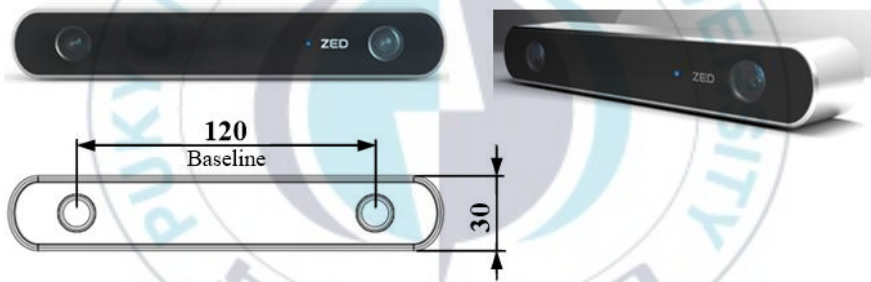
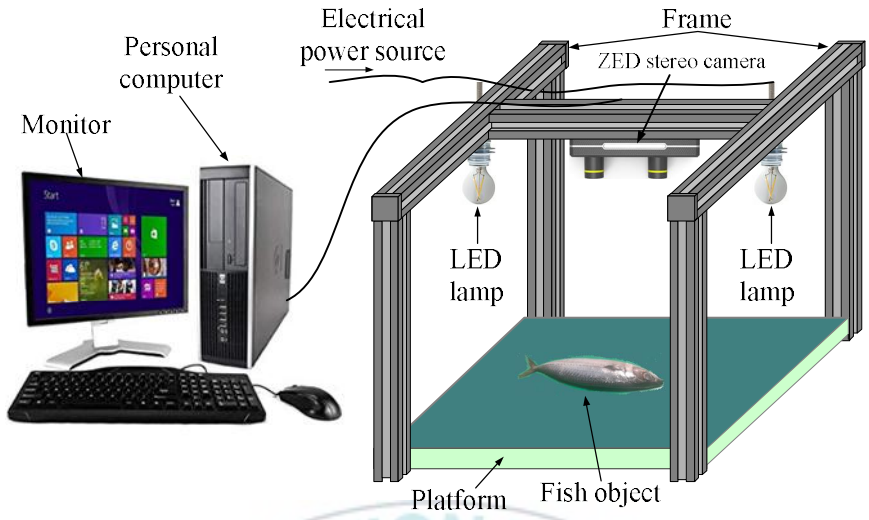


Fig. 3.2 Prototype of ZED stereo camera

The hardware structure for real-time image segmentation is shown in Fig. 3.3. The hardware structure consists of a personal computer, one ZED stereo camera, two light sources, and a platform. All tests are done using a personal computer with an Intel Core(TM) i3-3220 CPU @ 3.3GHz and 8 GB of ram with a Windows 7 64-bit operating system. This structure hardware is used for a proposed real-time measurement method in chapter 5.



Parts	Descriptions	
Personal computer	Intel® Core™ i3-3220 @3.30Hz 8GB	
Monitor screen	19" LCD Samsung	
LED lamp	8W – 220 V	
Platform	Plywood	
Frame	Aluminum profiles	
ZED stereo camera	Resolution	4,416 × 1,242 pixels
	Depth range	0.5 – 20 m
	Baseline	120 mm
	Field of view	110°

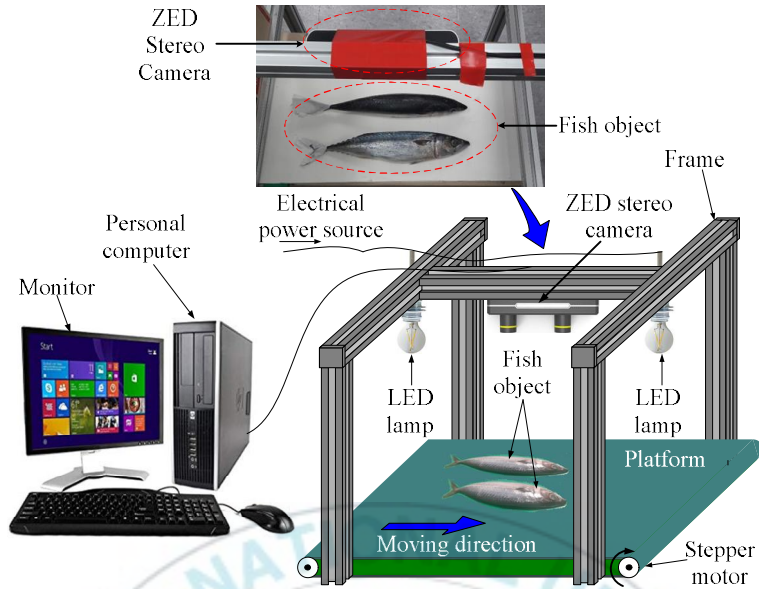
Fig. 3.3 Hardware structure of a proposed real-time measurement method

The camera device for video input is a ZED stereo camera as a stereo camera. Hardware structure and software are developed to perform real-time image segmentation of fish shape object similarly to the real fish processing line. The software used for image processing and analysis is open source computer vision (OpenCV, C++) with visual studio compiler.

### **3.3 Structure hardware of a proposed real-time measurement method for moving objects**

The targeting objects are the fish placed on the moving platform. The stereo camera is mounted perpendicular to the moving platform. The stereo camera uses a ZED stereo camera, as explained in section 3.2. Image processing on the video stream is developed in C++ by using the Qt framework, open source computer vision library (OpenCV), and the visual studio compiler. The hardware structure used for a proposed visual moving consists of a personal computer, one ZED stereo camera, two light sources, and platform. All tests are done using a personal computer with an Intel Core(TM) i3-3220 CPU @ 3.3GHz and 8 GB of ram with a Windows 7 64-bit operating system.

The testing environment is constrained to a solid color background in the back of the scene. Solid color background intends to minimize scene noise. Thus, the work can focus on applying the algorithm rather than solving noise problems. Fig. 3.4 shows the structure of the proposed visual moving method. This structure hardware is used for a proposed real-time measurement method for moving objects in chapter 6.



Parts	Descriptions	
Personal computer	Intel® Core™ i3-3220 @3.30Hz 8GB	
Monitor screen	19" LCD Samsung	
LED lamp	8W – 220 V	
Platform	Plywood	
Frame	Aluminum profiles	
Fish ZED stereo camera	Resolution	4,416 × 1,242 pixels
	Depth range	0.5 – 20 m
	Baseline	120 mm
	Field of view	110°
Stepper motor	24 V DC	

Fig. 3.4 Hardware structure of the proposed real-time measurement method for moving objects

## **Chapter 4: Analytic and Partition Measurement Method for Fish Surface Area and Volume**

This chapter proposes an analytic and partition measurement method for fish surface area and volume. This measurement method is built in offline and uses digital images captured by HD camera as object measurement. The measurement system was explained in Fig. 3.1 of section 3.1. In the application, the partition method uses image processing methods for calculating the fish surface area and volume. The fishes are considered as ellipsoid shapes on three view sides to appropriate analytical models for estimating their surface area and volume. To calculate the surface area and volume of fish using the partition method, Eqs. (2.34) ~ (2.7) in section 2.1.2.1 chapter 2 are used. The calculation results using partition method are compared to the analytical method using Eq. (2.19) and Eq. (2.22) in section 2.1.1.1 and section 2.1.1.2, respectively. To do this task, the followings are done. Firstly, image acquisition and calibration are done. Secondly, fish image shape is segmented to determine surface area and volume for computation. Thirdly, surface area and volume of fish are calculated by image processing methods. Finally, the effectiveness of the partition measurement method is compared with that of the analytical method through experimental results.

The software is built to process the images of fish and to perform calculations for its surface area and volume using information extracted from the proposed partition method. The image processing algorithm is built in Matlab programming language. The processing step

for calculating fish surface area and volume consists of image calibration, image acquisition, preprocessing, image segmentation, feature extraction, and calculating of fish surface area and volume as shown in Fig. 4.1

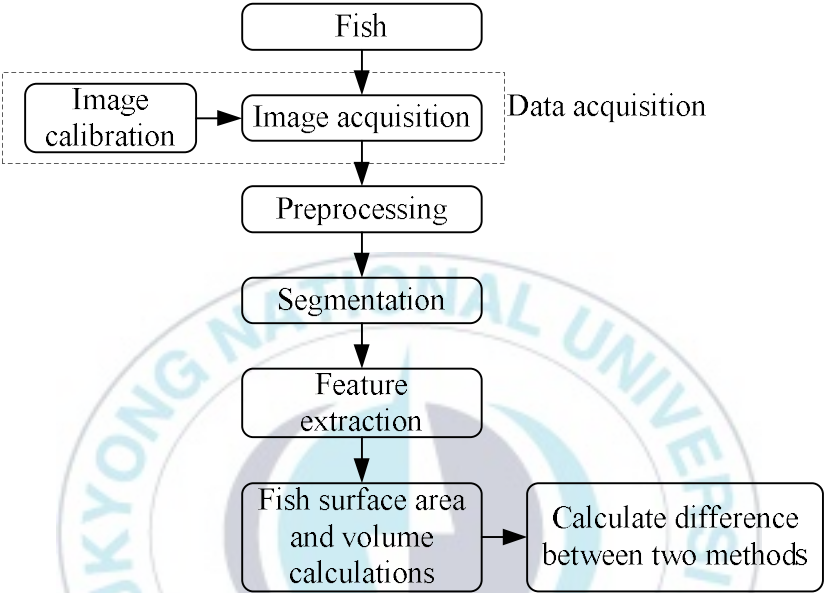


Fig. 4.1 Processing step for calculating fish surface area and volume

**4.1 Data acquisition**

The data acquisition stage of this proposed method consists of two parts: image acquisition and image calibration. For image acquisition, the fishes are captured to acquire digital profile images. The profile images are extracted as image segmentation used for calculating surface area and volume. For image calibration, the actual dimension of the fish is measured and used for finding a calibration constant value to calculate surface area and volume from shape features extracted from profile images of the fish.

#### 4.1.1 Image acquisition

The images of fish are captured by using HD camera located on the top of the fish object. The HD camera is a camera with two-dimensional array of light sensing elements on a chip. The sensor element is placed spatially to fit the pixels in an image. These sensors form the values of red, green and blue (RGB) for each pixel in the output digital image as they are exposed to light. Thus, the RGB image consists of three intensity ribbon matrices for R, G, and B. Each of the bands forms a grayscale image. Conventionally, intensity values usually range from 0 (dark) to 255 (bright), but they are also often scaled to run from 0 to 1 so that they can be interpreted as full intensity proportions.

Each sample of the fish is placed on plywood with green color to control the light level when photographs are taken. Each sample image is taken using an HD camera as shown in Fig. 4.2 below. The sample picture is taken in two positions, i.e. top view and side view. For image analysis, each sample image is converted into binary image. The pixel which is generated by the binary image is processed using the image processing mentioned in chapter 2. Pixels of each fish image are used to calculate the surface area and volume of fish.

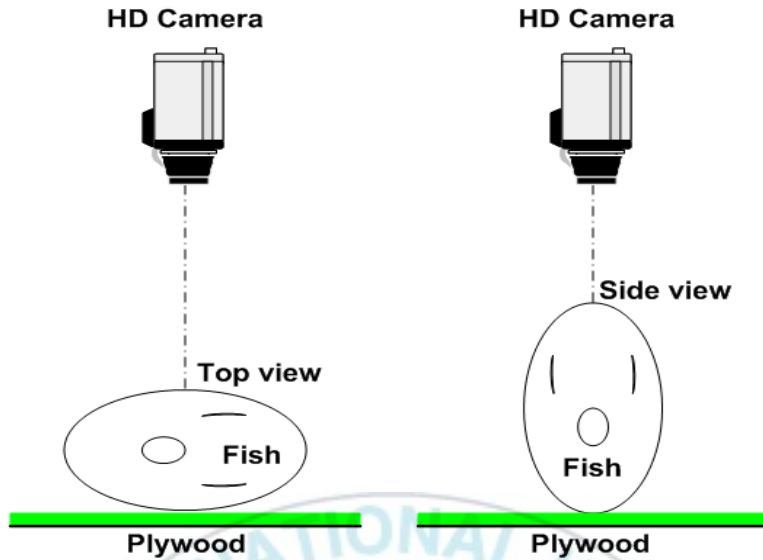


Fig. 4.2 Top view and side view of image acquisition

#### 4.1.2 Image calibration

The fish image is calibrated for size by using one sample image captured by HD camera. The physical dimension of the fish in millimeter are measured by using vernier caliper. The image calibration result of one fish object is used as a calibration constant value for measuring fish surface area and volume measurement. The size in millimeter is obtained by measuring the number of pixels from the outermost distance of the fish images as shown in Fig. 4.3. The fish image processing results used for image calibration is shown in Fig. 4.4. An example of one fish has its dimension of 290 mm (L) x 51.1 mm (H) x 38.22 mm (W), and calibration result is obtained as 1 pixel = 0.0251 mm for (L), 1 pixel = 0.00557 mm for (H), and 1 pixel = 0.00475 mm for (W) .

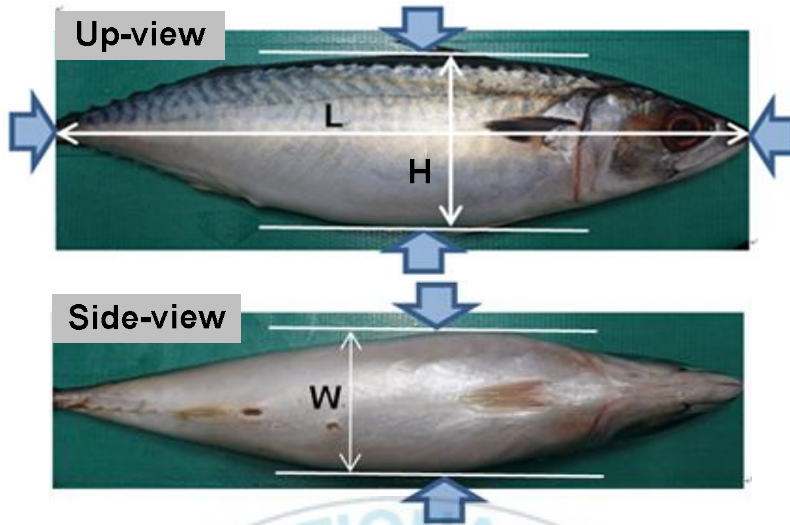


Fig. 4.3 Fish measured from two sides by using vernier caliper

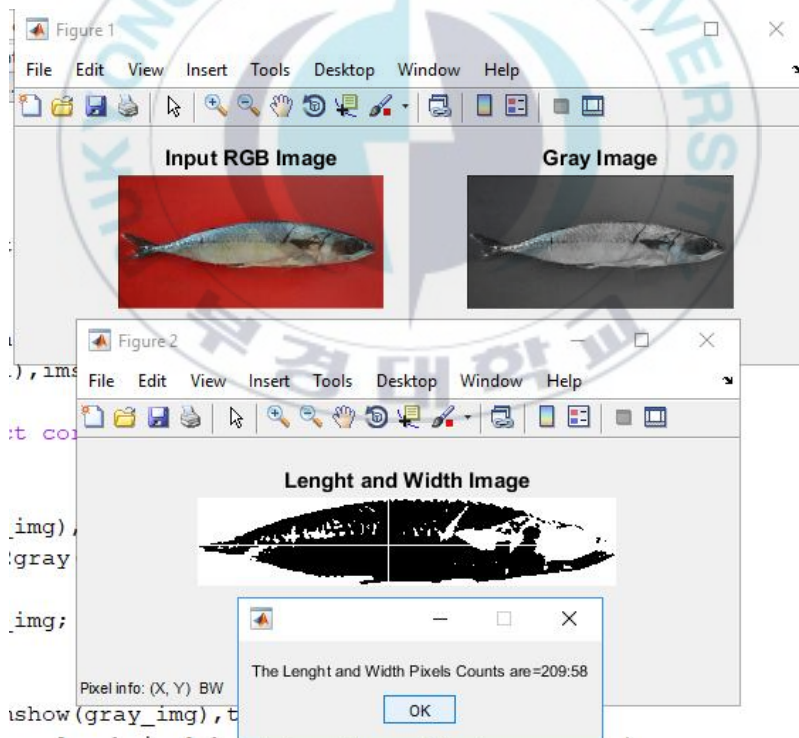


Fig. 4.4 Fish image processing results used for image calibration

Table 4.1 Algorithm to perform fish surface area and volume calculations using Matlab

<b>Algorithm 1.</b> Algorithm to perform fish surface area and volume calculations using Matlab	
1.	<b>Input image:</b> image file captured by HD camera in format joint photographic experts group (.jpg). Resize the two dimensional input image
2.	Read the image; image1, image2
3.	Get the number of clusters to be formed
4.	Convert the color image into hsv image
5.	Convert the color image into its corresponding gray image: $h = \text{hsv}(:, :, 1);$ ( Hue image). $s = \text{hsv}(:, :, 2);$ ( Saturation image). $v = \text{hsv}(:, :, 3);$ ( Value /intensity image).
6.	Convert a grayscale image into a black-white (bw) image with corresponding bw level
7.	Create an array consisting of all ones and find edges
8.	Apply morphology erosion to bw image with ones
9.	Creates a square structure element with a width of pixels.
10.	Apply morphology closing to “bw image with ones” by adding square structure element
11.	Remove small objects from binary images by applying area opening
12.	Apply image complement to change black image to white image.
<b>Output image as Segmented_1 and Segmented_2</b>	
Pseudo-code implementation to calculate fish surface area and volume using image output Segmented_1 and Segmented_2	
13.	$s=0;$ <input type="checkbox"/> <b>Set s for beginning</b> $v=0;$ <input type="checkbox"/> <b>Set v for beginning</b> $b\_old=0;$ $c\_old=0;$ $cal\_h;$ <input type="checkbox"/> <b>Set h calibration constant</b> $cal\_v;$ <input type="checkbox"/> <b>Set v calibration constant</b> for $i=1:\text{size}(bw1,1)$ ; $b=\text{size}(i);$ $s1=0;$

	<pre> v1=0; for j=1:size(bw1,2) if (bw1(i,j)==1) b=b+1; end end end for k=1:size(cw1,1); c=size(i); s1=0; v1=0; for l=1:size(bw1,2) if (bw1(k,l)==1) c=c+1; end end s1=pi.*cal_h.*cal_v.*((b_old+b)+(c_old+c))/2; v1=pi/2*cal_h.*cal_v.*((b_old.*c_old)+(b.*c)); s=s+s1; v=v+v1; b_old=b; c_old=c; end surface=num2str(s,5); volume=num2str(v,5); </pre>
15.	<pre>surface=num2str(s,5);</pre> <input type="checkbox"/> <b>Fish surface area result</b>
16.	<pre>volume=num2str(v,5);</pre> <input type="checkbox"/> <b>Fish volume result</b>

## 4.2 Image processing and analysis

**Algorithm 1** proposed in Table 4.1 is the algorithm to perform the fish surface area and volume calculations by using image processing methodology. This algorithm are executed in Matlab programing language.

### 4.2.1 Preprocessing

The first stage to process the fish image before the segmentation process is resizing. For the example, the original image captured by HD camera has 1280×1024 pixels frame resolution. The image with 1280×1024 pixels frame resolution is a large image and would be very computationally time-consuming for image processing. For this reason, each image needs to be resized to form smaller images of the relevant portions for future processing. The process of forming a resized image for each fish is summarized in Fig. 4.5.

An original image with 622×311 is resized to 447×105 pixels resolution image. This image will be used in segmentation and feature extraction to obtain segmented image.

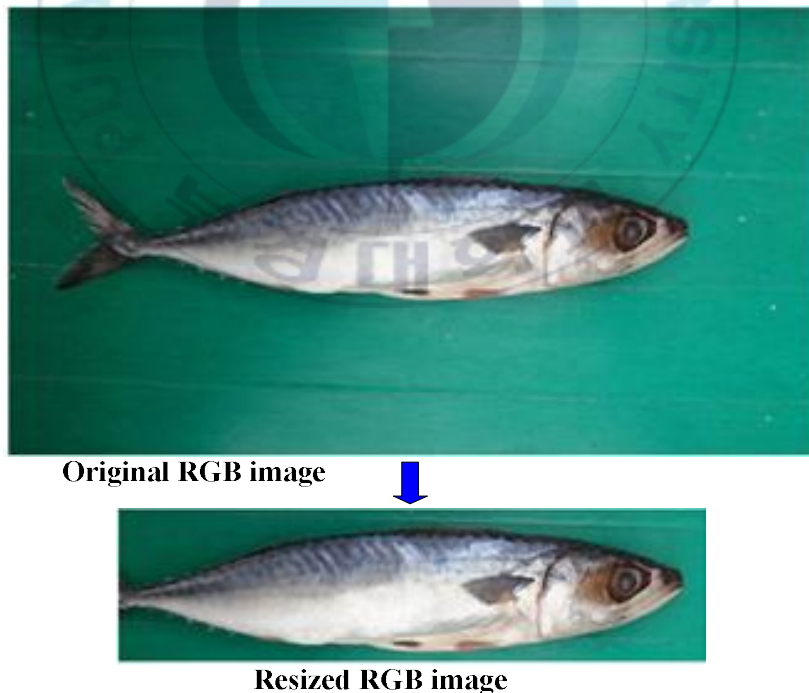


Fig. 4.5 Process of forming a resized image

### 4.2.2 Image segmentation and feature extraction

Fig. 4.6 shows the flowchart of image segmentation and feature extraction. Feature extraction is a prerequisite for image segmentation. Extracting an image is a procedure to segment a particular shape or structure in an image. The contour of the fish is extracted from digital images captured by the camera. The steps of extracting an image are image segmentation, noise reduction, and edge detection. The image threshold is used as an image segmentation. Generally, a grayscale image is transformed into binary images as follows:

$$g(x, y) = \begin{cases} 1 & \text{if } f(x, y) \geq T_h \\ 0 & \text{if } f(x, y) < T_h \end{cases} \quad (4.1)$$

where  $g(x, y)$  is the binary image of the grayscale image  $f(x, y)$  and  $T_h$  denotes the threshold value. In this case, the best threshold selection is done manually. Since the Gaussian filtering method allows the edge to be preserved in filtering out the unwilling noises, it is then employed to reduce noises within the segmented image. Finally, the edge of the fish is detected by the Sobel edge detector from an image filtering noises using the Gaussian filtering method.

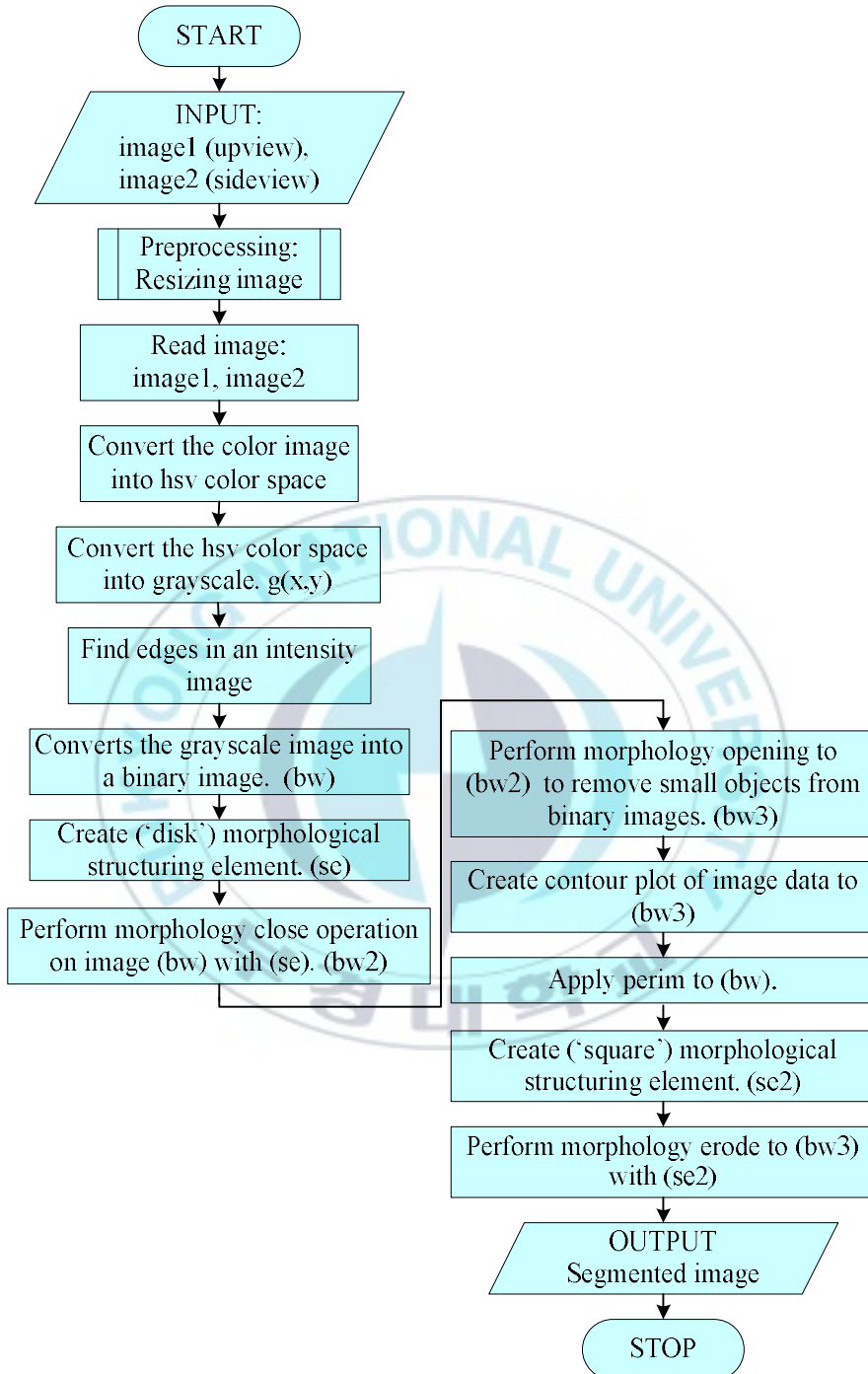
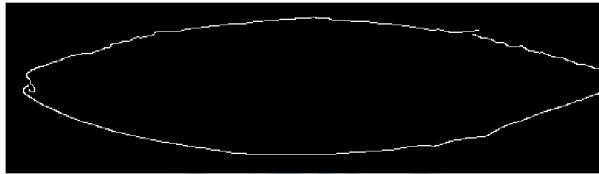


Fig. 4.6 Flowchart of image segmentation and feature extraction

Fig. 4.7 shows results of fish image segmentation and shape extraction.



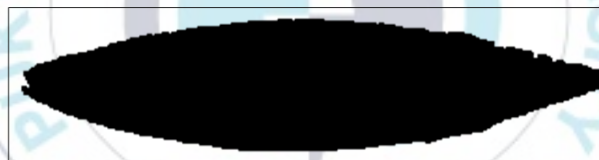
(a) Grayscale image



(b) Segmented edge image with Sobel edge detection



(c) Extracted contour image



(d) Thresholded image with noise filtering and filling holes inside the extracted edge image (c)



(e) Image complement of the image (d)



(f) RGB color image with the extracted contour image

Fig. 4.7 Results of fish image segmentation shape extraction

Fig 4.7(a) is a fish grayscale image. This image is an image that contains noise. Fig 4.7(b) is a segmented edge image with applying Sobel edge detection. Fig 4.7(c) is an extracted contour image from the edge image. This image is obtained by creating a contour plot to the binary image resulted from performing morphology closing and opening. Fig. 4.7(d) is a thresholded image with noise filtering and filling holes inside the extracted contour image from Fig. 4.7(c). Fig 4.7(e) is the image complement of image in Fig. 4.7(d), and Fig. 4.7(f) is a final process of image segmentation by combining the original RGB color image and the extracted contour. The result in Fig. 4.7(f) shows that the original RGB color fish image is successfully partitioned from the background image. Next step for image analysis used in this dissertation will use this result.

### **4.3 Experimental results**

#### **4.3.1 Image segmentation results**

Fig. 4.8 shows images converted from the RGB color images (a) and (b) into the HSV color images (c) and (d) in upview and sideview of a fish. The image segmentation is implemented based on the color threshold approach. In this case, the threshold value ( $Th$ ) is done manually, and the RGB images are converted into HSV color images without any modifications or improvement method. Fig. 4.9 shows the grayscale images (a) and (b) with a threshold corresponding to an intensity RGB image.

Images in Fig. 4.8(a)~(b) contain large amounts of noise. Fig. 3.10 shows holes when these images in Figs. 4.10(a) and (b) are converted

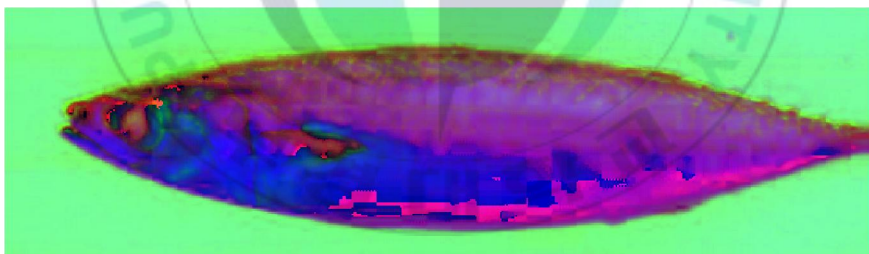
to black and white (bw) format. They have holes in the parts of the fish body. To solve this problem, a smoothing filter is applied. This discussion in detail is carried out in section 4.3.2.



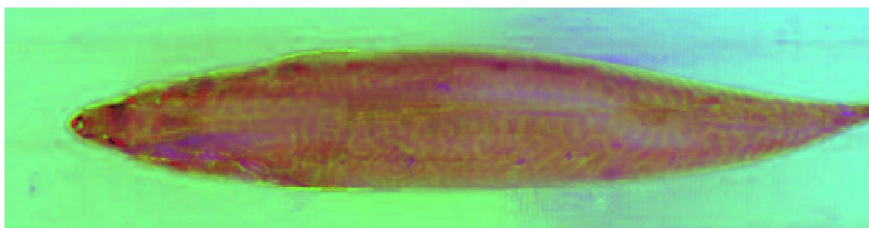
(a) RGB color image: upview



(b) RGB color image: sideview

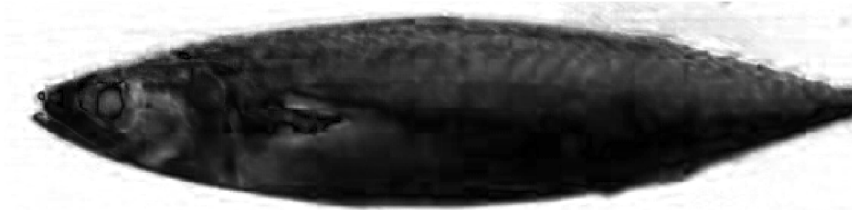


(c) HSV color image: upview

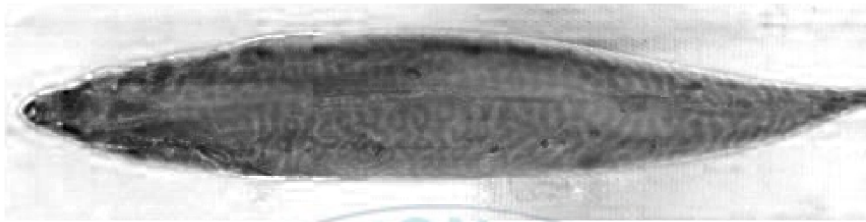


(d) HSV color image: sideview

Fig. 4.8 RGB images and HSV images in upview and sideview

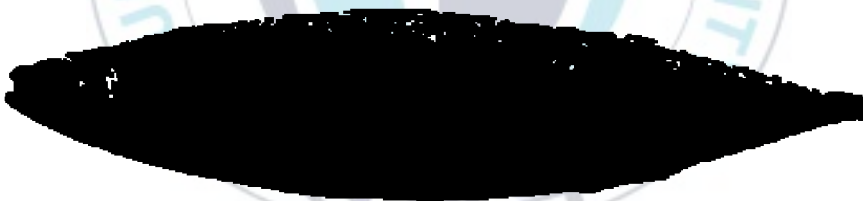


(a) Grayscale image: upview



(b) Grayscale image: upview

Fig. 4.9 Upview and sideview grayscale images



(a) Upview



(b) Sideview

Fig. 4.10 Upview and sideview bw images with noise

### 4.3.2 Contour extraction and region filling

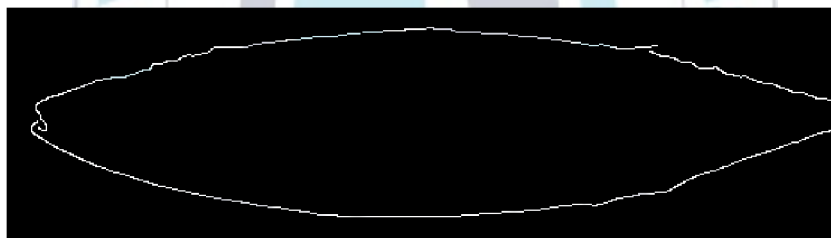
Defected fish skin has the color different from healthy skin. A defected part of the fish skin leads to false segmentation, and is often segmented as the foreground of the object. Fig. 4.10 shows of a fish skin bw images. The figure show holes in the body of the fish, but these are not the foreground. To solve this problem, mathematical morphology, a contour extraction, and region filling technique are applied.

Scanning pixel is performed to seek the contour point. The list of pixels belonging to the shape is the white color, and the different color of the pixels which are not part of the shape is the black color. For the left contour of the object, the pixel is scanned from left to right and from bottom to top in the image. In each scan line of the image, the pixel is judged from left to right whether it belongs to the foreground object. When the current pixel belongs to the object, this scanning process is a break and goes to the next scan line. The same rule is applied to every scan line. Therefore, left side contour is extracted and each pixel in the contour is marked. This process is performed on all other three directions in turn: from top to bottom, from right to left, and from bottom to top. In each contour extraction process, those marked pixel is not scanned again. The region wrapped by the four contours is decided as a final foreground region. In this extraction process, the coordinate of every pixel in contour are recorded for the next step, region filling. Note that this approach is only effective for the binary image.

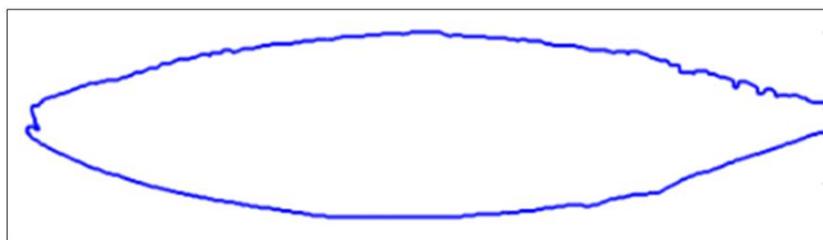
For a pixel in the contour, its coordinate is recorded in the above process. All pixels, which are scanned before this contour pixel is

encountered, are set as background. Pixels that are not scanned in the contour extraction process are set as a foreground object. So the contour region is filled.

Fig. 4.11 shows the segmented image by edge detection and contour extraction. Fig 4.11(a) is Sobel edge detection result applied to a segmented image. Fig. 4.11(b) shows the contour object extracted from a binary image resulted from performing morphology closing and opening. The contour of the fish object is acquired, and the contour line is smooth. Fish surface area and volume can be also obtained by counting the pixel number in the contour. To count the number of pixels in the extracted contour image, the gray value is 255. From this, the number of pixels in the image after region filling can be calculated. Furthermore, the perimeter of the image can also be calculated.



(a) Using Sobel edge detection method



(b) Contour extraction using morphology closing and opening

Fig. 4.11 Segmented image by edge detection and contour extraction

Fig. 4.12 shows the region filling result the fish image. It shows that the region are entirely filled for upview image and sideview image. Fig. 4.13 shows the original RGB color fish image combined with its contour. The original fish image is successfully partitioned from the background image after applying morphology closing and opening, and contour edge detection.



(a) Upview image



(b) Sideview image

Fig. 4.12 Region filling results of the fish image



Fig. 4.13 Original fish image combined with its contour

### 4.3.3 Surface area and volume calculations

The fish surface area and volume can be obtained by measuring the pixels in the upview and sideview of bw images in Fig. 4.12. With the end result of black and white image, image segmentation process with image conversion into several steps is done. This bw image is used to measure the dimension of fish. The size image calibration in millimeter is obtained by measuring the number of pixels from the outermost distance of the fish images as shown in Fig. 4.3. Outermost distances of fish in millimeter are measured by using vernier caliper as shown in Fig. 4.3. One sample of fish has its dimension of 290 mm (L) x 51.1 mm (H) x 38.22 mm (W), and calibration result is obtained as 1 pixel = 0.00557 mm for (H) and 1 pixel = 0.0251 mm for (L), and 1 pixel = 0.00475 mm for (W).

By using the proposed image processing method, the surface area  $S$  and the volume  $V$  of the fish are obtained. The error measurement ( $e_m$ ) is defined as percentage differences between the experimental result of the proposed partition method (PM) and the proposed analytic method (AM). The error measurement is calculated as follows:

$$e_m = \left( \frac{\text{PM} - \text{AM}}{\text{AM}} \right) \cdot 100\% \quad (4.2)$$

Experiment is conducted for four fishes and their results are shown in Table 4.2. Based on the partition method, the surface area for fish 1, 2, 3, and 4 are 174,343.81 mm<sup>2</sup>, 168,702.06 mm<sup>2</sup>, 172,655.05 mm<sup>2</sup>, and 168,458.05 mm<sup>2</sup>, respectively. The volume for fish 1, 2, 3, and 4 are 312,116.23 mm<sup>3</sup>, 286,657.97 mm<sup>3</sup>, 306,497.57 mm<sup>3</sup>, 284,822.04 mm<sup>3</sup>, respectively. From Eq. (2.19) and Eq. (2.22), the surface area and

the volume of an ellipsoid using the analytic method are obtained. The error measurement between the partition method and the analytic method of the surface area for fish 1, 2, 3, and 4 are 6.03%, 5.42%, 5.91%, and 5.31%, respectively. The error measurement between the partition method and the analytic method of the volume for fish 1, 2, 3, and 4 are 5.30%, 4.93%, 5.05%, and 4.81%, respectively. The process of image segmentation, feature extraction, and measurement of fish surface area and volume takes 23 milliseconds in computation time.

Table 4.2 Results of surface area and volume of four fishes

Fishes sample size (mm)				Surface area (mm <sup>2</sup> )		
	L	H	W	Partition method	Analytic method	Error ( $e_m$ ) (%)
1	290	38.22	51.1	174,343.81	164,428.75	6.03
2	287	37.12	49.0	168,702.06	160,028.51	5.42
3	289	38.20	50.5	172,655.05	163,020.54	5.91
4	287	37.00	48.9	168,458.05	159,963.96	5.31
				Volume (mm <sup>3</sup> )		
	L	H	W			
1	290	38.22	51.1	312,116.23	296,406.67	5.30
2	287	37.12	49.0	286,657.97	273,189.71	4.93
3	289	38.20	50.5	306,497.57	291,763.51	5.05
4	287	37.00	48.9	284,822.04	271,750.83	4.81

#### 4.4 Summary

This chapter proposed an image processing methods for fish surface area and volume calculations. The image samples used to validate the proposed method were images of four fishes. The HD camera was used to acquire two images, one from the top view and one from the side view. Measurement of surfaces area and volumes of four fishes could be done by experiment through partition method. Measurements can be done easily, quickly and accurately. Approximation of the fish's surface area and volume were done analytically and by partition method. Experimental results using samples of four fishes showed that the error between analytical method and image partition method in surface area were 5.31%~6.03% and the differences of volume were 4.81%~5.30%.

The difference in error measurement is due to the difference in the size of the actual fish. The gaps among differences in measurement results from the four fish samples were small: 0.72% for surface area and 0.49% for volume between fish 1 and fish 4, respectively. Therefore, the proposed partition method developed was valid. To develop an algorithm for estimating surface area and volume of fish in the future task, it is important also to develop a new image processing method and an image acquisition system.

## **Chapter 5: Real-time Measurement Method for Fish Surface Area and Volume**

The proposed partition method developed in chapter 4 was valid because the difference between image processing and analytical method was small. However, this method was built for offline application. This chapter proposes a real-time measurement method based on 3D coordinate using stereo camera. The measurement system used in this proposed method was explained of Fig. 3.3 in section 3.2. To do this task the followings are done. Firstly, the stereo camera is calibrated to correct its intrinsic parameters and distortion parameters rightly. Secondly, real-time image segmentation is done by combining HSV color space, threshold, mathematical morphological transformation, and contour detection techniques to extract objects in a graph-based image. Thirdly, the object coordinate, surface area and volume of the fish are measured. Finally, the effectiveness of the measurement method in real-time based on 3D coordinate is compared with the analytical method through experimental results.

### **5.1 Camera calibration**

Camera calibration is an important step in 3D computer vision to extract metric information from 2D images. Focal length is the important parameter in a measurement algorithm using stereo camera. This parameter is obtained through the stereo camera calibration. This parameter determines the strength or weakness of a camera lens to focus on the object by distorted images. There are four intrinsic parameters:  $f_x$  and  $f_y$  as the focal lengths of the camera in terms of pixel

dimensions in the  $x$  and  $y$  direction, and  $(u_0, v_0)$  is the principal point. The camera usually represents lens distortion that is a radial distortion given by

$$\mathbf{u}_d = \begin{cases} u_d = (u_u - u_0)(1 + k_1 r_u^2 + k_1 r_u^4) \\ v_d = (v_u - v_0)(1 + k_1 r_u^2 + k_1 r_u^4) \end{cases} \quad (5.1)$$

where  $p(u_u, v_u)$  and  $p(u_d, v_d)$  are distortion-free and distortion-normalized image coordinates, respectively.  $k_1$  and  $k_2$  are the radial distortion coefficients, and  $r_u^2 = u_u^2 + v_u^2$  [59,60]. According to the camera model, focal length is given by

$$f = \frac{1}{2}(f_x / m_x + f_y / m_y) \quad (5.2)$$

where  $f_x$  and  $f_y$  are defined as the focal length of the camera in terms of pixels dimensions in the  $x$  and  $y$  direction, respectively.

The important task of the camera calibration is to determine the four intrinsic parameters and the two distortion coefficients.

The camera calibration follows the procedure proposed in [61]. The recommended calibration procedure as follows:

1. Setup camera, print a pattern and attach it to a planar surface.
2. Take a few images of the model plane under different orientations by moving either the plane or the camera.
3. Detect the feature points in the images.
4. Estimate the intrinsic and extrinsic parameters of the camera.

The camera system used in this dissertation is a single-head stereo camera put on the table as shown in Fig. 5.1(a). The camera is

connected to personal computer using USB cable. The personal computer is used to process acquired images. The frames obtained from the camera system are captured and stored on the computer system using open source computer vision (OpenCV C++) [62]. The calibration object used in the computation is a planar checkerboard pattern. The checkerboard pattern is obtained by a laser printer paper. The use of the checkerboard pattern allows sub-pixel corner detection of checkerboard corners. The calibration pattern is shown in Figure 5.1(b). Each square box over the calibration pattern has dimensions  $25\text{mm} \times 25\text{mm}$ . Fig. 5.2 shows a set of pairs of close-up RGB images of the checkerboard placed in different positions and orientations. The RGB images are corrected by taking a variety of focus images that can cover the entire picture.



Fig. 5.1 Camera calibration setup (a), and image pattern for calibrating intrinsic parameter (b)

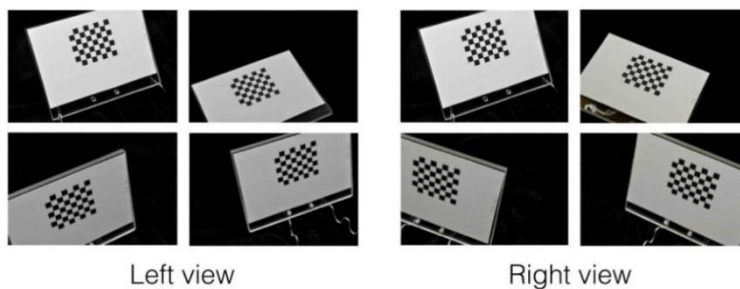


Fig. 5.2 Set of pairs of close-up RGB images of the checkerboard

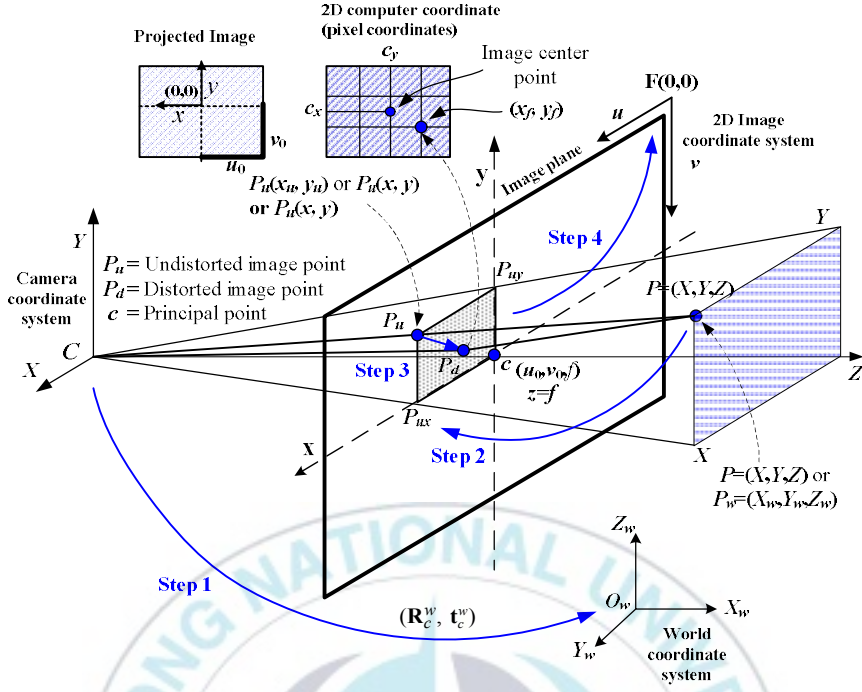


Fig. 5.3 Steps of camera calibration.

There are four steps to convert a point from world coordinate to the computer memory image coordinate [61]:

**Step 1** (Transformation from world to camera): Transformation from a point Let  $P_w=(X_w, Y_w, Z_w)$  in 3D world space to the point  $P=(X, Y, Z)$  in the 3D camera frame using homogeneous transformation is represented as follows:

$$\mathbf{x} = \begin{bmatrix} x_k \\ y_k \\ z_k \end{bmatrix} = \begin{bmatrix} r_1 & r_2 & r_3 \\ r_4 & r_5 & r_6 \\ r_7 & r_8 & r_9 \end{bmatrix} \begin{bmatrix} x_w \\ y_w \\ z_w \end{bmatrix} + \begin{bmatrix} t_x \\ t_y \\ t_z \end{bmatrix} = \mathbf{R}\mathbf{x}_w + \mathbf{t} \quad (5.3)$$

where  $\mathbf{R}$  is 3x3 rotation matrix, and  $\mathbf{t}$  is the 3x1 translation vector.

**Step 2 (Projection):** Transformation from 3D coordinate to the undistortion image coordinate  $(x_u, y_u)$  using perspective projection of pinhole camera geometry and focal length  $f$  is represented as

$$\mathbf{x}_u = \begin{bmatrix} x_u \\ y_u \end{bmatrix} = \begin{bmatrix} f \frac{X}{Z} \\ f \frac{Y}{Z} \end{bmatrix} \quad (5.4)$$

where  $(x_u, y_u)$  is undistorted image point

**Step 3 (Lens distortion):** Transformation from undistorted image coordinate to distorted coordinate  $(x_d, y_d)$  with distorted function  $f_d$  and lens distortion coefficients  $k_i$ , for  $i=1\sim3$ , is represented as

$$\mathbf{x}_d = \begin{bmatrix} x_d \\ y_d \end{bmatrix} = f_d \mathbf{x}_u = \left(1 + k_1 r^2 + k_2 r^4 + k_3 r^6\right) \mathbf{x}_u \quad (5.5)$$

where  $r^2 = \sqrt{x_u^2 + y_u^2}$  [58, 60].

There are two kinds of distortions: radial and tangential. However only radial distortion  $k_i$  is to be considered as shown in Eq. (5.5).

**Step 4 (Camera to image):** Transformation from distorted image coordinate to computer image coordinate  $(x_f, y_f)$  is presented as

$$\mathbf{x}_f = \begin{bmatrix} x_f \\ y_f \end{bmatrix} = \begin{bmatrix} f_x & 0 \\ 0 & f_y \end{bmatrix} \mathbf{x}_d + \begin{bmatrix} c_x \\ c_y \end{bmatrix} \quad (5.6)$$

$$f_x = s_x d_x'^{-1}, f_y = d_y^{-1}, d_x' = d_x \frac{N_{cx}}{N_{fx}} \quad (5.7)$$

where  $s_x$  is an uncertainty scale factor,  $d_x$  is the center to center distance between adjacent sensor elements in  $X$  direction,  $d_y$  is the center to center distance between adjacent sensor elements in  $Y$  direction,  $N_{cx}$  is number of sensor elements in  $X$  direction, and  $N_{fx}$  is number of pixels in one scan line of the image captured by computer.

### 5.1.1 Calibration intrinsic parameter of camera

Camera intrinsic parameters are calibrated at working distance about 1000 mm. Chessboard image is used as calibration pattern, and 19" LCD monitor is used to display image pattern. Fig. 5.4 shows an image pattern for calibrating intrinsic parameters. Table 5.1 shows the calibration results of the left camera and right camera, respectively.

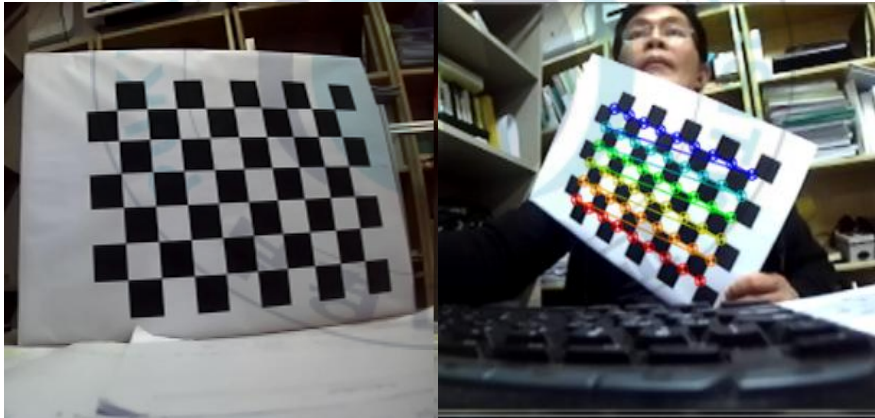


Fig. 5.4 Image pattern for calibrating intrinsic parameter.

Table 5.1 Calibration results of the intrinsic camera parameter.

Camera	Focal length (pixel)		Principal point (pixel)		
	$f_x$	$f_y$	$u_0$	$v_0$	
Left	940.49	769.00	674.65	180.35	
Right	941.49	769.50	675.65	181.25	
Camera	Distortion coefficients		pixel/mm		Focal length (mm)
	$k_1$	$k_2$	$P_{ux}$	$P_{uy}$	
Left	-98.91	11.34	674	180	2.8289
Right	-99.01	11.84	675	181	2.8311

## 5.2 Real-time image segmentation method for fish surface area and volume measurement

### 5.2.1 Related work

Image segmentation and stereo camera plays an important role in application of video processing such as object detection and recognition. To recognize an object, firstly, the image must be segmented into the object background and the object to be recognized. Because the results of image segmentation are often not very appropriate for some visual tasks, the shape and appearance of the area change significantly for landscape images obtained from different viewpoints or different lighting conditions. Therefore, matching a segmented region in such an image is indispensable. There are a lot of

researches in relation to image segmentation and object handling task with camera as a vision system. Implementation of real-time vision for tracking task and robot guidance has been introduced [63]. This method was a basic theoretical approach and simply described a typical architecture of 3D scene reconstruction. S. Helmer et al. [64] proposed object recognition using stereo camera, where a model utilized a chamfer-type silhouette classifier. However, it was easy to lose stereo depth information. A method using segmentation-based stereo camera for 3D object recognition was proposed [65]. In this work, segmentation-based stereo camera was employed for 3D sensing, and matched with computer-aided design (CAD). This method is not suitable for real-time processing due to the computational complexity to combine between pre-processing with CAD matching.

The quality of the segmented image always depends on color, distance, plan information, and light. Nevertheless, the user did not stop finding the way to get good image segmentation methods. A method for image segmentation using mathematical morphology was proposed [66]. This method used approach based on the watershed transformation. However, this method was applied to the static image. An image segmentation algorithm based on threshold segmentation was proposed [67]. In this work, the segmentation algorithm assumed that each pixel in the image has its own threshold. However, this method was applied to the offline method, and threshold-based segmentation is difficult to be performed if the object has low contrast with its background. Automatic threshold selection for image segmentation based on genetic algorithm was proposed [68]. This paper focused on the issue of automatic selection for multi-level

threshold for image segmentation. However, this method in implementation was applied to the offline method.

Image segmentation is done before estimating the actual features of object recognition. The main problems of an image captured by the video camera results in excessive information, complex disparities, the significant change of the shape and appearance of regions. Therefore, a method to extract the foreground object image is needed. A real-time image segmentation method must be proposed to solve this problem.

### **5.2.2 Proposed real-time image segmentation method**

In this section, an image segmentation method in real-time is proposed. The segmentation process is done in real-time on the video frame by using stereo camera. To reduce complexity and computation time, hue and value feature spaces are segmented separately before they are combined. Stereo camera is applied to capture the images of the fish. In this work, a contour based segmentation and mathematical morphological method are used for real-time segmentation. Image segmentation is done by combining HSV color space, threshold, mathematical morphological transformation, and contour detection techniques to extract objects in a graph-based image. Software design is implemented by using C++ programming language. For implementing a real-time image segmentation, a library available in open source computer vision (OpenCV, C++) is used. Library functions are used for loading image, creating windows to hold an image in real-time, and saving image. Algorithm 2 explains the real-time image segmentation used for fish surface area and volume calculations.

<b>Algorithm 2.</b> Algorithm to perform real-time image segmentation used for fish surface area and volume calculations	
1.	Creates window user interface on OpenCV image processing tool to adjust the value of parameters in real-time.
2.	Get the centroid of the object by creating a two dimensional OpenCV image processing tool point as follows: $pt = cvPoint(x, y) \quad (5.8)$ (Obtaining XY coordinates from (x,y) from CvPoint)
3.	Segment color images using features color of images extracted from the HSV space. To convert from RGB to HSV use standard transformation Eqs. (2.40)~(2.42), (assuming normalized RGB values) first find the maximum and minimum values from the RGB triplet.
4.	Set a saturation level. Based on human vision perception, the intensity domination is at saturation level $th_{sat}$ below 0.2. Color is defined as black at $th_{sat}(v)=1$ for white=0. $v=value(V)$ $th_{sat}(v) = 1 - \frac{0.8 \cdot v}{255} \quad (5.9)$ The saturation $S$ is defined as $S_i = \begin{cases} (G \max - G \min) / G \max, & \text{for } G \max \neq 0 \\ 0, & \text{otherwise} \end{cases} \quad (5.10)$ If saturation $S$ is 0 (zero), hue is undefined (i.e. the color has no hue, therefore, it is monochrome)
5.	Create a structuring element. The structuring element B is a $3 \times 3$ square, that is, $B = \{(-1,-1), (-1,0), (-1,1), (0,-1), (0,0), (0,1), (1,-1), (1,0), (1,1)\}$ .
6.	Select the centroid based on its magnitude. The centroid is calculated as follows: $x_c = \frac{\sum_{x=1}^N \sum_{y=1}^N x \times g(x, y)}{\sum_{x=1}^N \sum_{y=1}^N g(x, y)}; \quad y_c = \frac{\sum_{x=1}^N \sum_{y=1}^N y \times g(x, y)}{\sum_{x=1}^N \sum_{y=1}^N g(x, y)} \quad (5.11)$

	where $x_c$ and $y_c$ are the centroid of a fish, $N$ is the image length in the pixel, and $g(x, y)$ is grey level.
7.	Apply boundary region by erosion and dilation.
8.	Repeat step 3 to 6 until a point $(x, y)$ converge to object image centroid.
9.	Output a binary image.

### 5.2.2.1 Scene setup

Scene settings play an important role in real-time image segmentation. Scene settings must be explained in advance to evaluate the functionality of the algorithm and its components. Four different objects are tested before being done on fish objects to test the ability of the proposed real-time image segmentation method as follows:

1. Different simple objects to test and demonstrate the basic functionality.
2. Different size of the objects to test the upper and lower bounds of objects which can be detected.
3. An object with different shapes like sharp-edged, elongated and hairy objects to test the limits of the fixation-based approach.
4. Textured objects to test the ability to handle multi-colored objects.

### 5.2.3 Experimental results of real-time image segmentation

The proposed segmentation method is designed to detect the fish object useful for fish processing. The proposed image segmentation method is applied to different scanning objects before it is applied to the fish. The various common objects such as a simple object, small

and large objects, objects of different shapes, and various objects are used in this experiment.

### 5.2.3.1 Real-time image segmentation results of various common objects

The segmentation of simple objects is the basis for testing the capability of the algorithm. If it fails at this stage, it will probably also fail for more complex objects. The simple object, in this case, is defined as objects with constant color. Their shape is convex without having sharp edges. A segmentation of simple objects can be shown in Fig. 5.5. Two simple objects with different sizes are all segmented very well. The location of the contours is optimal. On the other hand, the quality of the disparity map gets worse for relatively small objects as there is less depth information available. Only the contour on the cup shifts slightly from the edge of the object because the color difference between the object and background is almost the same.



Fig. 5.5 Segmentation of simple objects

The size of an object can affect the segmentation process. Therefore, two different sizes in the scene are evaluated. The scene contains the small size object and the large size object. Fig. 5.6 shows

the result of the segmentation of the small object and the large object. The results of the segmentations produce for both the large object and the small object are very good. Especially, the segmentation of very small objects outperforms the expectations.

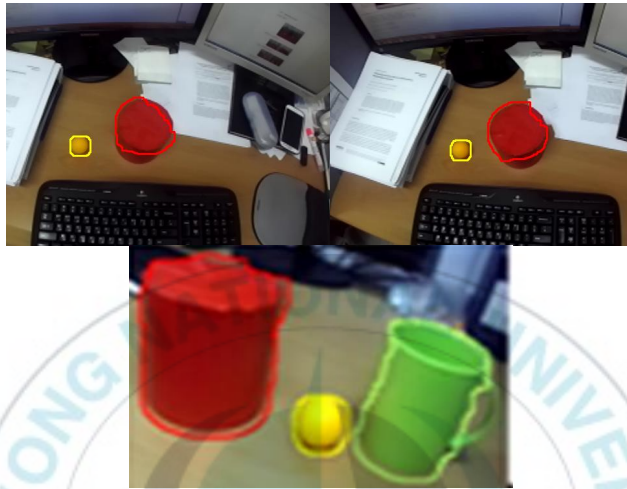


Fig. 5.6 Segmentation of the small object and the large object

The shape of the object influences the segmentation process and can also have an impact on the results of segmentation. Fig. 5.7 shows the segmentation results of several objects with different shape of objects. The shape includes objects with sharp-edge, elongated object, and thin object. The experimental results in the segmentation of the edge detection for the large size are more difficult than those for the small size. When the large size objects are transformed to log-polar space, the displayed objects in the scene are deformed to long horizontal objects as they are bent around the fixation point. Fixation points are the view focuses on various salient locations. However, the graph cut algorithm tries to find a short vertical cut to minimize energy [69]. Therefore, long objects and objects with sharp edges tend to get

cut off. The graph cut algorithm suffers from the same problem, but it can counteract this behavior by using the color information.

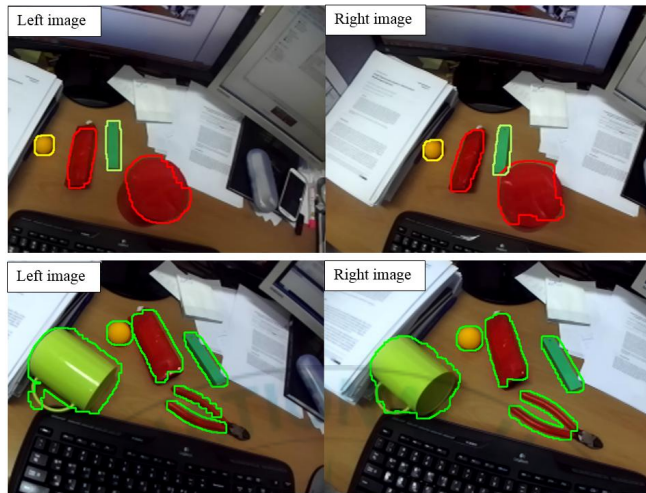


Fig. 5.7 Segmentation of the different shapes of objects

### 5.2.3.2 Real-time image segmentation results for fish object

This section describes the real-time segmentation process of the fish object. The surface structure of fish skin is categorized as a textured object. Object segmentation becomes a problem when the object surfaces have complex texture patterns and generate many local edges within the same region [70]. Textured objects are the most difficult objects to segment, where the computation of the texture gradient is neglected to increase the performance of the edge detection. The textured gradient is compensated by the large kernel filter in the edge detection and the color models in the graph cut algorithm.

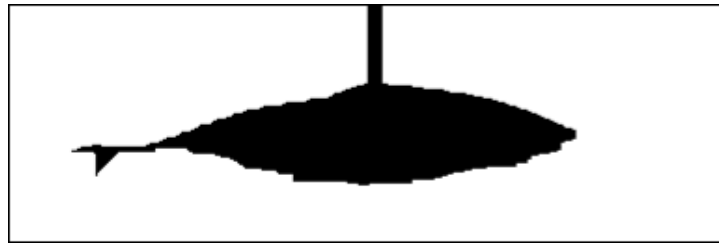
In the segmentation process, if a segmentation result has low accuracy, the segmentation is considered as a failure. For segmentation of fish objects in real time, several trials were carried out to obtain

satisfactory results. Fig. 5.8 shows the thresholded image that needed to be inverted from black color to white color after segmentation. As shown in Fig. 5.8(a), in this image segmentation process, the thresholded image is overlaid. The failure in segmentation causes failure in fish detection as shown in Fig. 5.8(b). In this trial, the segmentation of the fish object is done by choosing a high threshold ( $Th=255$ ). Fig. 5.9 shows the image segmentation result of the fish object by choosing a medium threshold ( $Th=126$ ). Fig. 5.9(a) shows that an image is not be segmented properly or an image get the wrong polarity after segmentation. The improper segmentation also causes failure in fish contour detection as shown in Fig. 5.9(b). Another case is needed to overcome this obstacle: i.e., image segmentation using the bounding box [71].

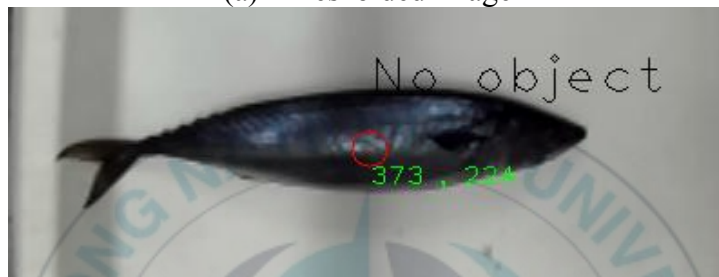
Fig. 5.10 shows the segmentation results of the fish object with the lowest threshold ( $Th = 0$ ) and the bounding box. Fig. 5.10(a) shows that the best result is gained in this trial. Since it has high accuracy, the feature segmentation results obtained in this trial will be used on the next step. Next trial is using feature segmentation results obtained in Fig. 5.10. By applying a graph cut algorithm, the results in Fig. 5.11 are obtained. Finally, image segmentation in the bw image of the object is obtained as shown in Fig. 5.11(a).

The segmentation results of the proposed method were compared with the segmentation methods in [8] and [9] as shown in Fig. 5.12. Fig. 5.12(c) showed that the proposed method obtains good segmentation result compared to the method by the watershed method and the method by the threshold value of Fig. 5.12(a) and Fig. 5.12(b).

As can be seen in Fig. 5.12(a) and Fig. 5.12(b), the results of segmentation are not perfectly segmented.



(a) Thresholded image



(b) Original RGB color image

Fig. 5.8 Segmentation of the fish object with  $Th = 255$



(a) Thresholded image

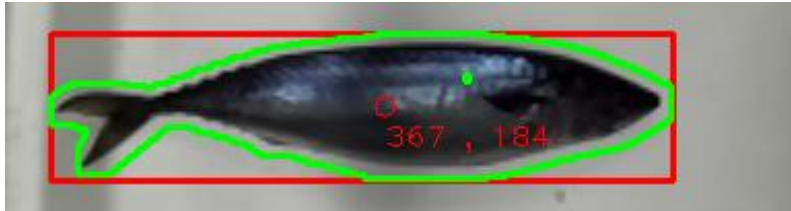


(b) Original RGB color image

Fig. 5.9 Segmentation of the fish object with  $Th = 126$



(a) Thresholded image



(b) Original RGB color image

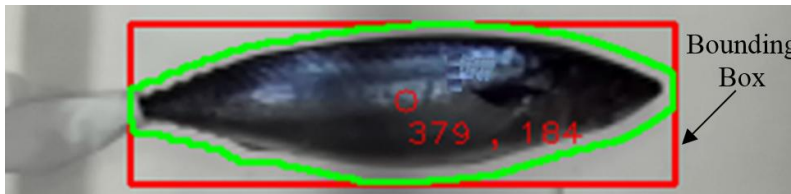
Fig. 5.10 Segmentation of the fish object with  $Th = 0$  and bounding box



(a) Thresholded image

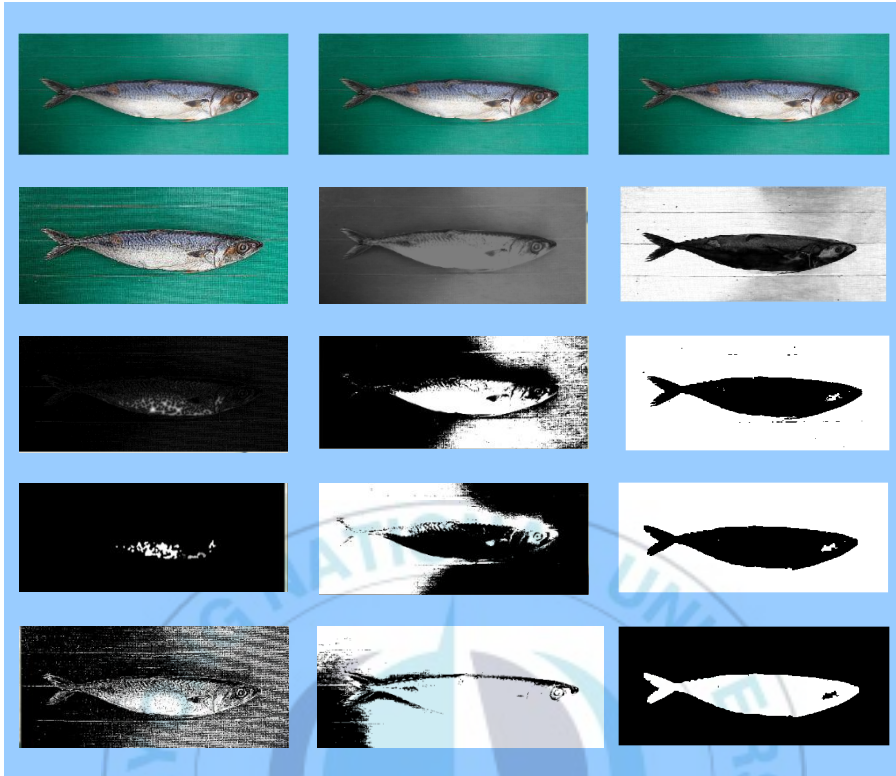


(b) Original RGB color image with the contour image



(c) Original RGB color image with the contour and the bounding box

Fig. 5.11 Segmentation of the fish object with  $Th = 0$ , bounding box, and graph cut



(a) Result for watershed transformation      (b) Result by threshold value      (c) Segmentation result by proposed method

Fig. 5.12 Image segmentation results by watershed transformation, threshold value, and the proposed method

### 5.3 3D coordinate measurement using stereo camera

This section proposes 3D coordinate measurement using stereo camera. Obtaining exact position of an object before measuring the object is needed for handling the object. Using stereo camera to determine the object position is very important for measuring the 3D coordinate. A method for recognizing an object of feature descriptor for being texture-less was proposed [72]. This method performed an initial dense descriptor computation to capture 2D and 3D gradient image information and combined the point-based information into

local histograms. However, the image histogram was not suitable for real image segmentation

### 5.3.1 3D Measurement principle

The 3D position is obtained from stereo triangulation. Firstly, two images are acquired from a set of 3D test points whose 3D coordinate are known. Secondly, the estimated 3D coordinate of the same points are computed from their projections using the calibrated parameters. Finally, the discrepancy between real and estimated positions is compared. In this case, the accuracy depends on the calibration of both cameras. Fig. 5.13 shows the 3D measurement principle using stereo camera. The projective transformation for the baseline stereo camera images are searched with the epipolar constraints that the epipolar lines are horizontal, and the 3D measurement is carried out from the information of corresponding points. The pairs of baseline stereo images are generated from the ordinary images with the projective transformation about the axes of X, Y, and Z.

The triangulation of stereo camera model is shown in Fig. 5.14. Generally, stereo systems may have optical axes with the fixation point at a finite distance from the cameras. The left and right image planes are represented by the segments  $I_{left}$  and  $I_{right}$ , respectively, and  $O_l$  and  $O_r$  are the centers of projection, or optical centers in the left and right of the camera, respectively. Because the optical axes are parallel, their point of centroid called the fixation point lies intimately far from the cameras.

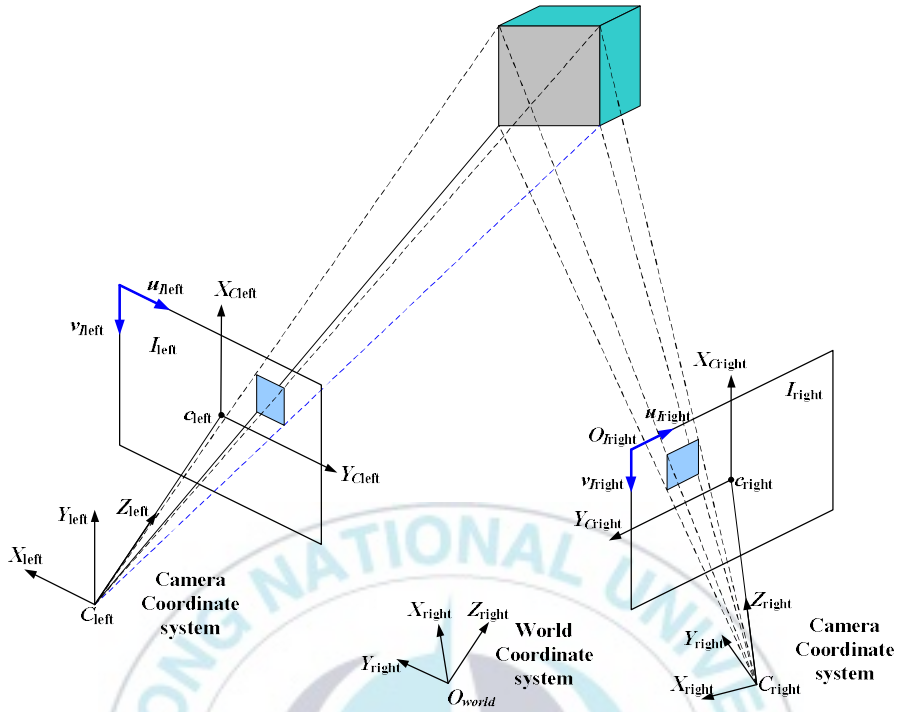


Fig. 5.13 3D measurement principle using stereo camera

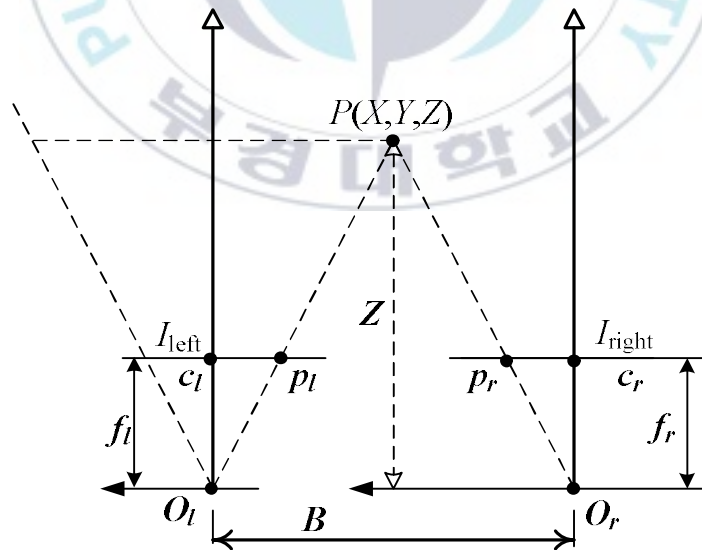


Fig. 5.14 Triangulation of stereo camera model

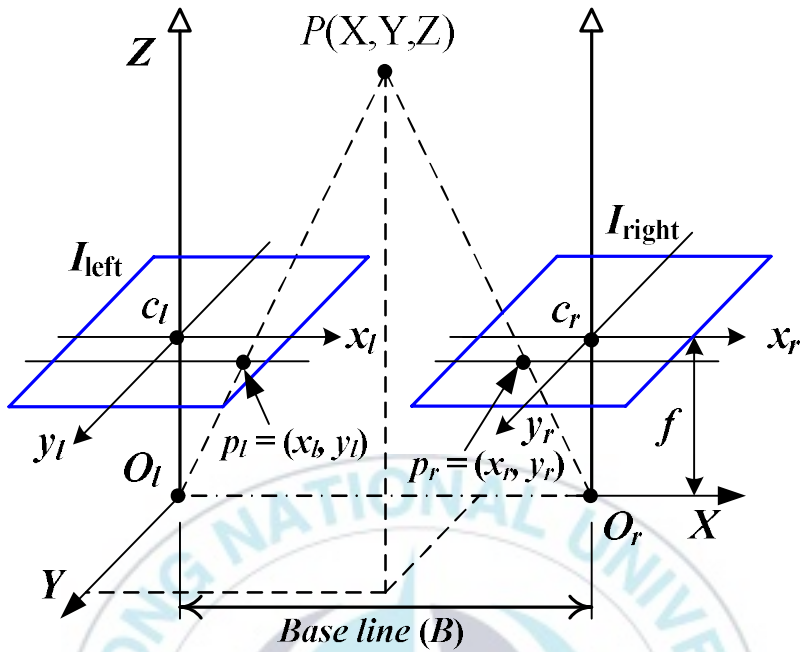


Fig. 5.15 Reconstruction of the 3D stereo position

Reconstruction the 3D stereo position is shown in Fig. 5.15. Triangulation of the stereo system reconstructs the 3D position of each single observed point  $P(X, Y, Z)$  in the camera coordinate frame from its projections  $p_l$  and  $p_r$  on the left and right ideal image coordinate frames using the known distance  $B$  between the center of projection  $O_l$  and  $O_r$  and the common focal length  $f$  of the cameras. The distance  $L$  is called as a baseline of the stereo system. Let  $(x_l, y_l)$  and  $(x_r, y_r)$  be the 2D coordinate of the image points  $p_l$  and  $p_r$  with respect to the principal points as traces of the optical axes  $c_l$  and  $c_r$  as the origins of  $x, y$ -image coordinate, and the  $x$ -axis is parallel to the baseline. The 3D  $X, Y, Z$ -coordinate frame has the distance  $Z$ -axis parallel to the optical axes, the  $X$ -axis parallel to the baseline and the image  $(x_l, x_r)$ -axes, and the  $Y$ -axis parallel to the image  $(y_l, y_r)$ -axes. By assuming that the 3D

coordinate frame has the origin in the optical center of the left camera, the perspective projection from the 3D camera coordinate  $(X, Y, Z)$  to the ideal image coordinate  $(x, y)$  as follows:

$$x_l = \frac{X \cdot f}{Z}; x_r = \frac{(X - B) \cdot f}{Z} - B; y_l = y_r = \frac{Y \cdot f}{Z} \quad (5.12)$$

From Eq. (5.12), the  $Z$  coordinate can be determined as follows:

$$Z = f \cdot \frac{B}{B - d} \quad (5.13)$$

where  $x_l = p_l - c_l$ ,  $x_r = p_r - c_r$ , and  $d = x_r - x_l$  is a disparity that is the difference in image position between corresponding points in the two images. Once  $Z$  is determined, it is straightforward to calculate  $X$  and  $Y$  using similar triangles:

$$X = x_l \cdot \frac{B}{B - d} \quad (5.14)$$

$$Y = y_l \cdot \frac{B}{B - d} \quad (5.15)$$

Determination of 3D object coordinate is implemented after segmentation process. Firstly, the object is recognized to determine the center of the object, then the principle of determining the 3D coordinate is implemented. Distance error rate  $e_d$  is calculated as

$$e_d = \left( \frac{Z - \text{real distance}}{\text{real distance}} \right) \cdot 100\% \quad (5.16)$$

### 5.3.2 Distance measurement of an object between stereo camera

Fig. 5.16 shows the relationship between the object size in bounding box (pixels) and the distance which can be used to estimate the width and height of the object in millimeters. The acquisition of two stereo camera images showing the same object from different and known point of views allows the analytic estimate of the target relative distance, relative position and absolute diameter.

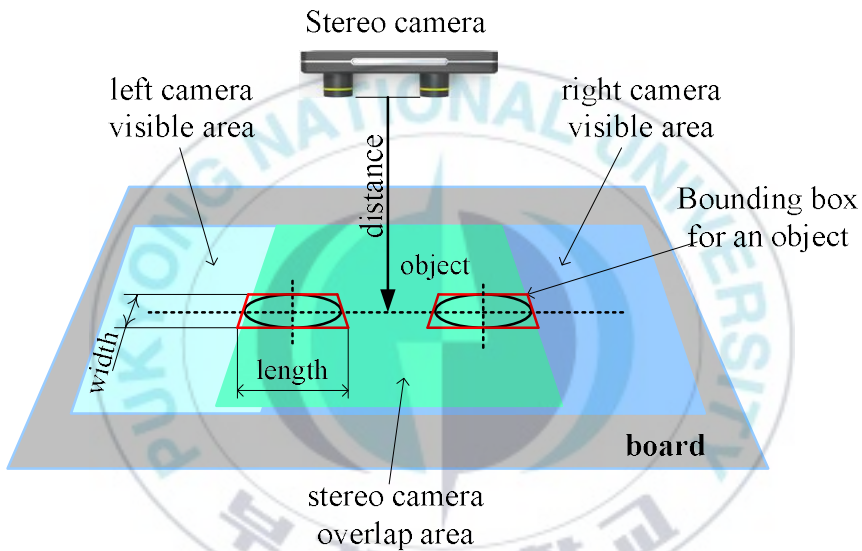


Fig. 5.16 Object size in function of the distance between the stereo camera and the object

Fig. 5.17 shows a schematic representation of a distance estimated with a stereo camera.  $B$  is the distance between two cameras,  $\beta_1$  is half of the horizontal angle field of view of the left camera, and  $\alpha_1$  is half of the vertical angle field of view of the left camera.  $\beta_2$  is half of the horizontal angle field of view of the right camera, and  $\alpha_2$  is half of the vertical angle field of view of the right camera. From Fig. 5.17, by

doing analytical computation for the angles of  $\varphi_1$ ,  $\varphi_2$  and  $\varphi_3$ , the distance to a pixel located in the column  $x_1$  of the left image and  $x_2$  of the right image as shown in Fig. 5.19 can be estimated.

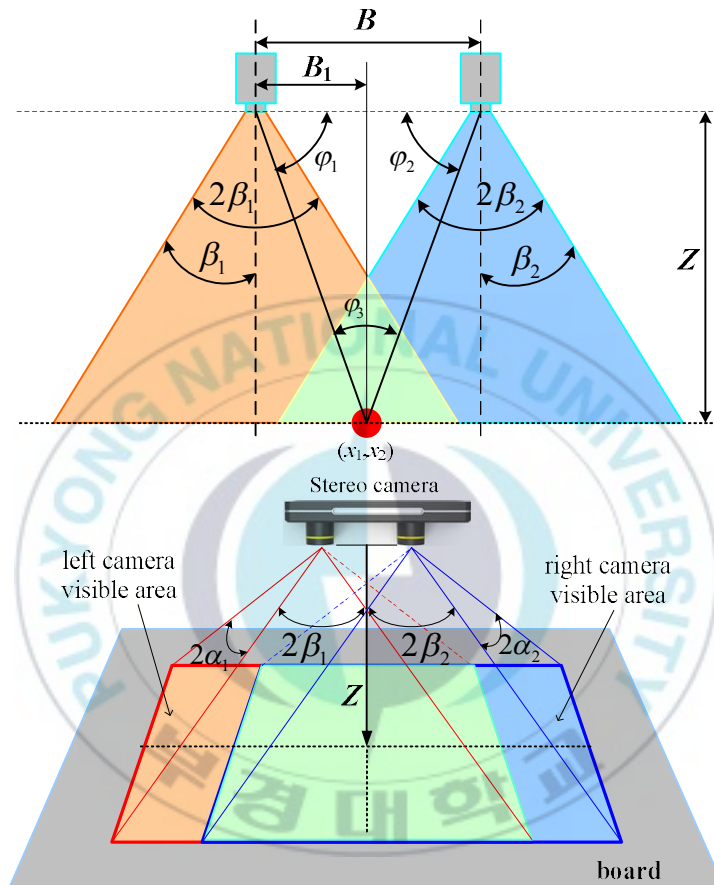


Fig. 5.17 Schematic representation of a distance estimate with a stereo camera.

The half angle of view of a camera is given by  $\beta_1 = \tan^{-1}(D/2f)$ .  $D$  is the diameter of the camera's field stop and  $f$  is the focal length of the camera as shown in Fig. 5.18.

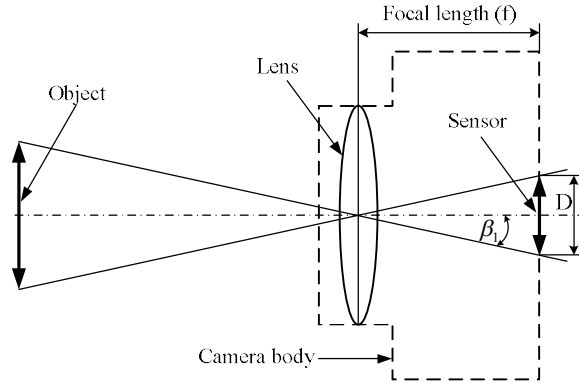


Fig. 5.18 Angular aperture of a camera

From Fig. 5.17, by doing geometry principle, distance Z can be obtained as follows:

For left camera

$$\tan \varphi_1 = \frac{Z}{B_1} \quad (5.17)$$

$$Z = B_1 \cdot \tan \varphi_1 \quad (5.18)$$

For right camera

$$\tan \varphi_2 = \frac{Z}{B - B_1} \quad (5.19)$$

Substituting Z in Eq. (5.19) for Eq. (5.18) yields:

$$\tan \varphi_2 = \frac{B_1 \cdot \tan \varphi_1}{B - B_1} \quad (5.20)$$

Solving Eq. (5.20) for  $B_1$ , the equation become as follows:

$$B_1 = \frac{B \cdot \tan \varphi_2}{\tan \varphi_1 + \tan \varphi_2} \quad (5.21)$$

By substituting back Eq. (5.21) for Eq. (5.18), the distance  $Z$  between stereo camera and an object can be obtained as follows:

$$Z = \frac{(\tan \varphi_1 \cdot \tan \varphi_2) \cdot B}{\tan \varphi_1 + \tan \varphi_2} \quad (5.22)$$

The scale of the pixels in the image ( $xScale$ ,  $yScale$ ) is determined as follows:

$$xScale = \frac{2Z \cdot \tan \frac{\beta}{2}}{cols}, \quad yScale = \frac{2Z \cdot \tan \frac{\alpha}{2}}{rows} \quad (5.23)$$

where  $\beta$  and  $\alpha$  are stereo camera field of view,  $Z$  is the distance between stereo camera and object, and  $rows$  and  $cols$  are image size ( $rows$ ,  $cols$ ).

The relative positions of a pixel ( $x,y$ ) as follows:

$$x = \left( x_1 - \frac{cols}{2} \right) \cdot xScale, \quad y = \left( y_1 - \frac{rows}{2} \right) \cdot yScale \quad (5.24)$$

where ( $x_1, y_1$ ) is the relative location of the pixel in one image of the stereo camera.

The real target fish length  $L$  expressed in millimeters can be calculated from the apparent length  $L'$  in pixels obtained from the left image of the stereo camera as follows:

$$L = \sqrt{(L' \cdot \cos \omega \cdot xScale)^2 + (L' \cdot \sin \omega \cdot yScale)^2} \quad (5.25)$$

where  $\omega$  is angle between the  $x$ -axis and the *major axis* of the ellipse that has the same second-moments as the region.

The regionprops are used to measure the properties of image regions. This property is supported only for 2-D input label matrices. Fig. 5.19 illustrates the axes and orientation of the ellipse. The left side of the figure shows an image region and its corresponding ellipse. The Fig. 5.19(a) shows the same ellipse with features indicated graphically; the solid blue lines are the axes, the red dots are the foci, and the orientation is the angle between the horizontal dotted line and the major axis as shown in Fig. 5.19(b).

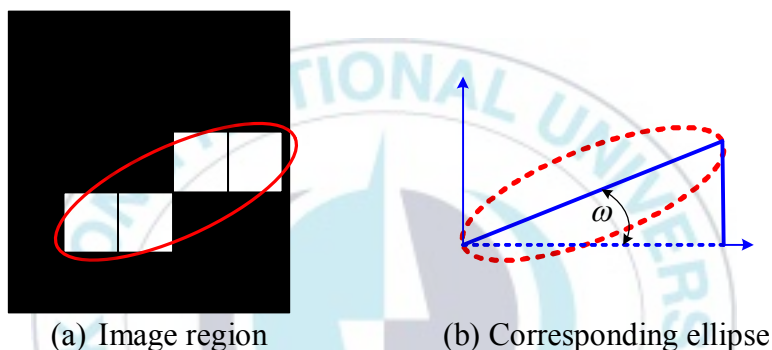


Fig. 5.19 Axes and orientation of the ellipse

Fig. 5.20 shows the flow chart to determine the 3D coordinate for fish surface area and volume measurement. The goal to determine the 3D coordinate is to measure the absolute XYZ coordinate. As mention in section 1.1 above, image geometry must be in the correct position used as an object to calculate fish surface area and fish volume. The correct image geometry is adjusted by stereo camera coordinate measurement. Therefore, this section proposes the stereo camera measuring method to determine the absolute XYZ coordinate of the object. Determination of the absolute XYZ coordinate is done after the image coordinate calibration.

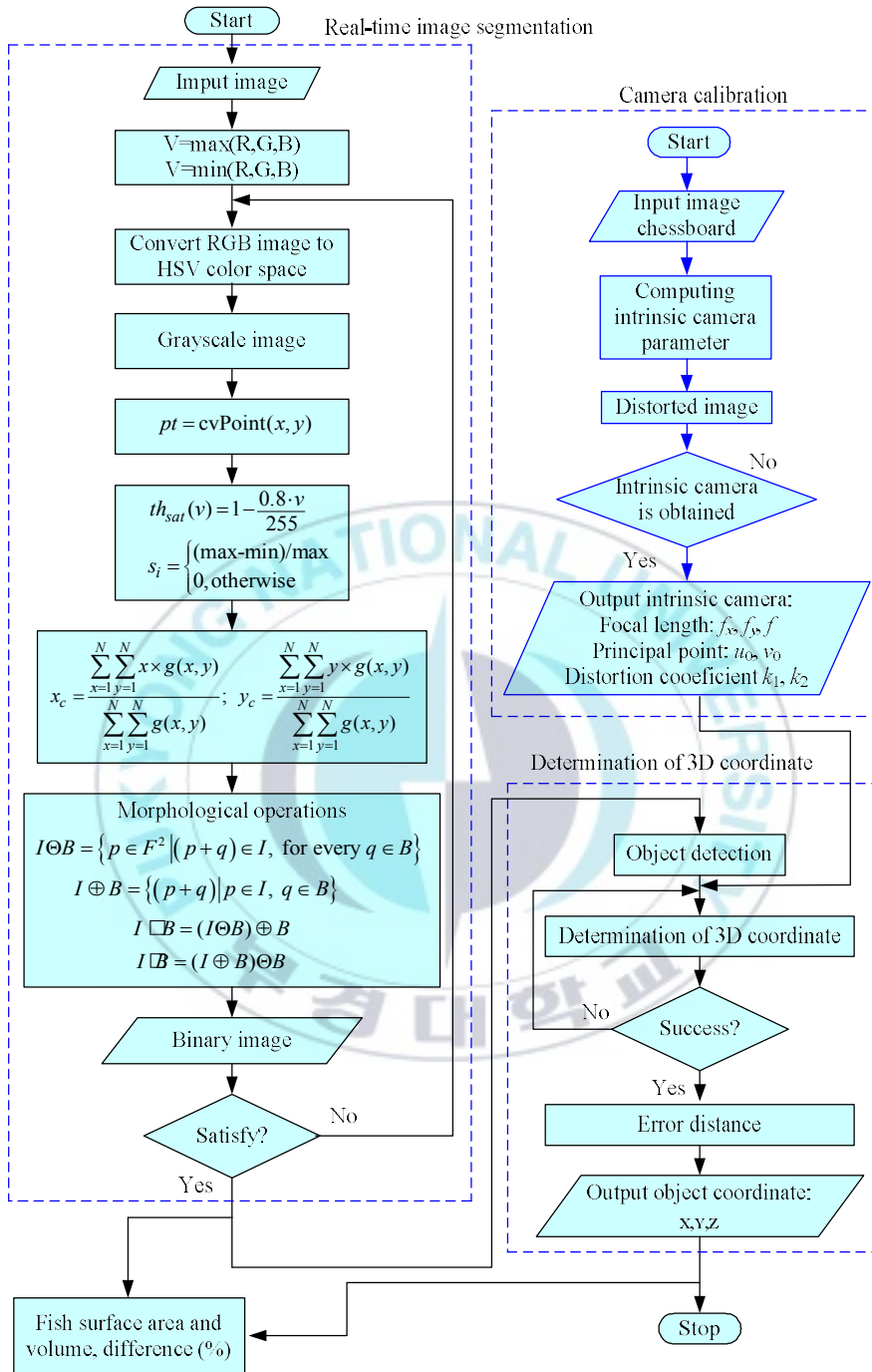


Fig. 5.20 Flowchart to determine the 3D coordinate.

### 5.3.3 System setup

This section describes system setup used to determine the XYZ coordinate. The system setup consists of the image acquisition system of stereo camera used to estimate fish location, and the vision targets used in the experiments.

#### 5.3.3.1 Stereo camera image acquisition system

Fig. 4.21 shows the experimental setup used in this proposed method. The image acquisition device used in this work is ZED stereo camera as a stereo camera. Fig. 4.21(a) shows the prototype of ZED stereo camera to determine 3D coordinate. Fig. 4.21(b) shows the experimental setup of the target measurement. The cross-line is used as a reference to place the target fish at the exact position manually, and its position can be detected automatically.

The purpose of this experimental setup is to estimate the accuracy of a ZED stereo camera in the case of detecting the fish target. The experiment is conducted with a fixed camera, and distances from the camera to the desired object are 780 mm, 660 mm, and 550 mm, respectively. The measurement are conducted three times. This experiment is implemented with a middle-resolution camera and long distance camera, and the image is taken without the special light on its surrounding to check whether the proposed algorithm and the accuracy of measurement can be employed.

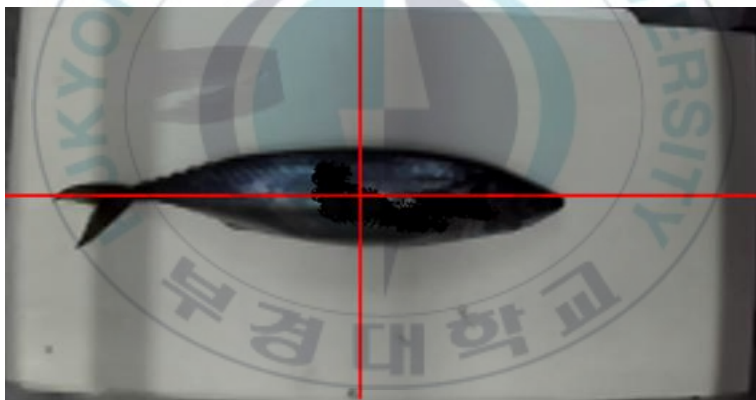
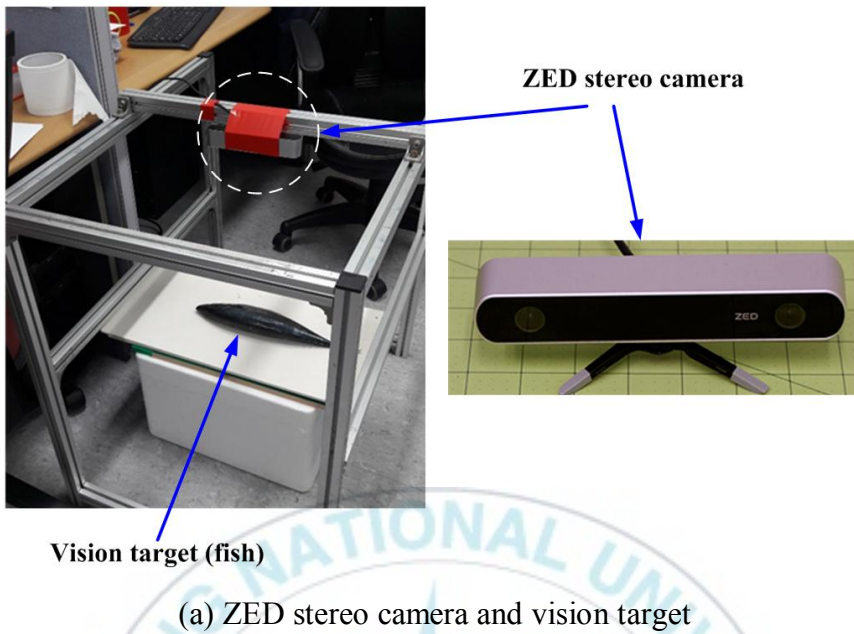
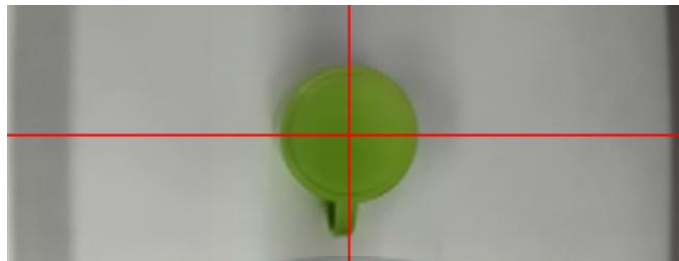


Fig. 5.21 Experimental setup of the stereo camera image acquisition system

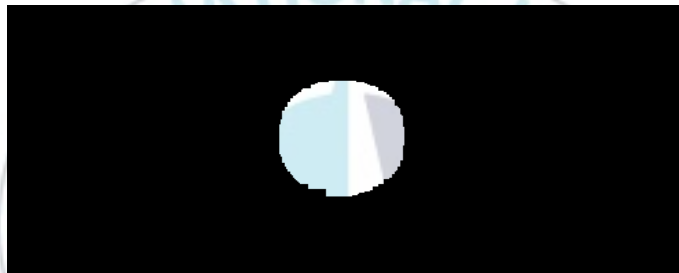
### 5.3.3.2 Vision target detection

As mentioned in section 4.2.3.1, a simple object is the basis for testing the capability of the real-time image segmentation algorithm.

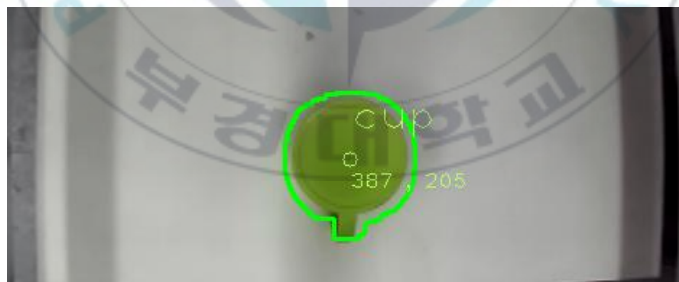
If it fails at this stage, it will probably also fail for more complex objects. The simple object, in this case, is defined as objects with constant color. In this experiment, a cup is used as a reference object as shown in Fig. 5.22 (a).



(a) Cup used as a reference object



(b) Cup thresholded image



(c). Cup segmented image with centroid and centroid position

Fig. 5.22 Cup target detection.

The vision targets tested in the experiments are fish as a real detected vision object. Fig. 5.23 shows fish target detection. Detected target settings are the original RGB color image in Fig. 5.23(a),

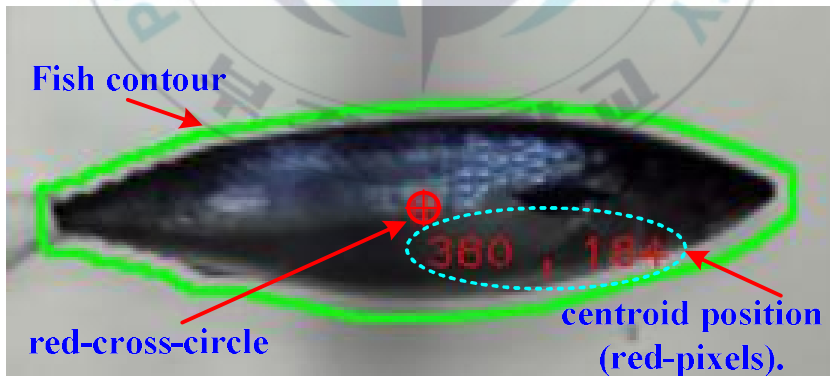
threshold image Fig. 5.23(b), and segmented image with centroid position in Fig. 5.23(c).



(a) Original RGB color image



(b) Thresholded image



(c) Segmented image with centroid (red-cross-circle) and centroid position in (red-pixels)

Fig. 5.23 Fish target detection

The image processing stage involves image segmentation for the fish object target, the object centroid, and bounding box in pixels. The white background used in the experimental setup simplifies the procedure of detecting the background in both RGB color images obtained with the stereo camera.

### **5.3.3.3 Fish surface area and volume measurement**

The software design is developed in C++ using the Qt framework and the open source computer vision library (OpenCV). Fig. 4.24 shows the flow chart of the software developed to calculate the surface area and volume of the fish. The process begins with obtaining two synchronous images of the cameras and their subsequent correction by using the parameters obtained from the calibration. Once the images are corrected, the fish real-time image segmentation algorithm is executed individually for up-view image and side-view image. The proposed real-time image segmentation algorithm was described in section 5.2.2. It is done for up-view image to obtain fish length and width in pixels, and the same process is done for side-view image to obtain fish length and height in pixels.

The first process is done for upview image so that length ( $L$ ) and width ( $W$ ) are obtained, and these results are stored as a save model. The next process is done for side view to get length ( $L$ ) and height ( $H$ ), and this result is also saved in a save model. For last process, the values of  $LWH$  are used for the calculation process of surface area and volume.

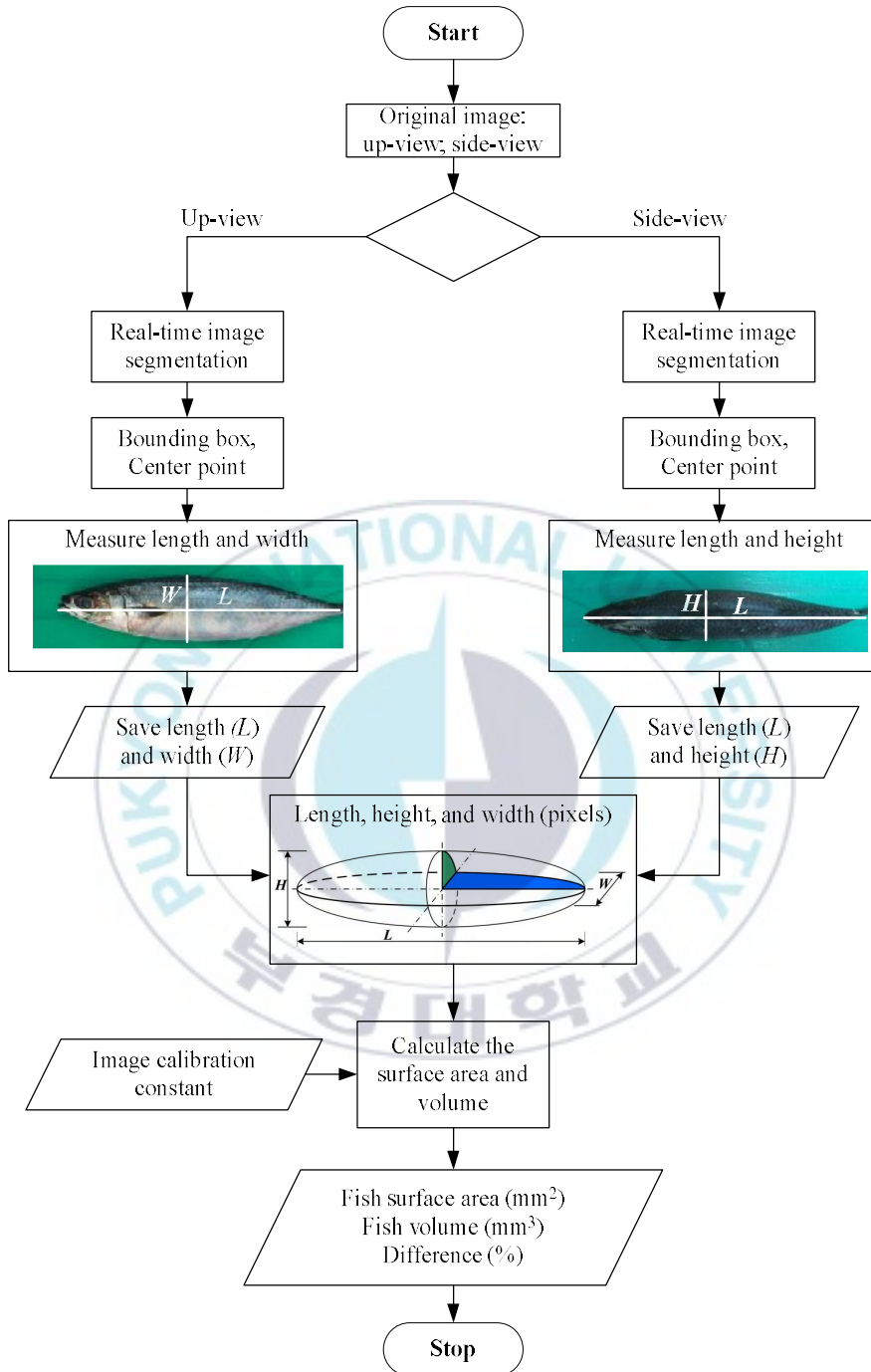


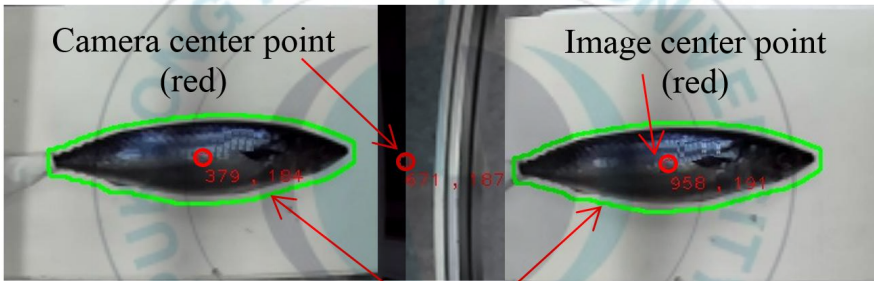
Fig. 5.24 Flowchart to calculate fish surface are and volume.

### 5.3.4 Experimental results of fish surface area and volume measurement based on 3D coordinate

Fig. 5.25 shows the representation of the right camera and the left camera in real-time image segmentation.

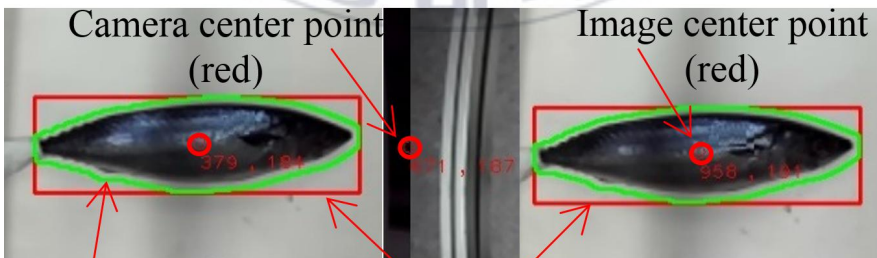


(a) Left and right thresholded images



Contour (green line)

(b) Left and right original RGB color images



Contour (green line)      Bounding box (red line)

(c) Left and right original RGB color images with bounding box

Fig. 5.25 Representation of the right camera and left camera

The white color area of the fish threshold image in Fig. 5.25(a) is represented by the inside area of the green line in the fish original RGB color image of Fig. 5.25(b). The white color area in threshold image and the green line in the original RGB color image are visible for the left camera and right camera. In other words, image segmentation works well. It is also indicated by the bounding box in the green line area, the centroid of the left-right original image (red), and the centroid between the left camera and the right camera (red).

The length ( $L$ ), width ( $W$ ), and height ( $H$ ) of the fish image are represented by the length, width, and height of the bounding box (in pixels). The computation of the centroid is required for both images obtained with the stereo camera system because calculating the surface area and volume can be limited to one image. Fig. 5.25(a) shows the thresholded image of the target analyzed in one example image. Fig. 5.25(b) shows the detection results of the fish to be analyzed: centroid location (red circle), and contour (green line). Fig. 5.25(c) shows the detection results of the fish to be used for calculating surface area and volume of the fish. The result obtained in this case shows the centroid location (red circle), contour (green line), and bounding box in stereo camera image. One example of the object experiment result is shown in Fig. 5.25(b) and Fig. 5.25(c). In this result, the image centroid for the left camera in pixels is (379,184), the center of the image for the right camera in pixels is (958,191), and the image center is for stereo cameras in pixels (671,187). From this value, the distance from the planes of the two cameras to the plane of the pixel can be obtained.

Table 5.2 shows the 2D image coordinate (pixels) of the centroid in stereo camera. The results of the 3D coordinate (mm) are shown in

Table 5.3. Based on the experimental results obtained for the measurement of 3D coordinate as shown in Table 4.3, the smallest distance error rate is at a distance of 550 mm. After that, a distance 550 mm will be used to adjust the distance between stereo camera and an object in measuring the surface area and volume of the fish. Table 5.4 shows the measurement results of surface area and volume of four fishes using 3D coordinate. To calculate the difference between the partition method and analytic method, Eq. (3.2) is used.

Table 5.2 Image coordinate of the centroid point

Trial	Centroid in 2D coordinate (pixels)		Real distance Z (mm)
	X	Y	
1	687	203	780
	680	194	660
	671	187	550
2	687	203	780
	680	194	660
	671	187	550
3	687	203	780
	680	194	660
	671	187	550

Table 5.3 Measurement data of 3D coordinate.

Trial	Centroid in 3D coordinate (mm)			Real distance Z (mm)	Distance error rate $e_d$ (%)
	X	Y	Z		
1	16	20	793.2	780	1.69
	16	20	667.7	660	1.17
	16	20	553.4	550	0.62
2	16	20	792.9	780	1.65
	16	20	667.5	660	1.14
	16	20	553.2	550	0.58
3	16	20	791.6	780	1.49
	16	20	667.1	660	1.08
	16	20	552.6	550	0.47

Table 5.4 Measurement results of surface area and volume of four fishes using 3D coordinate.

Fishes sample size (mm)				Surface area (mm <sup>2</sup> )		
	L	H	W	Real-time method	Analytic method	Error $e_d$ (%)
1	290	38.22	51.1	173,159.92	164,428.75	5.31
2	287	37.12	49.0	167,981.93	160,028.51	4.97
3	289	38.20	50.5	170,715.11	163,020.54	4.72
4	287	37.00	48.9	166,746.44	159,963.96	4.24
	L	H	W	Volume (mm <sup>3</sup> )		
1	290	38.22	51.1	311,256.65	296,406.67	5.31
2	287	37.12	49.0	286,384.78	273,189.71	4.83
3	289	38.20	50.5	305,330.52	291,763.51	4.65
4	287	37.00	48.9	282,648.04	271,750.83	4.01

## 5.4 Summary

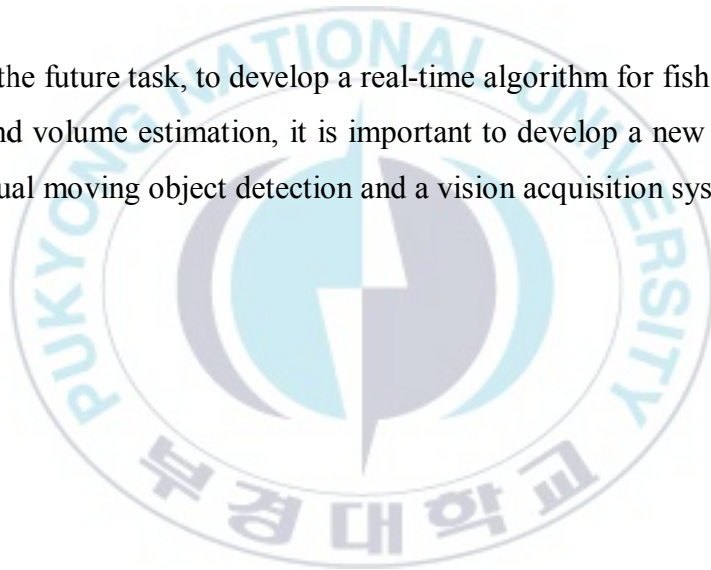
A method for image segmentation and determination of 3D coordinate for fish surface area and volume measurement by using stereo camera was proposed. The segmentation process was done in real-time on the video frame. To reduce complexity and computation time, the H, S, and V were segmented separately before they are combined. The result of this segmentation was the targeting object in which its coordinate was measured. Experiment results show that real-time image segmentation of the proposed method had a good result. The experiments demonstrated that the calibration process could quickly detect the chessboard corners. After the calibration results, focal lengths of the left camera and right camera were about 2.8289 mm and 2.8311 mm, respectively. The focal length difference between two cameras was about 0.00221 mm. For desired object distances of 780 mm, 660 mm, and 550 mm, the distance error rate was less than 2% for both distances of 650 mm and 550 mm in three trial times. However, for 780 mm, the distance error rate was bigger than the two distances of 550 mm and 660 mm and was more than 3%. 3D coordinate measurement results showed that distance error was increased in Z coordinate by increasing the distance and this was caused by the field of view of the camera. Therefore, for the next analysis, namely measuring the fish surface area and volume uses a distance of 550 mm.

The surface area and volume of fish were measured by the proposed analytic measurement method and real-time measurement method. Experimental results using sample of four fishes show that the differences of surface area and volume were 4.24%~5.31% and

4.01%~5.01%, respectively. The process of real-time image segmentation, feature extraction, and measurement fish surface area and volume takes time 0.0018 milliseconds.

The real-time image segmentation, 3D information, and measurement methods for surface area and volume proposed in this dissertation could be useful for fish recognition and sorting applications. The 3D information based stereo camera could be applied to an automated fish processing system to handle fish on a conveyor belt.

In the future task, to develop a real-time algorithm for fish surface area and volume estimation, it is important to develop a new method for visual moving object detection and a vision acquisition system.



## **Chapter 6: Real-time Measurement Method of Moving Objects for Fish Surface Area and Volume**

This chapter proposes a real-time measurement method of moving objects for fish surface area and volume. This proposed method uses a stereo camera for acquiring 3D information from moving objects and determines their size. The measurement system used in this proposed method was explained in Fig. 3.4 of section 3.3. To determine the size of objects which cannot be contained within the camera field of view, it is useful to be able to track its contours. To complete this task, the following steps are done. Firstly, a segmented object is shown as the target view. Secondly, each image is classified and stored in computer as image library. Thirdly, stereo camera automatically identifies the targeting object by matching the two views of the contour. Fourthly, at two contours matching position, the stereo camera measure the object centroid and the object size. Finally, the effectiveness of a real-time measurement method for moving objects is compared with the analytical method through experimental results.

### **6.1 Proposed measurement method in real-time for moving object**

Moving object detection visually involves segmentation of the target object in the sequence of images. Accurate visual object detection must involve tracking the object itself. This section focuses

on solving the segmentation problem used for moving object detection and object tracking, and measurement problem of moving objects.

One of the problems of image segmentation is of pigmented skin. The fish skin is categorized as pigmented skin. The segmentation problem of pigmented skin is solved by real-time image segmentation.

Fig. 6.1 shows examples of the sequence of image frames of visual object tracking using stereo camera. The sequence of image frames are shown by  $k$ . Fig. 6.1(a) shows the part of the fish body entering the camera field of view area. There are no contours detected in this frame. In Fig. 6.1(b) of the  $(k+1)^{\text{th}}$  frame, the left camera and the right camera can detect the contours of fish. However, there are no bounding boxes detected in this frame. In Fig. 6.1(c) of the  $(k+2)^{\text{th}}$  frame only the right camera can detect the contours of fish. Therefore, the 3D coordinate measurement does not work in Fig. 6.1(a)~(c). In Fig. 6.1(d) of the  $(k+3)^{\text{th}}$  frame, the left camera and the right camera can detect the contours of the fish and have bounding boxes on both cameras. In this frame, the 3D coordinate measurement is working well.

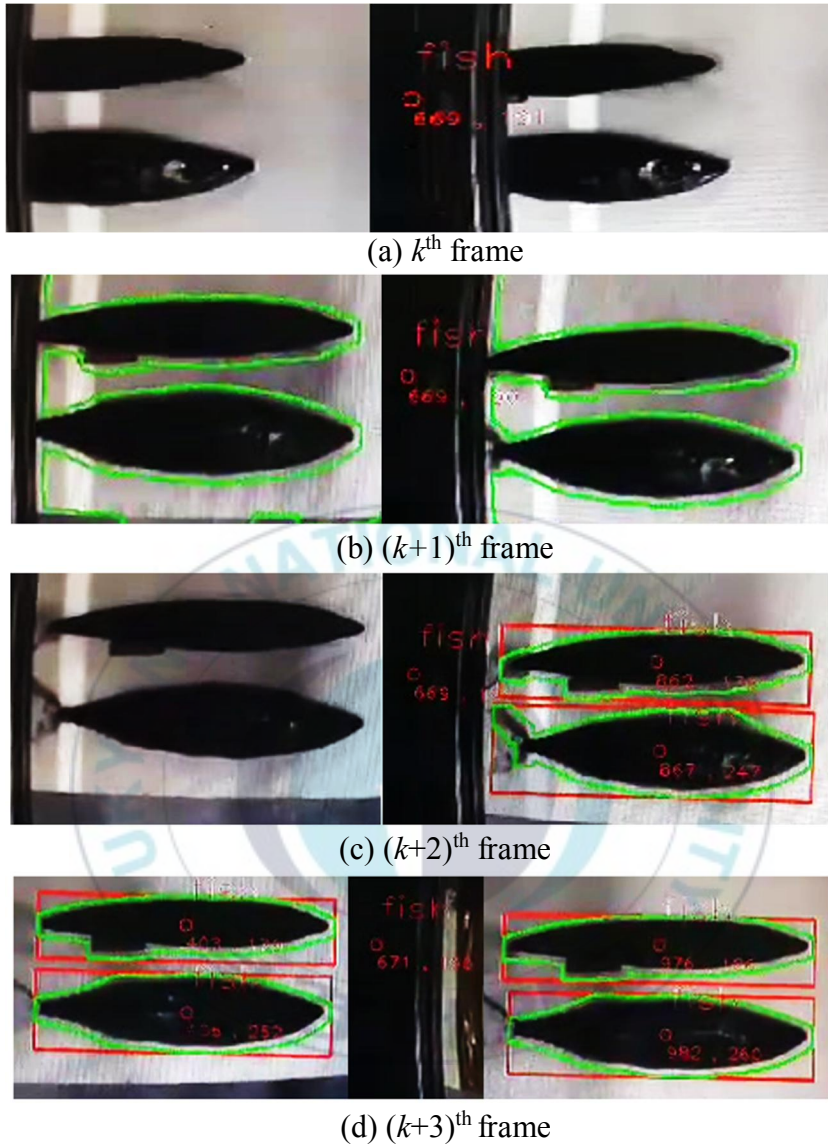


Fig. 6.1 Examples of the sequence of stereo camera image frames.

The following steps explain the algorithm used for finishing a visual moving object detection and measurement method.

**Step 1:** Segmented object is shown as the target view. This step consists of detecting and segmenting the targeting object located in the object image plane. Image segmentation is done

in real-time applied for online object detection and tracking.  
The output of this step is the 2D coordinate of the object.

**Step 2:** A selected contour is automatically extracted and its image shape is stored as pseudo code in computer memory.

**Step 3:** The position of the stereo camera is set based on the reference position of the object relative to the planar contour.

**Step 4:** Create a motion model and determine a tracking window for a moving object in the stereo camera scene area. The stereo camera automatically identifies the moving object. In this step, start moving the object as the first frame. To identify the moving object is done by tracking its contours. The object tracking is predicted based on the states estimated using Kalman filter.

**Step 5:** Search the contour of the moving object on the tracking window in the scene. In this step, the contour of the moving object will merge with the contour in image classification on computer memory if they are similar. In this step, the tracking contour is complete.

**Step 6:** Measure the fish surface area and the volume based on the proposed 3D coordinate measurement method. After measuring, then keep tracking the moving object until it disappeared.

**Step 7:** Go to to step 5 for the next frame.

The next discussion will explain the details of these seven steps. Fig. 6.2 shows the flowchart of the proposed moving object detection and measurement algorithm.

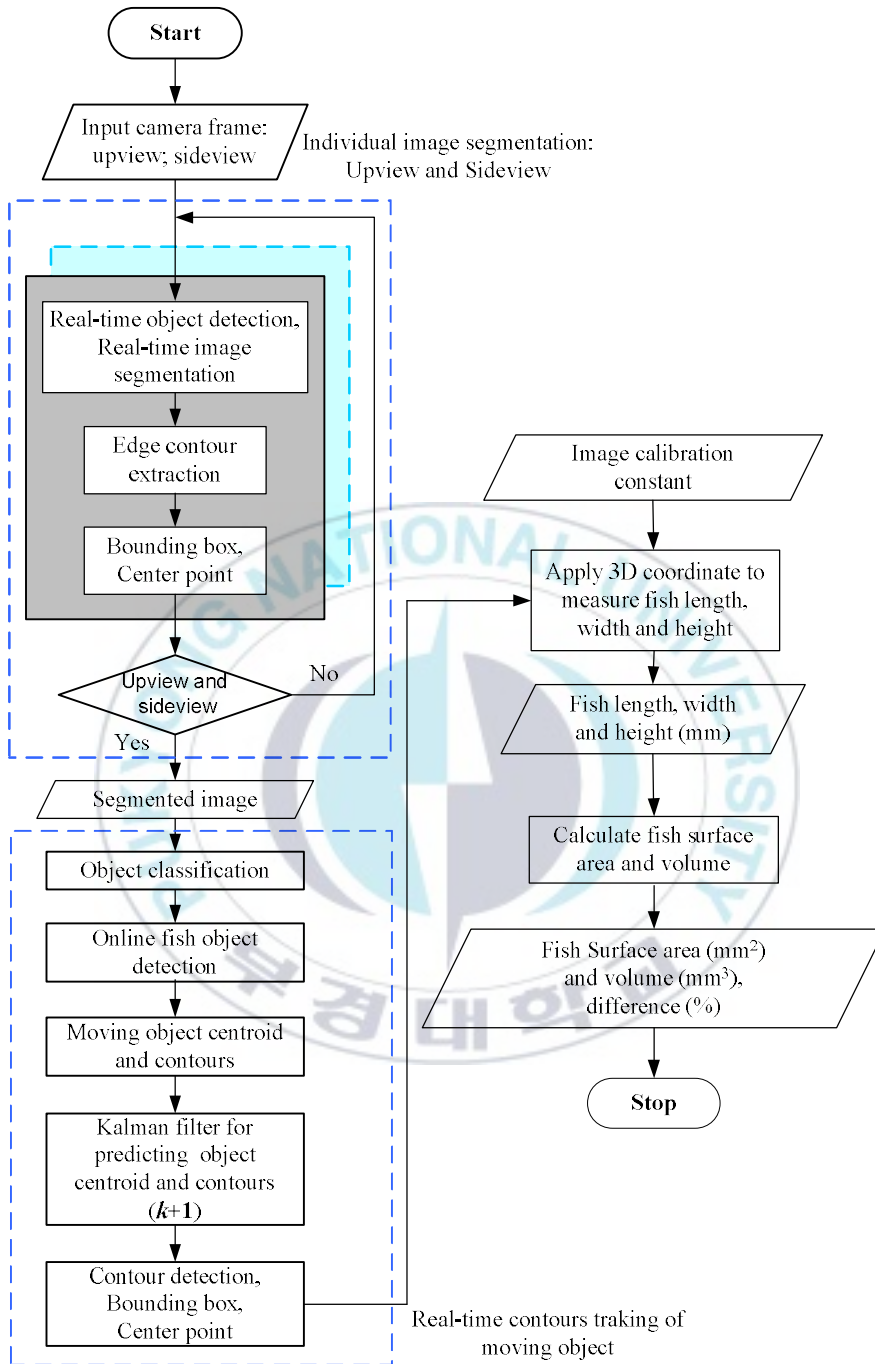


Fig. 6.2 Flowchart of the proposed moving object detection and measurement algorithm

### 6.1.1 Real-time image segmentation for moving object detection

This section presents a real-time image segmentation for detecting a moving object. The real-time segmentation method in section 5.2.2 is applied for the object segmentation. Image segmentation is done individually for fish side-view and up-view. It is done by combining the threshold, mathematical morphological transformation, and contour detection techniques to extract objects in a graph-based image.

Fig. 6.3 shows the image segmentation and contour detection process used for detecting a moving object. As shown in Fig. 6.4(a), the input image contains the foreground and background pieces of information of the object that needs to be solved. After receiving the image, the threshold method is applied to distinguish between the background and the object.

A bw image is obtained after applying the threshold 0.75 (scale 1.0) as shown in Fig. 6.3(b). Then, two morphology of dilation and erosion are applied to remove noise. The results are shown in Fig. 6.3(c) and Fig. 6.3(d). The contour of the object is retrieved from the previous step using the algorithm proposed in work [73]. The contour detection algorithm provides object information in the image plane including the centroid location, the orientation, and the area as shown in Fig. 6.3(e).



(a) Original RGB color image



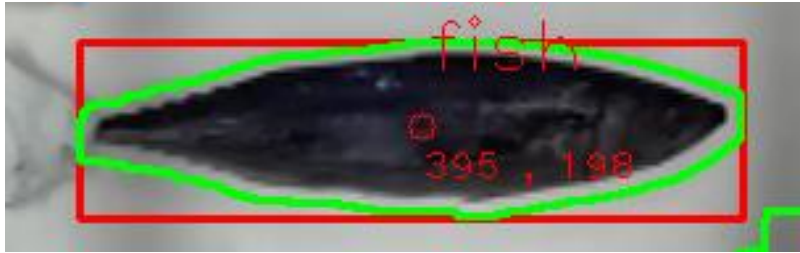
(b) bw image with threshold 0.75



(c) Dilation image



(d) Erosion image



(e) Original RGB color image with contour and bounding box

Fig. 6.3 Image segmentation and contour detection.

### 6.1.2 Object classification

Object detection includes the following parts: data, features, and classifier. Data are represented by input images, and a specific type of feature is chosen from input images. The type of feature represents different characteristics of objects. In the final stage, the proper classifier is applied to learn from obtained features and to provide the ability to detect objects in new images. Every object is treated as individual image segmentation that pass through a classifier for identification.

Every object map is created from an individual image segmentation by classifying each region with one of many available classification algorithms. Object classification used in this proposed method adopts a library for support vector machines (LIBSM) principle in [73]. Fig. 6.4 shows the flowchart of the object classification.

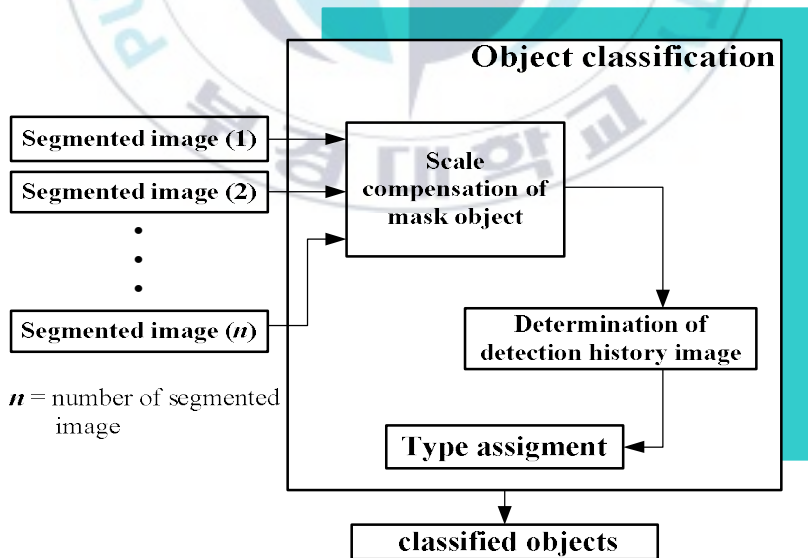


Fig. 6.4 Flowchart of the object classification.

### 6.1.3 Tracking contour of a moving object

The contour that shows the position of the current object determined using centroid coordinates, speed, and acceleration. The next state of the contour is predicted based on the states estimated using Kalman filter [74]. To get the correct contour in the next frame, the first centroid of the contour is obtained in a new frame and then the best contour is estimated by looking for a contour environment. The best fit of contour is a contour which has the maximum energy as follows:

$$E = nF - nB \quad (6.1)$$

where  $E$  is energy,  $nF$  is total number of pixels lying inside the contour which belong to a foreground object, and  $nB$  is the total number of pixels lying inside the contour which belongs to background. Pixel which lies inside the contour is said to be the foreground pixel if

$$(p_c - c)^T \Sigma^{-1} (p_c - c) < n\lambda \quad (6.2)$$

where  $c$  is the center of a bin in the object histogram,  $p_c$  is the color vector associated with pixel  $p$ ,  $\Sigma$  is a covariance matrix and only contains diagonal terms,  $\lambda$  is a user defined constants, and  $n$  is the dimension of the feature vector.

At any time  $k$ , the position of the contour is defined by specifying its centroid  $(x_t, y_t)$  and predicted by using the discrete time equations as follows:

$$\begin{cases} x_k = x_{k-1} + v_{x,k-1} + 0.5a_{x,k-1} \\ y_k = y_{k-1} + v_{y,k-1} + 0.5a_{y,k-1} \end{cases} \quad (6.3)$$

where

$$v_{x,k} = x_k - x_{k-1}; \quad v_{y,k} = y_k - y_{k-1} \quad (6.4)$$

$$a_{x,k} = v_{x,k} - v_{x,k-1}; \quad a_{y,k} = v_{y,k} - v_{y,k-1} \quad (6.5)$$

where  $v$  and  $a$  are velocity and acceleration, respectively.

After estimating the new state of the contour, the stochastic search is performed to get the best fit contour. From the contour represented by a set of points  $(x_k, y_k)$ , for  $(k = 1, 2, \dots, n)$ , the position of the  $k^{\text{th}}$  contour point can be searched. The correct position of the  $k^{\text{th}}$  contour point that is the values of  $x$  and  $y$  are searched stochastically in the range as follows:

$$\begin{cases} (x_k - 2\sigma_x) \text{ to } (x_k + 2\sigma_x) \\ (y_k - 2\sigma_y) \text{ to } (y_k + 2\sigma_y) \end{cases} \quad (6.6)$$

where  $\sigma_x$  and  $\sigma_y$  are the standard deviation of the prediction error in  $x$  and  $y$  direction, respectively.

$\sigma_x$  and  $\sigma_y$  are written as follows:

$$\begin{cases} \sigma_{x,k} = \beta \sqrt{(x_{k-1} - \hat{x}_{k-1})^2} + (1 - \beta) \sigma_{x,k-1} \\ \sigma_{y,k} = \beta \sqrt{(y_{k-1} - \hat{y}_{k-1})^2} + (1 - \beta) \sigma_{y,k-1} \end{cases} \quad (6.7)$$

where  $(\hat{x}_{k-1} - \hat{y}_{k-1})$  and  $(x_{k-1} - y_{k-1})$  are the predicted and the exact values of the contour centroid at time  $k-1$ , and  $\beta$  is the learning rate. After a new position of the contour is gotten, modeling parameters of the Kalman filter are updated based on the prediction error.

### 6.1.4 3D coordinate measurement of a moving object

The 3D coordinate measurement of a moving object uses feature bounding box in the captured image. Fig. 6.5 shows the 3D coordinate measurement technique of a moving object. Fig. 6.5(a) shows the experimental environment used for measuring a moving object. The first one is that the image segmentation is done in Section 6.1.2 and classify the feature image. This classified feature image is stored as pseudo code in computer memory. The second one is that the stereo camera identifies the targeting object automatically, and tracking its contours.

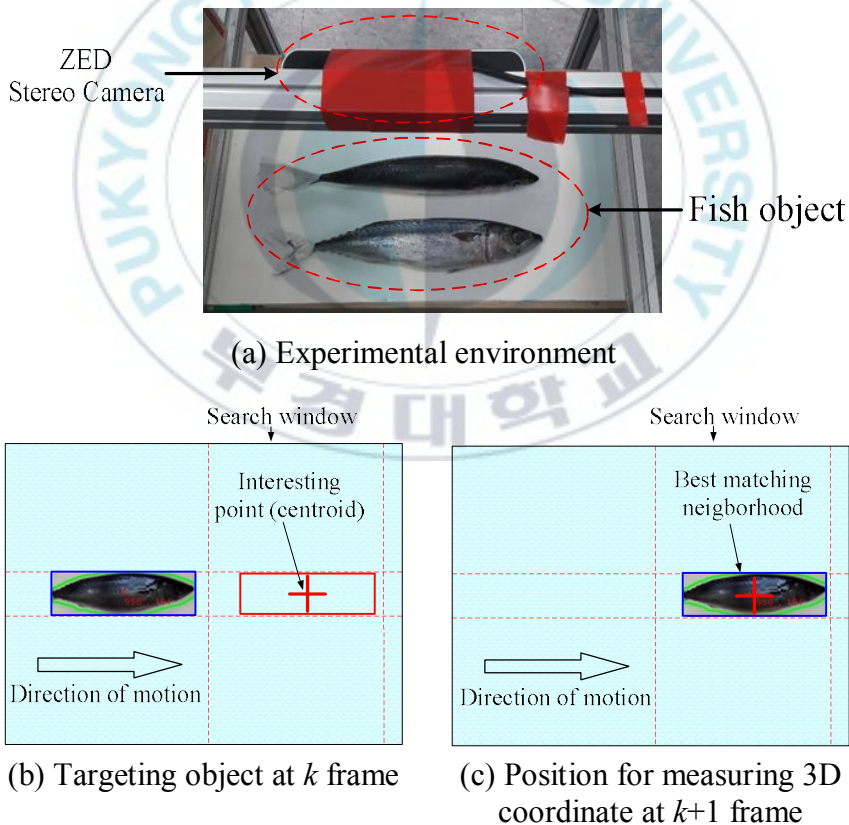


Fig. 6.5 3D coordinate measurement technique of moving object

As shown in Fig. 6.5(b), the object containing a fish image moves to the stereo camera area field of view with cross-line as a center point of camera. The object moves until the rectangle containing a fish image is merged to the rectangle with center point of the camera in the scene as shown in Fig. 6.5(c). Fig. 6.5(c) shows the exact position of the object to measure the 3D coordinates of the moving object.

## **6.2 Experimental results for moving objects**

The experiment results illustrated here demonstrate the feasibility of vision-based measurement of a moving object.

### **6.2.1 Experimental results of real-time image segmentation**

Fig. 6.6 shows one sample fish image implemented for segmented in stereo camera frame. Fig. 6.6(a) is the original RGB color image used for example in the real-time image segmentation. Fig. 6.6(b) shows the thresholded image obtained from the individual step of object detection and image segmentation step. Perfect image segmentation yields a good result for contour detection as shown in Fig. 6.6(c). Fig. 6.6(d) shows a result of an image combining the original RGB color image with the contour and the bounding box in the segmentation process. The bounding box and the circle are obtained in performing the image segmentation. This figure is a final step of the segmentation process and is used as image classification.

The image classification with contour and bounding box is useful for performing the real-time moving object detection and object measurement using a stereo camera.



(a) Original RGB color image



(b) Thresholded image



(c) Segmented RGB color image with contour



(d) Image classification with contour and bounding box

Fig. 6.6 Sample fish image made for segmented in stereo camera frame

## 6.2.2 Experimental results of tracking contour

This proposed method uses sampling time 30 fps. Thus the center positions of two moving objects in the adjacent two frames are little changed. Fig. 6.7 shows the experimental results for tracking contour of two moving objects (fish sideview and fish upview) using stereo camera. The stereo camera is starting from frame 1 as shown in Fig. 6.7(a), and the frame 2 is the image obtained by moving a plywood panel more than frame 1 as shown in Fig. 6.7(b). The contours on these frames are not detected by stereo camera. In these frames, the object is not shown in the measurement area. The tracking window has been set in the process of image segmentation and objects classification. This tracking window is used as a position for measuring surface area and volume of fish based on 3d coordinates. The object tracking is starting from frame 3 obtained by moving the panel more than the frame 2 as shown in Fig. 6.7(c), and the final tracking is frame 5 obtained by moving the panel more than the frame 4 as shown in Fig. 6.7(e). The contours on the Fig. 6.7(c) is detected by stereo camera. However, there is no centroid and bounding box on the object because the contour is not perfectly covered with the fish shape. The closed contours on Figs. 6.7(d)~(e) are visible. Therefore, the bounding box and centroid on the objects are available. Fig. 6.7(e) is the frame position of the object in performing a 3D coordinate measurement. For each object, a search is made by the bounding box to define its length, width and height of a correct object.

Fig. 6.7 shows that the proposed object tracking method in this chapter has good results. The stereo camera can detect moving objects, centroids, and track the contours. When the moving objects come into

the visible scene as a new tracking object, the stereo camera directly initialize a new tracking window for the new tracking object.



(a) Frame 1



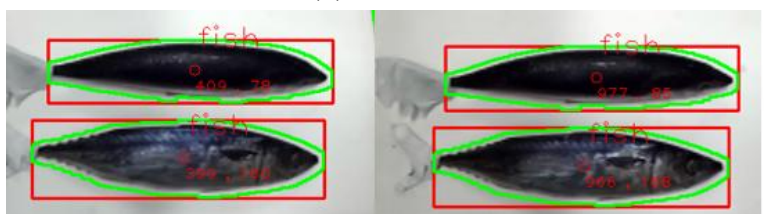
(b) Frame 2



(c) Frame 3



(d) Frame 4



(e) Frame 5

Fig. 6.7 Experimental results of tracking contour using stereo camera

The tracking results show that the proposed method can correctly handle a new entry and exit of the moving objects in the area monitoring scene.

### **6.2.3 3D coordinate measurement results of moving objects**

To measure surface area and volume of the fish in this experiment, image processing results in Fig. 6.7(e) are used. The result obtained in this case shows the centroid location (circle), contour, and bounding box in stereo camera image. By using the 3D coordinate measurement principle, the length, width and height of the fish are obtained. Table 6.1 shows experimental results of the 2D image coordinate in the stereo camera for up view and side view. This table shows the image centroids in pixels of the left camera, the right camera, and the stereo frame for upview and sideview. From this value, the distance from the planes of the stereo camera to the plane of the pixel can be obtained. Table 6.2 shows the measurement results of surface area and volume of four fishes using 3D coordinate. The difference between the proposed image processing method and the proposed analytic method is calculated using Eq. (3.2).

Further, the fish surface area and volume based on the proposed visual moving object detection and measurement method is confirmed by comparison with the values of the analytic, offline image processing, and real-time image processing methods. Table 6.3 shows the measurement difference of the partition method (offline image processing method), real-time image processing method, and real-time-moving object method.

Table 6.1 2D Image coordinate of the centroid point for moving object measurement

Centroid in 2D coordinate of upview (pixels)						Distance Z (mm)
Left camera		Right camera		Stereo frame		
X	Y	X	Y	X	Y	
409	78	977	85	670	231	550
Centroid in 2D coordinate sideview (pixels)						Distance Z (mm)
Left camera		Right camera		Stereo frame		
X	Y	X	Y	X	Y	
399	160	966	168	670	231	550

Table 6.2 Moving object measurement results of surface area and volume of four fishes using 3D coordinate.

Fishes sample size (mm)				Surface area (mm <sup>2</sup> )		
	L	H	W	Real-time moving objects method	Analytic method	Error $e_m$ (%)
1	290	38.22	51.1	174,508.24	164,428.75	6.13
2	287	37.12	49.0	170,990.46	160,028.51	6.85
3	289	38.20	50.5	173,861.40	163,020.54	6.65
4	287	37.00	48.9	168,506.04	159,963.96	5.34
	L	H	W	Volume (mm <sup>3</sup> )		
1	290	38.22	51.1	316,888.38	296,406.67	6.91
2	287	37.12	49.0	291,903.21	273,189.71	6.85
3	289	38.20	50.5	311,165.79	291,763.51	6.65
4	287	37.00	48.9	286,262.32	271,750.83	5.34

Table 6.3 Measurement difference comparison of the proposed offline, real-time, and real-time-moving object methods.

Fish sample	Partition method (Chapter 3)	Real-time method (Chapter 4)	Real-time moving objects method (Chapter 5)
Surface area error rate (%)			
1	6.03	5.31	6.13
2	5.42	4.97	6.85
3	5.91	4.72	6.65
4	5.31	4.24	5.34
Volume error rate (%)			
1	5.30	5.31	6.91
2	4.93	4.83	6.85
3	5.05	4.65	6.65
4	4.81	4.01	5.34

### 6.3 Summary

This chapter proposed a visual moving object detection and measurement method of fish surface area and volume. The position of the camera was adjusted perpendicular to the planar contour. To overcome the variety in color, edge contrast, texture, image size and noise on the scene, every image was segmented to produce multiple segmentations. These figures were used as image classification. The real-time moving object detection and tracking are performed after image classification.

The accurate classification was obtained for the proposed method because the stereo camera could detect objects in the left and right sides of the stereo camera. All the steps necessary for visual moving object detection for real-time image segmentation, classifications, and tracking were done. The measurement of fish surface area and volume using the moving platform showed good results. Experimental results of moving objects using the samples of four fishes show that the differences of surface area and volume were 5.34%~6.13% and 5.34%~6.91%, respectively. The execution time of the proposed method was 0.008 millisecond.

Difference in surface area and volume of the partition method were 6.03%~5.31% and 5.30%~4.81%, respectively. Difference of surface area and volume of the real-time method were 5.31%~4.24% and 5.31%~4.01%, respectively.

## **Chapter 7: Conclusions and Future Works**

### **7.1 Conclusions**

This dissertation proposed a measurement method for fish surface area and volume based on 3D-coordinate using an image processing method. The conclusion of this dissertation were summarized as follows:

**Chapter 2:** The mathematical modeling useful for fish surface area and volume calculations was presented. The fishes were considered as ellipsoid shapes to get analytical models for their surface area and volume estimation. The mathematical model of the surface area and volume of ellipsoid was derived using Green's theorem. The mathematical modeling consists of an analytic method deriving ellipsoidal area, surface area and volume, and a partition method applied for image processing. The image processing method used for image segmentation was also described. The mathematical morphology applied for image segmentation was also described. The main principle of stereo camera used for real-time image segmentation and 3D coordinate measurement were explained in detail. For moving object detection, tracking Kalman filter was used. The typical Kalman filter for multi-object tracking using Kalman filter was also described.

**Chapter 3:** The hardware structures for fish measuring systems used for this dissertation were described. The structure hardware was used for a proposed analytical measurement method and partition measurement method for fish surface area and volume used in chapter 4, a proposed real-time measurement method for fish surface area and

volume used in chapter 5, and a proposed real-time measurement method of moving objects for fish surface area and volume used in chapter 6. The structures hardware include a personal computer (PC), monitor screen, LED lamp, HD camera, stereo camera, frame, fixed or moving plywood panel, etc.

**Chapter 4:** A partition method for calculating fish surface area and volume were designed. The fish image was segmented before calculations of surface area and volume. Image segmentation was done based on mathematical morphology, image edge detection, and contour detection. The edge detection applied the Sobel operator and the contour detection applied Kernels. The sample images used to validate the proposed method were images of four fishes. The hardware structure was arranged to apply an image processing method for fish surface area and volume calculations. It consisted of one personal computer (PC), one high density (HD) camera, light source, plywood panel, etc. The HD camera was used to acquire two images, one from the top view and one from the side view as images acquisition. The source code used for measurement was built using Matlab programming language and applied for offline application. Measurement of surfaces area and volumes of four fishes were done by experiment through image processing by applying the partition method. Measurement of surface area and volume of four fishes were done experimentally through image processing by applying the partition method. Approximation of the fish's surface area and volume in the analytical method was compared to the image processing method. Experimental results using samples of four fishes showed that the differences between the proposed analytical method and the proposed image processing method (partition method) in surface area were

5.42%~6.03% and the differences of volume were 4.93%~5.30%. Therefore, the proposed partition method by the image processing method was valid.

**Chapter 5:** The proposed partition measurement method used in the chapter 4 was valid because the difference between the partition method by the image processing method and analytical method was small. However, the algorithm was built for offline method. A real-time image segmentation and a measurement method for fish surface area and volume based on 3D coordinate using stereo camera were proposed. The proposed real-time image segmentation method could solve the problems of an image captured by a stereo camera such as excessive information, complex disparities, and the significant change of the shape and appearance of regions. The real-time image segmentation and 3D coordinate measurement method could increase the capacity of measurement, accuracy and execution time. For real-time applications of image segmentation and feature-extraction, open source computer vision (OpenCV, C++) and ZED camera as stereo camera were used.

The stereo camera was calibrated to collect its intrinsic parameters and distortion parameters. Real-time image segmentation and feature extraction were done to extract objects in a graph-based image. These were done by combining HSV color space, threshold, mathematical morphological transformation, and contour detection techniques. Finally, the object coordinate, surface area and volume of the fish were obtained.

Experiment results showed that real-time image segmentation of the proposed method had a good result. The experiments demonstrated

that the calibration process could quickly detect the chessboard corners. After the calibration results, focal length of the left camera and right camera were about 2.8289 mm and 2.8311 mm, respectively. The focal length difference between two cameras was about 0.00221 mm. For desired object distances of 780 mm, 660 mm, and 550 mm, the distance error rate was less than 1.69% for three trial times. For distances of 650 mm and 550 mm, the error rate was less than 0.47%~1.17% for three trial times. However, for 780 mm, the distance error rate was bigger than the two distances of 550 mm and 660 mm and was 1.49~1.69%. 3D coordinate measurement results showed that the distance error was increased in Z coordinate by increasing the distance, and this was caused by the field of view of the camera. Therefore, to measure the surface area and volume of fish by the 3D coordinate technique, a distance of 550 mm was used in this dissertation.

Experimental results using samples of four fishes showed that the differences of surface area and volume were 4.24%~5.31% and 4.01%~5.01%, respectively. The execution times of image segmentation and feature extraction in the offline method and the real-time method were 23 milliseconds and 0.0019 millisecond, respectively.

The real-time image segmentation, 3D information, and measurement methods for surface area and volume proposed in this dissertation could be useful for fish recognition and sorting applications. The 3D information based stereo camera could be applied to an automated fish processing system to handle fish on a conveyor belt.

**Chapter 6:** A visual moving object detection and measurement was proposed. The objects were moving and a stereo camera determined the size of objects. The size of the objects which cannot be contained within the camera field of view was determined by tracking its contours. Real-time image segmentation and feature extraction were done for each object. Furthermore, a selected contour was automatically extracted and its image shape was stored as objects classifications. Finally, the stereo camera tracked the contour of the object at the reference position relative to the planar contour, and measured the centroid, the surface area and volume of the object.

To overcome the variety in color, edge contrast, texture, image size and noise on the scene, every image was segmented to produce multiple segmentations. The object classification was applied after individual image segmentation. After that, real-time moving object detection and tracking were done. The accurate classification was obtained for the proposed method because the stereo camera can detect objects in the left and right sides of the stereo camera.

All the steps necessary for visual moving object detection for real-time image segmentation, classifications, and tracking were done. The measurement of fish surface area and volume using the moving platform showed good results.

Experimental results of the real-time moving object method using the samples of four fishes showed that the differences of surface area and volume were 5.34%~6.13% and 5.34%~6.91%, respectively. Mean difference surface area and volume of the offline method and real-time method were 5.3%~6.03%, 4.81%~5.30%, and 4.4%~5.31%, respectively.

The effectiveness of a measurement method for fish surface area and volume based on 3D coordinate using image processing method was shown through experimental results. The proposed partition measurement method based on partition using image processing, measurement method in real-time based on 3D coordinate, and measurement method in real-time for moving objects showed good results. Therefore, the proposed partitioned measurement method for fish surface area and volume using the image processing method can be implemented in automated systems.

## **7.2 Future works**

As for this dissertation, the future works will be made as follows:

- To minimize the measurement error in the offline method, improving a new image segmentation method is needed.
- Hardware design for object detection and tracking in the real-time method is needed to improve with two pairs of stereo camera.
- The ability of the real-time method is needed to be tested on real fish in the water with multi stereo camera.

## References

- [1] M. F. Jeebhay, T. G. Robins and A. L. Lopata, "World at Work: Fish Processing Workers," *Occupational and Environmental Medicine*, Vol. 61, No. 5, pp. 471–474, 2014.
- [2] E. S. Bridge, R. K. Boughton, R. A. Aldredge, T. J. E. Harrison, R. Bowman, and S. J. Schoech, "Measuring Egg Size Using Digital Photography: Testing Hoyt's Method Using Florida Scrub-Jay Eggs," *Field Ornithol*, Vol. 78, No. 1, pp. 109–116, 2007.
- [3] R. Badonia, A. Ramachandran and T. V. Sankar, "Quality Problems in Fish Processing," *Journal of the Indian Fisheries Association*, Vol. 18, pp. 283–287, 1988.
- [4] A. Getu, K. Misganaw and M. Bazezew, "Post-Harvesting and Major Related Problems of Fish Production," *Fisheries and Aquaculture Journal*, Vol. 6, 2015.
- [5] D. J. Lee, X. Xu, J. Eifert and P. Zhan, "Area and Volume Measurements of Objects with Irregular Shapes Using Multiple Silhouettes," *Optical Engineering*, Vol. 45, No. 2, 027202, 2006.  
<https://doi.org/10.1117/1.2166847>.
- [6] A. B. Koc, "Determination of Watermelon Volume using Ellipsoid Approximation and Image Processing," *Postharvest Biology and Technology*, Vol. 45, No. 3, pp. 366–371, 2007.
- [7] T. Y. Wang and S. K. Nguang, "Low Cost Sensor for Volume and Surface Area Computation of Axi-Symmetric Agricultural Products," *Journal of Food Engineering*, Vol. 79, No. 3, pp. 870–877, 2007.

- [8] R. J. Hughes, "Estimation of Shell Surface Area from Measurements of Length, Breadth, and Weight of Hen Eggs," *Poultry Science*, Vol. 63, No. 12, pp. 2471–2474, 1984.
- [9] N. N. Mohsenin, "Chapter 3: Physical Characteristics in Physical Properties of Plant and Animal Materials," Gordon and Breach Science Publishers: New York, NY, pp. 51–87, 1970.
- [10] S. M. A. Moustafa, "Theoretical Prediction of Volume, Surface Area and Center of Gravity for Agricultural Products," *Transactions of the ASAE*, Vol. 14, No. 3, pp. 549–553, 1971.
- [11] J. A. Marchant, "A Mechatronic Approach to Produce Grading," *Mechatronics: Designing Intelligent Machines*, pp. 159–164, 1990.
- [12] R. J. Hughes, "Estimation of Shell Surface Area from Measurements of Length, Breadth, and Weight of Hen Eggs," *Physiology and Reproduction*, Vol. 63, No. 12, pp. 2471–2474, 1984.
- [13] C. M. Sabliov, D. Boldor, K. M. Keener, and B. E. Farkas, "Image Processing Method to Determine Surface Area and Volume of Axisymmetric Agricultural Products," *International Journal of Food Properties*, Vol. 5, No. 3, pp. 641–653, 2002.
- [14] J. Wen, Q. Sun, Z. Sun, and H. Gu, "An Improved Image Processing Technique for Determination of Volume and Surface Area of Rising Bubble," *International Journal of Multiphase Flow*, Vol. 104, pp. 294–306, 2018.
- [15] M.O. Balaban, M. Chombeau, G. Bahar, D. Cirban, "Determination of Volume of Alaska Pollock (*theragra chalcogramma*) by Image Analysis," *Journal of Aquatic Food Product Technology*. Vol. 20, No. 1, pp. 45–52, 2011.

- [16] S. Damar, Y. Yagız, M. O. Balaban, S. Ural, A. C. M Oliveira, and C. A. Crapo, "Prediction of Oyster Volume and Weight using Machine Vision," *Journal of Aquatic Food Product Technology*, Vol. 15, No. 4, pp. 5–17, 2006.
- [17] K. Manikantan, B. V. Arun, K. Darshan, S. Yaradoni, "Optimal Multilevel Thresholds Based on Tsallis Entropy Method using Golden Ratio Particle Swarm Optimization for Improved Image Segmentation," *Procedia Engineering*. Vol. 30, pp. 364–371, 2012.
- [18] W. Hongzhi, J. Oliensis, "Generalizing Edge Detection to Contour Detection for Image Segmentation," *Computer Vision and Image Understanding*, Vol. 114, No. 7, pp. 731-744. 2010.
- [19] F. Wang, T. Zhang, and J. Deng, "A Novel Method Concerning about Image Transition Region Extraction and Segmentation," *International Conference on Multimedia Technology (ICMT)*, pp. 95–97, 2011.
- [20] H. Yao, Q. Duan, D. Li, J. Wang, "An Improved K-means Clustering Algorithm for Fish Image Segmentation," *Mathematical and Computer Modelling*, Vol. 58, No. (3–4), pp. 784-792, 2013.
- [21] J. Fischer, R. Bormann, G. Arbeiter, and A. Verl, "A Feature Descriptor for Texture-less Object Representation using 2D and 3D Cues from RGB-D Data," *Proceedings of the International Conference on Robotics and Automation, Karlsruhe, Germany*, pp. 2112–2117, May 2013.
- [22] B. Curless, M. A. Levoy, "Volumetric Method for Building Complex Models from Range Images," *Proceedings of SIGGRAPH*, pp. 303–312, 1996.

- [23] D Huber, "Automatic 3D Modeling Using Range Images Obtained from Unknown Viewpoints," Proceedings of the 3rd International Conference on 3D Digital Imaging and Modeling. IEEE Press, New York, pp. 153–160, 2001.
- [24] Wheeler M, Sato Y, Ikenuchi K (1998) Consensus Surfaces for Modeling 3D Objects from Multiple Range Images. IEEE Conference on Computer Vision, pp. 917–924
- [25] A. Fitzgibbon, G Cross, and A. Zisserman, "Automatic 3D Model Construction for Turn-Table Sequences," European Workshop SMILE, Lecture Notes in Computer Science, Vol. 1506, Springer, Berlin Heidelberg New York, pp. 155–170, 1998.
- [26] S. Seitz and C. R. Dyer, "Photorealistic Scene Reconstruction by Voxel Coloring, Proceedings of the IEEE conference on computer vision and pattern recognition, pp. 1067–1073, 1997.
- [27] S. Y. Park and M. Subbarao, "A Multiview 3D Modeling System Based on Stereo Camera Techniques," Machine Vision and Applications, Vol. 16, pp. 148–156, 2005.
- [28] T. Kenji, M. Toru, H. Okamoto, and K. Umeda, "3D Measurement Using a Fish-Eye Camera Based on EPI Analysis," Journal of Robotics and Mechatronics, Vol. 24, No. 4, pp. 677–685, 2012.
- [29] S. Spiess, M. Vincze, and M. Ayromiou, "On the Calibration of a 6-D Laser Tracking System for Dynamic Robots," IEEE Trans. on Instrumentation and Measurement, Vol. 47, No. 4, pp. 270–274, 1998.
- [30] S. P. Jaroslaw and I. A. Siltan, "Positioning Sensing of Industrial Robot-a Survey," Information Technology Journal, Vol. 5, No. 1, pp. 14–24, 2007.

- [31] J. Hancock and D. Langer, "Active Laser Radar for High-Performance Measurements," Proc. of IEEE International Conference on Robotics and Automation (ICRA), Vol. 2, pp. 1465–1470, 1998.
- [32] H. Fujiyoshi, S. Shimizu, T. Nishi, Y. Nagasaka and T. Takahashi, "Fast 3D Position Measurement with Two Unsynchronized Cameras," Proceedings of IEEE International Symposium on Computational Intelligence in Robotics and Automation, pp. 1239–1244, July 16-20, UHM, Kobe, Japan. 2003.
- [33] H. Kim, C. S. Lin, J. Song, and H. Chae, "Distance Measurement Using a Single Camera with a Rotating Mirror," International Journal of Control, Automation, and Systems, Vol. 3, No. 4, pp. 542–551, 2005.
- [34] Y.M. Mustafah, R. Noor, H. Hasbi, and A.W. Azma, "Stereo Camera Images Processing for Real-Time Object Distance and Size Measurements," Proceedings of the International Conference on Computer and Communication Engineering, pp. 659–663, Kuala Lumpur, Malaysia, 2012.
- [35] G. Takahashi, R. Matsuoka, "Accuracy of Measurement using a Pair of Stereo Images Acquired by Fine Pix Real 3D W1 Without Controls," International Archives of Photogrammetry, Remote Sensing and Spatial Information Sciences, Vol. 38, No. 5, pp. 565–570, 2010.
- [36] M. Jernej and V. Damir, "Distance Measuring Based on Stereoscopic Pictures," 9th International PhD Workshop on Systems and Control: Young Generation Viewpoint, Izola, Slovenia, October 2008.

- [37] C. Igathinathane, J.D. Davis, J.L. Purswell, and E.P. Columbus, "Application of 3D Scanned Imaging Methodology for Volume, Surface Area, and Envelope Density Evaluation of Densified Biomass," *Bioresource Technology*, Vol. 101, No. 11, pp. 4220–4227, June 2010.
- [38] N.V Ngo, Q.Ch. Hsu, W.L. Hsiao, and C.J. Yang, "Development of a Simple Three-Dimensional Machine-Vision Measurement System for in-Process Mechanical Parts," *Advances in Mechanical Engineering*, Vol. 9, No. 10, pp. 1–11, 2017.
- [39] K. Terabayashi, T. Morita, H. Okamoto, and K. Umeda, "3D Measurement Using a Fish-eye Camera Based on EPI Analysis," *Journal of Robotics and Mechatronics*, Vol. 24, No. 4, pp. 677–685, 2012.
- [40] K. Shimada, A. Namiki, and I. Ishii, "High-speed 3-D Measurement of a Moving Object with Visual Servo," *Proceedings of the 2016 IEEE/SICE International Symposium on System Integration*, pp. 248–253, Sapporo, Japan, December, 2016.
- [41] M. J. Kang, C. H. Lee, J. H. Kim, and U. Y. Huh, "Distance and Velocity Measurement of Moving Object Using Stereo Camera System," *Proceedings of International Conference on Control, Automation and Systems*, pp. 2181–2184, Seoul, Korea 2008.
- [42] T. R. Chandruptala and T. J. Osler, "The Perimeter of an Ellipse," *Math. Scientist*, Vol. 35, pp. 122–13, 2010.
- [43] G. Saravanan, G. Yamuna, and S. Nandhini, "Real-time Implementation of RGB to HSV/HSI/HSL and Its Reverse Color Space Models," *Proceedings of the International Conference on Communication and Signal Processing*, pp. 462–466, Apr. 2016.

- [44] R. Jain, R. Kasturi, B. G. Schunck, "Machine Vision," McGraw Hill, Inc., pp. 39–61, 1995.
- [45] J. Bernd, "Digital Image Processing," Springer-Verlag," Second edition, 1993.
- [46] J. C. Russ, "The Image Processing Handbook," CRC Press, Inc. and IEEE Press, 1995.
- [47] R. M. Haralick, S. R. Sternberg, and X. Zhuang, "Image Analysis Using Mathematical Morphology," IEEE Trans. Putt. Anal. Machine Intell., Vol. 9, No. 4, pp. 532–550, July 1987.
- [48] R. Wilson and A.H. Bhalerao, "Kernel Designs for Efficient Multi Resolution Edge Detection and Orientation Estimation," IEEE Transaction on Pattern Analysis and Machine Intelligence, Vol. 14, No. 3, pp. 384–392, 1992.
- [49] F. Yi and I. Moon, "Image Segmentation: A Survey of Graph-Cut Methods," International Conference on Systems and Informatics, pp. 1936–1941, 2012.
- [50] Y. Y. Boykov and M. P. Jolly, "Interactive Graph Cuts for Optimal Boundary and Region Segmentation of Objects in n-d Images," In IEEE International Conference on Computer Vision, Vol. 1, pp. 105–112, 2001.
- [51] Z. Zewei, W. Tianyue, L. Guo, T. Wang, and L. Xu, "An Interactive Method Based on the Live Wire for Segmentation of the Breast in Mammography Images," Computational and Mathematical Methods in Medicine, Vol. 2014, 2014.
- [52] R. N. Bracewell, "The Fourier Transform & Its Applications," Chapter Heaviside's Unit Step Function, pp. 61–65, McGraw Hill Science, Engineering Math, Third edition, 1999.

- [53] Y. Y. Boykov and M. P. Jolly, "Interactive Graph Cuts for Optimal Boundary & Region Segmentation of Objects in n-d Images," In IEEE International Conference on Computer Vision, Vol. 1, pp. 105–112, 2001.
- [54] B. Cyganek and J. P. Siebert, "An Introduction to 3D Computer Vision Techniques and Algorithms," John Wiley and Sons, Ltd, 2009.
- [55] R. Hartley and A. Zisserman, "Multiple View Geometry in Computer Vision," Second Edition, Cambridge University press, 2004.
- [56] R.E. Kalman, "A New Approach to Linear Filtering and Prediction Problems," Journal of Basic Engineering, Vol. 82, pp. 35–45, 1960.
- [57] S. Pathan, A. Al-Hamadi, and B. Michaelis, "Intelligent Feature-Guided Multi-Object Tracking Using Kalman Filter," 2009 2nd International Conference on Computer, Control and Communication, Vol. 6, pp. 17–18, 2009.
- [58] ZED Stereo camera. <https://www.stereolabs.com/>.
- [59] T. H. Nguyen, "Control of a Mobile Picking Robot for Path Tracking and Object Grasping using a 3D Vision Stereo Camera," PhD Thesis, Pukyong National University, 2016.
- [60] R. Cucchiara, C. Grana, A. Prati, and R. Vezzani, "A Hough Transform-Based Method for Radial Lens Distortion Correction," Proc. Int. IEEE Conf. Image Analysis Processing, pp. 182–187, 2003.
- [61] Z. Zhang, "A Flexible New Technique for Camera Calibration," IEEE Transactions on Pattern Analysis and Machine Intelligence. Vol. 22, No. 11, pp. 1330–1334, 2000.

- [62] <https://sourishghosh.com/2016/stereo-calibration-cpp-opencv/>
- [63] P. I. Corke and S. A. Hutchinson, "Real-time Vision, Tracking and Control," Proceedings of the International Conference on Robotics and Automation, pp. 622–629, Apr. 2000.
- [64] S. Helmer and D. Lowe, "Using Stereo for Object Recognition," Proceedings of the International Conference on Robotics and Automation, pp. 3121–3127, May 2010.
- [65] Y. Sumi, Y. Kawai, T. Yoshimi, and Tomita S, "3D Object Recognition in Cluttered Environments by Segment-Based Stereo Camera," International Journal of Computer Vision, Vol. 46, No. 1, pp. 5–23, Jan. 2002.
- [66] L. J. Belaid and W. Mouru, "Image Segmentation: a Watershed Transformation Algorithm," International Society for Stereology & Image Analysis, Tunis, Tunisia, pp. 93–102, Mar. 2009.
- [67] S. Zhu, X. Xia, Q. Zhang, and K. Belloulata, "An Image Segmentation Algorithm in Image Processing Based on Threshold Segmentation," Proceedings of the Third International IEEE Conference on Signal-Image Technologies and Internet Based System, Shanghai, China, pp. 673–678, Dec. 2007.
- [68] B. R. Lee, Q.B. Truong, V. H. Pham, and H. S Kim, "Automatic Thresholding Selection for Image Segmentation Based on Genetic Algorithm," Journal of Institute of Control, Robotics and Systems (in Korean), Vol. 17, No. 6, pp. 587–595, 2011.
- [69] F. Yi and I. Moon, "Image Segmentation: a Survey of Graph-Cut Methods," International Conference on Systems and Informatics, pp. 1936–1941, 2012.
- [70] X. Huang, Z. Qian, R. Huang, and D. Metaxas, "Deformable-Model Based Textured Object Segmentation," Proceedings of

- International conference on Energy Minimization Methods in Computer Vision and Pattern Recognition, pp. 119–135, 2005.
- [71] V. Lempitsky, P. Kohli, C. Rother, and T. Sharp, “Image Segmentation with a Bounding Box Prior, IEEE 12<sup>th</sup> International Conference on Computer Vision, pp. 277–284, 2009.
- [72] J. Fischer, R. Bormann, G. Arbeiter, and A. Verl, “A Feature Descriptor for Texture-Less Object Representation Using 2D and 3D Cues from RGB-D Data,” Proceedings of the International Conference on Robotics and Automation, Karlsruhe, Germany, pp. 2112-2117, 2013.
- [73] S. Suzuki and K. A. Be, “Topological Structural Analysis of Digitized Binary Images by Border Following,” Computer Vision, Graphics, and Image Processing, Vol. 30, No. 1, pp. 32–46, 1985.
- [74] X. Chen, X. Wang, and X. Jianhua, “Tracking Multiple Moving Objects Using Unscented Kalman Filtering Techniques,” International Conference on Engineering and Applied Science, 2012.
- [75] D. Zwillinger, “CRC Standard Mathematical Tables and Formulas,” Advances in Applied Mathematics, 33rd Edition, CRC Press, 2018.
- [76] E. W. Swokowski, “Calculus with Analytical Geometry,” Prindle Weber and Schmidt, Massachusetts, 1979.
- [77] C. E. Linderholm and A. C. Segal, “An Overlooked Series for the Elliptic Perimeter,” Mathematics Magazine, Vol. 68, No. 3, pp. 216–220, 1995.



## **Publication and Conference**

### **Published Journal**

1. **Jotje Rantung**, Jong Min Oh, Hak Kyeong Kim, Sea June Oh, and Sang Bong Kim, “Real-Time Image Segmentation and

- Determination of 3D Coordinate for Fish Surface Area and Volume Measurement Based on Stereo Camera,” Journal of Institute of Control, Robotics and Systems, Vol. 24. No. 2, pp. 76–82, 2018. KOREA ISSN 1976–5622 (Print), /ISSN 2233–4335 (Online)
2. **Jotje Rantung**, Minh Thien Tran, Hwan Yeol Jang, Jin Woo Lee, Hak Kyeong Kim and Sang Bong Kim, “Determination of the Fish Surface Area and Volume Using Ellipsoid Approximation Method Applied for Image Processing” Recent Advances in Electrical Engineering and Related Sciences, Lecture Notes in Electrical Engineering, Vol. 465, pp. 334–347, 2017. SCOPUS, ISSN 1876-1100 (Print), /ISSN 1876-1119 (Online)
  3. Jong Min Oh, **Jotje Rantung**, Sung Rak Kim, Sang Kwun Jeong, Hak Kyeong Kim, Sea June Oh and Sang Bong Kim, “Visual Servoing Controller Design Based on Barrier Lyapunov Function for a Picking System” Proceedings of 2018 Recent Advances in Electrical Engineering and Related Sciences, Lecture Notes in Electrical Engineering, Vol. 554, pp. 605–617, 2018. SCOPUS, ISSN 1876-1100 (Print), /ISSN 1876-1119 (Online)
  4. Minh Thien Tran, Huy Hung Nguyen, **Jotje Rantung**, Hak Kyeong Kim, Sea June Oh and Sang Bong Kim, “A New Approach of 2D Measurement of Injury Rate on Fish by a Modified K-means Clustering Algorithm Based on L\*A\*B\* Color Space,” Recent Advances in Electrical Engineering and Related Sciences, Lecture Notes in Electrical Engineering, Vol. 465, pp. 324–333, 2017. SCOPUS, ISSN 1876-1100 (Print), /ISSN 1876-1119 (Online)

### **Conference Paper**

1. Minh Thien Tran, **Jotje Rantung**, Trong Hai Nguyen, Hak Kyeong Kim and Sang Bong Kim, “Measurement of Injury Rate on Fish Skin and Performance Comparison Based on L\*A\*B\* and HSV Color Spaces” Proceedings of The 2<sup>nd</sup> International Joint Conference on Advanced Engineering and Technology and International Symposium on Advanced Mechanical and Power Engineering, Vol. 159, 2017. (Online)
2. **Jotje Rantung**, Jong-Min Oh, Sung-Won Kim, Sang-Kwun Jeong, Hak-Kyeong Kim, and Sang-Bong Kim, “Controller Design Framework based on Visual Servoing for A Picking System” Proceedings of 2018 International Symposium on Advanced Mechanical and Power Engineering (ISAMPE 2018), Shanghai, Republic of China, 2018.vg
3. **Jotje Rantung**, Chetan Chunilal Patel, Sung Rak Kim, Sang Kwun Jeong, Hak Kyeong Kim and Sang Bong Kim, “Real-time Multiple Object Detection on Cluttered Desk Based on Segmentation Method Using Stereo Camera,” 16 International Conference on Ubiquitous Robot 2019 (URAI), Jeju, Republic of Korea, (Accepted).

## Appendix A. The proof of Eq. (2.10) ~ Eq. (2.19)

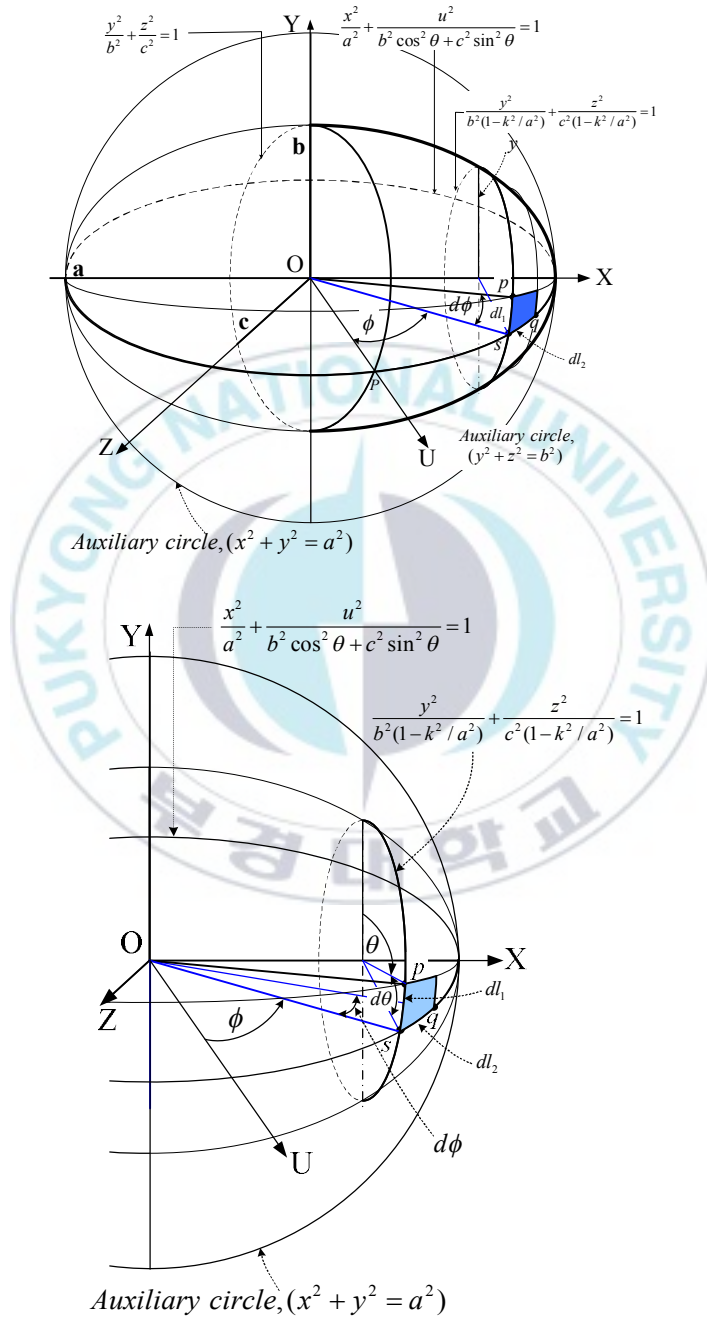


Fig. A.1 General standard ellipsoid and its auxiliary circle

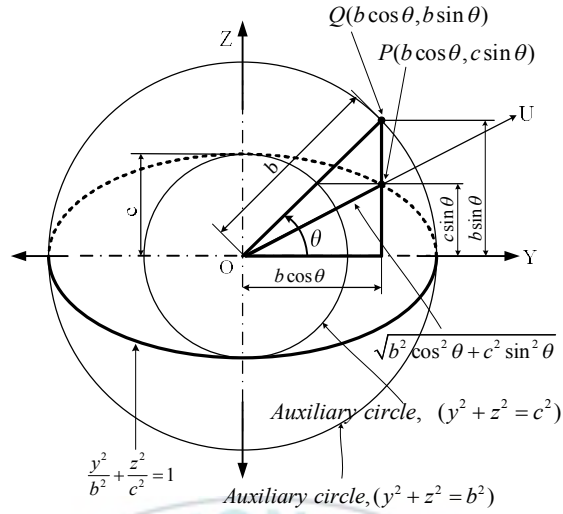


Fig. A.2 Ellipse and its auxiliary circle of (Y,Z) coordinate

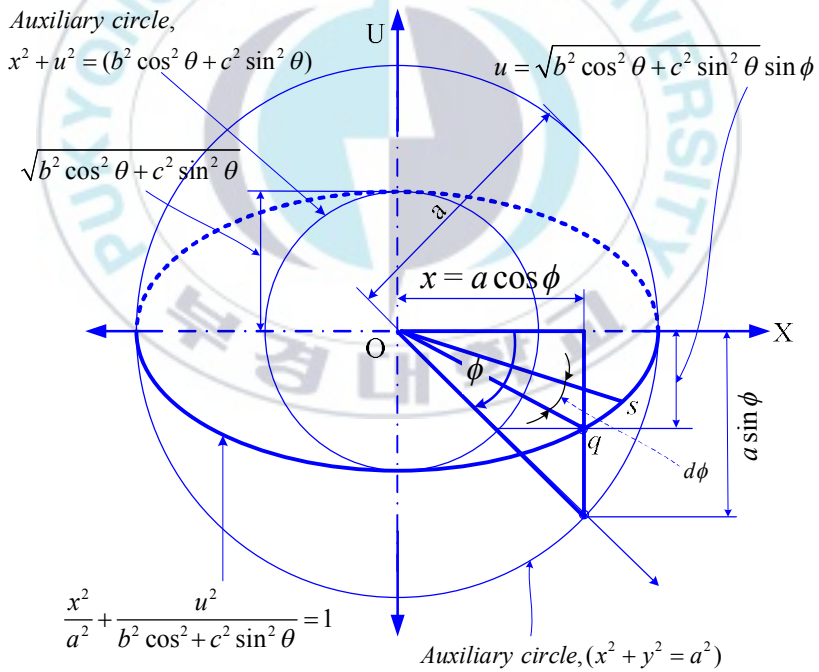


Fig. A.3 Ellipse and its auxiliary circle of (X,U) coordinate

Eq. (2.15) is given as

$$S = 8 \int_0^{\pi/2} \int_0^{\pi/2} \left( \sin \phi \sqrt{b^2 \sin^2 \theta + c^2 \cos^2 \theta} \right) \times \left( \sqrt{(b^2 \cos^2 \theta + c^2 \sin^2 \theta) \cos^2 \phi + a^2 \sin^2 \phi} \right) d\theta d\phi \quad (\text{A.1})$$

By taking  $A = a^2 - (b^2 \cos^2 \theta + c^2 \sin^2 \theta)$  and  $t = \cos \phi \rightarrow dt = -\sin \phi d\phi$ , Eq. (A.1) is expressed as follows

$$\begin{aligned} S &= 8 \int_0^{\pi/2} \int_0^{\pi/2} \left( \sqrt{b^2 \sin^2 \theta + c^2 \cos^2 \theta} \right) \times \left( \sqrt{a^2 (1 - \cos^2 \phi) + (b^2 \cos^2 \theta + c^2 \sin^2 \theta) \cos^2 \phi} \right) d\theta d\phi \\ &= 8 \int_0^{\pi/2} \int_0^{\pi/2} \left( \sqrt{b^2 \sin^2 \theta + c^2 \cos^2 \theta} \right) \times \left( \sqrt{a^2 - a^2 \cos^2 \phi + (b^2 \cos^2 \theta + c^2 \sin^2 \theta) \cos^2 \phi} \right) d\theta dt\phi \\ &= 8 \int_0^{\pi/2} \int_0^{\pi/2} \left( \sqrt{b^2 \sin^2 \theta + c^2 \cos^2 \theta} \right) \times \left( \sqrt{a^2 - (a^2 \cos^2 \phi - (b^2 \cos^2 \theta + c^2 \sin^2 \theta) \cos^2 \phi)} \right) d\theta dt\phi \\ &= 8 \int_0^{\pi/2} \int_0^1 \left( \sqrt{b^2 \sin^2 \theta + c^2 \cos^2 \theta} \right) \times \left( \sqrt{a^2 - (a^2 - (b^2 \cos^2 \theta + c^2 \sin^2 \theta))t^2} \right) d\theta dt \\ &= 8 \int_0^{\pi/2} \left[ \left( \sqrt{b^2 \sin^2 \theta + c^2 \cos^2 \theta} \right) \times \int_0^1 \left( \sqrt{a^2 - At^2} \right) dt \right] d\theta \quad (\text{A.2}) \end{aligned}$$

From [75],  $\int_0^1 \sqrt{a^2 - At^2}$  is obtained as follows:

$$\begin{aligned}
\int_0^1 (\sqrt{a^2 - At^2}) dt &= \sqrt{A} \int_0^1 \left( \sqrt{\frac{a^2}{A} - t^2} \right) dt \\
&= \frac{1}{2} \sqrt{A} \left( t \sqrt{\frac{a^2}{A} - t^2} + \left( \frac{a}{\sqrt{A}} \right)^2 \sin^{-1} \frac{t}{\frac{a}{\sqrt{A}}} \right) \Bigg|_0^1 \\
&= \frac{1}{2} \sqrt{A} \left( \sqrt{\frac{a^2}{A} - 1} + \left( \frac{a}{\sqrt{A}} \right)^2 \sin^{-1} \frac{1}{\frac{a}{\sqrt{A}}} \right) \\
&= \frac{1}{2} \left( \sqrt{\frac{a^2}{A} - 1} \times \sqrt{A} + \sqrt{A} \left( \frac{a}{\sqrt{A}} \right)^2 \sin^{-1} \frac{1}{\frac{a}{\sqrt{A}}} \right) \\
&= \frac{1}{2} \left( \sqrt{a^2 - A} + \sqrt{A} \left( \frac{a^2}{A} \right) \sin^{-1} \frac{1}{\frac{a}{\sqrt{A}}} \right) \\
&= \frac{1}{2} \left( \sqrt{a^2 - A} + \sqrt{A} \left( \frac{a}{\sqrt{A}/a} \right) \sin^{-1} \frac{\sqrt{A}}{a} \right) \\
&= \frac{1}{2} \left( \sqrt{a^2 - A} + a \frac{\sqrt{A}}{\sqrt{A}} \left( \frac{\sin^{-1} \sqrt{A}/a}{\sqrt{A}/a} \right) \right) \\
&= \frac{1}{2} \left( \sqrt{a^2 - A} + a \left( \frac{\sin^{-1} \sqrt{A}/a}{\sqrt{A}/a} \right) \right) \\
&= \frac{1}{2} \left( \sqrt{b^2 \cos^2 \theta + c^2 \sin^2 \theta} + a \left( \frac{\sin^{-1} \sqrt{A}/a}{\sqrt{A}/a} \right) \right) \tag{A.3}
\end{aligned}$$

Eq. (A.3) can be simplify as follows:

$$\begin{aligned}
 S &= 4 \int_0^{\pi/2} \left( \sqrt{b^2 \sin^2 \theta + c^2 \cos^2 \theta} \right) \times \sqrt{b^2 \cos^2 \theta + c^2 \sin^2 \theta} d\theta \\
 &+ 4a \int_0^{\pi/2} \left( \sqrt{b^2 \sin^2 \theta + c^2 \cos^2 \theta} \right) \times \left( \frac{\arcsin \sqrt{A/a}}{\sqrt{A/a}} \right) d\theta
 \end{aligned} \tag{A.4}$$

The semi-intermediate axis and semi-minor axis are equal for the prolate. By inserting  $c \approx b$  in Eq. (A.4) and simplifying it, the ellipsoid surface area become as follows:

$$\begin{aligned}
 S &= 4 \int_0^{\pi/2} \left( \sqrt{b^2 \sin^2 \theta + b^2 \cos^2 \theta} \right) \times \sqrt{b^2 \cos^2 \theta + b^2 \sin^2 \theta} d\theta \\
 &+ 4a \int_0^{\pi/2} \left( \sqrt{b^2 \sin^2 \theta + b^2 \cos^2 \theta} \right) \times \left( \frac{\arcsin(B)}{B} \right) d\theta \\
 &= 4 \int_0^{\pi/2} \left( \sqrt{b^2} \times \sqrt{b^2} \right) d\theta + 4a \int_0^{\pi/2} \left( \sqrt{b^2} \right) \times \left( \frac{\arcsin(B)}{B} \right) d\theta \\
 &= 4 \left( \sqrt{b^2} \times \sqrt{b^2} \right) \theta \Big|_0^{\pi/2} + 4a \left( \sqrt{b^2} \right) \times \left( \frac{\arcsin(B)}{B} \right) \theta \Big|_0^{\pi/2} \\
 S &= 2\pi b^2 + 2\pi \left( \frac{ab}{B} \right) \arcsin(B)
 \end{aligned} \tag{A.5}$$

where  $B = \frac{\sqrt{A}}{a}$

By substituting the value of  $B = \varepsilon$  into Eq. (A.5) and simplifying, the surface area of the prolate ellipsoid is as follows:

$$S = 2\pi b^2 + 2\pi \left( \frac{ab}{\varepsilon} \right) \arcsin(\varepsilon) \tag{A.6}$$

## Appendix B. The proof of Eq. (2.21)

Let  $OABC$  be the positive octant of the given ellipsoid which is bounded by planes  $OAB$  ( $z=0$ ),  $OBC$  ( $x=0$ ),  $OCA$  ( $y=0$ ), and surface  $ABC$ . General ellipsoid is as follows:

$$\frac{x^2}{a^2} + \frac{y^2}{b^2} + \frac{z^2}{c^2} = 1 \quad (\text{B.1})$$

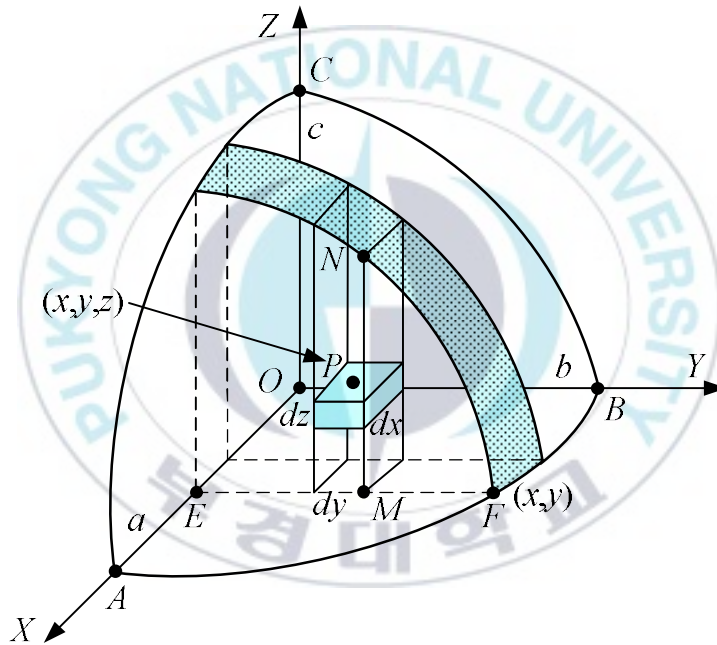


Fig. B.1 Ellipsoid element

Divide this region  $R$  into rectangular parallelepipeds of volume  $\delta x \delta y \delta z$  [76]. Consider such an element at  $P(x, y, z)$  in Fig. B.1.

$$\therefore \text{the required volume} = 8 \iiint_R dx dy dz \quad (\text{B.2})$$

In this region  $R$ ,

(i)  $z$  varies from 0 to  $MN$ , where

$$MN = z = c\sqrt{1 - \frac{x^2}{a^2} - \frac{y^2}{b^2}} \quad (\text{B.3})$$

(ii)  $y$  varies from 0 to  $EF$ , where  $EF = y = b\sqrt{1 - x^2/a^2}$  from the equation of the ellipse  $OAB$ , i.e.,

$$\frac{x^2}{a^2} + \frac{y^2}{b^2} = 1 \quad (\text{B.4})$$

(iii)  $x$  varies from 0 to  $OA = a$ .

Hence the volume of the whole ellipsoid is obtained as follows:

$$\begin{aligned} V &= 8 \int_0^a \int_0^{b\sqrt{1-(x^2/a^2)}} \int_0^{c\sqrt{1-(x^2/a^2)-(y^2/b^2)}} dx dy dz \\ &= 8 \int_0^a dx \int_0^{b\sqrt{1-(x^2/a^2)}} dy \left| z \right|_0^{c\sqrt{1-(x^2/a^2)-(y^2/b^2)}} \\ &= 8c \int_0^a dx \int_0^{b\sqrt{1-(x^2/a^2)}} \sqrt{1-(x^2/a^2)-(y^2/b^2)} dy \\ &= \frac{8c}{b} \int_0^a dx \int_0^\rho \sqrt{(\rho^2 - y^2)} dy ; \text{ when } \rho = b\sqrt{1-(x^2/a^2)} \\ &= \frac{8c}{b} \int_0^a dx \left[ \frac{y\sqrt{(\rho^2 - y^2)}}{2} + \frac{\rho^2}{2} \sin^{-1} \frac{y}{\rho} \right]_0^\rho = \frac{8c}{b} \int_0^a \left( 1 - \frac{x^2}{a^2} \right) dx \\ &= 2\pi bc \int_0^a \left( 1 - \frac{x^2}{a^2} \right) dx = 2\pi bc \left| x - \frac{x^3}{3a^2} \right|_0^a = \frac{4abc}{3} \quad (\text{B.5}) \end{aligned}$$

## Appendix C. The proof of Eq. (2.32)

The equation for the perimeter of the ellipse is as follows:

$$p = 4a \int_0^{\pi/2} \sqrt{1 - \varepsilon^2 \sin^2 \theta} d\theta = 4a \int_0^{\pi/2} (1-x)^{1/2} d\theta \quad (C.1)$$

where  $x = \varepsilon^2 \sin^2 \theta$ ,  $n=1/2$ .

By using Binomial solution, perimeter of an ellipse is obtained approximately as follows:

$$(1-x)^n = 1 - nx + \frac{n(n-1)x^2}{2!} - \frac{n(n-1)(n-2)x^3}{3!} + \frac{n(n-1)(n-2)(n-3)x^4}{4!} - \frac{n(n-1)(n-2)(n-3)(n-4)x^5}{5!} + \frac{n(n-1)(n-2)(n-3)(n-4)(n-5)x^6}{6!} - \dots$$

$$(1-x)^n = 1 - nx + \frac{n(n-1)x^2}{2!} - \frac{n(n-1)(n-2)x^3}{3!} + \dots \quad (C.2)$$

Using Eq. (C.2), the equation for the perimeter of the ellipse Eq. (C.1) is written as follows:

$$p = 4a \int_0^{\pi/2} (1 - \varepsilon^2 \sin^2 \theta)^{1/2} d\theta = S_1 + S_2 + S_3 + S_4 + \dots \quad (C.3)$$

$S_1$  is represented as follows:

$$S_1 = 4a \left[ \int_0^{\pi/2} d\theta \right] = 4a \left( \theta \Big|_0^{\pi/2} \right) = 2a(\pi - 0) = 2\pi a \quad (C.4)$$

$S_2$  is represented as follows:

$$\begin{aligned} S_2 &= 4a \left( -\frac{1}{2} \int_0^{\pi/2} (\varepsilon^2 \sin^2 \theta) d\theta \right) = 4a \left( -\frac{\varepsilon}{2} \int_0^{\pi/2} (\sin^2 \theta) d\theta \right) \\ &= 4a \left( -\frac{\varepsilon}{2} \int_0^{\pi/2} \left[ \frac{1 - \cos 2\theta}{2} \right] d\theta \right) = 4a \left( -\frac{\varepsilon}{4} \int_0^{\pi/2} (1 - \cos 2\theta) d\theta \right) \\ &= 4a \left( -\frac{\varepsilon^2}{4} \int_0^{\pi/2} (1) d\theta + \frac{\varepsilon^2}{4} \int_0^{\pi/2} \cos(2\theta) d\theta \right) \\ &= 4a \left( -\frac{\varepsilon^2}{4} \left( \theta \Big|_0^{\pi/2} \right) + \frac{\varepsilon^2}{4} \int_0^{\pi/2} \cos(2\theta) d\theta \right) \\ &= 4a \left( -\frac{\varepsilon^2}{4} \left( \frac{\pi}{2} - 0 \right) + \frac{\varepsilon^2}{4} \int_0^{\pi/2} \cos(2\theta) d\theta \right) \\ &= 4a \left( -\frac{\pi \varepsilon^2}{8} + \frac{\varepsilon^2}{4} \int_0^{\pi/2} \cos(2\theta) d\theta \right) \end{aligned} \quad (C.5)$$

Now integrate the second term of Eq. (C.5) by substituting

$$u = 2\theta, \quad du = 2d\theta, \quad \text{then } d\theta = \frac{du}{2}.$$

Change limits:

$$\text{When } \theta = 0, \quad u = 2(0) = 0.$$

$$\text{When } \theta = \frac{\pi}{2}, \quad u = 2\left(\frac{\pi}{2}\right) = \pi.$$

Substituting to the above forms into the second item of Eq. (C.5) and taking integral yield:

$$\frac{\varepsilon^2}{4} \int_0^{\pi/2} \cos(2\theta) d\theta = \frac{\varepsilon^2}{4} \int_0^{\pi} \frac{\cos(u)}{2} du = \frac{\varepsilon^2}{8} (\sin(\pi) - \sin(0)) = 0 \quad (\text{C.6})$$

Eq. (C.5) becomes as follows:

$$S_2 = 4a \left( -\frac{\pi\varepsilon^2}{8} + 0 \right) = 2\pi a \left( -\frac{\varepsilon^2}{4} \right) = 2\pi a \left( -\frac{\varepsilon^2}{(1)} \left( \frac{1}{2} \right)^2 \right) \quad (\text{C.7})$$

$S_3$  is represented as follows:

$$\begin{aligned} S_3 &= 4a \left( \frac{\frac{1}{2} \left( \frac{1}{2} - 1 \right) \int_0^{\pi/2} (\varepsilon^2 \sin^2 \theta)^2 d\theta}{2!} \right) \\ &= 4a \left( \frac{\frac{1}{2} \left( \frac{1}{2} - 1 \right) \int_0^{\pi/2} (\varepsilon^2 \sin^2 \theta)^2 d\theta}{2!} \right) \\ &= 4a \left( \left( \frac{-\varepsilon^4}{8} \right) \int_0^{\pi/2} ((\sin^2 \theta))^2 d\theta \right) \end{aligned} \quad (\text{C.8})$$

$$\begin{aligned} (\sin^2 \theta)^2 &= \left( \frac{1 - \cos(2\theta)}{2} \right)^2 \\ &= \left( \frac{1 - \cos(2\theta)}{2} \right) \left( \frac{1 - \cos(2\theta)}{2} \right) \\ &= \left( \frac{1 - 2\cos(2\theta) + \cos^2(2\theta)}{4} \right) \end{aligned} \quad (\text{C.9})$$

Substituting Eq. (C.9) into Eq. (C.8),  $S_3$  becomes as follows:

$$S_3 = 4a \left( \left( -\frac{\varepsilon^4}{8} \right) \left( \frac{1}{4} \right) \int_0^{\pi/2} (1 - 2\cos(2\theta) + \cos^2(2\theta)) d\theta \right) \quad (\text{C.10})$$

In Eq. (C.10), the following is obtained as:

$$\int_0^{\pi/2} \cos(2\theta) d\theta = 2 \left[ \frac{\sin 2\theta}{2} \right]_0^{\pi/2} = 0 \quad (\text{C.11})$$

Therefore, Eq. (C.10) becomes:

$$\begin{aligned} S_3 &= 4a \left( \left( -\frac{\varepsilon^4}{8} \right) \left( \frac{1}{4} \right) \int_0^{\pi/2} (1 + \cos^2(2\theta)) d\theta \right) \\ &= 4a \left( \left( -\frac{\varepsilon^4}{8} \right) \left( \frac{1}{4} \right) \int_0^{\pi/2} \left( 1 + \frac{\cos(4\theta) + 1}{2} \right) d\theta \right) \\ &= 4a \left( \left( -\frac{\varepsilon^4}{8} \right) \left( \frac{1}{4} \right) \left( \frac{1}{2} \right) \int_0^{\pi/2} (3 + \cos(4\theta)) d\theta \right) \end{aligned} \quad (\text{C.12})$$

Let  $u = 4\theta$ ,  $du = 4d\theta$  then  $d\theta = \frac{du}{4}$ .

Change limits:

When  $\theta = 0$ ,  $u = 4(0) = 0$

When  $\theta = \frac{\pi}{2}$ ,  $u = 4\left(\frac{\pi}{2}\right) = 2\pi$

$$S_3 = 4a \left( \left( -\frac{\varepsilon^4}{8} \right) \left( \frac{1}{4} \right) \left( \frac{1}{2} \right) \left( \int_0^{\pi/2} 3d\theta + \left( \frac{1}{4} \right) \int_0^{2\pi} \cos u du \right) \right) \quad (\text{C.13})$$

where  $\int_0^{2\pi} \cos u du = 0$

$$\begin{aligned}
S_3 &= 4a \left( \left( -\frac{\varepsilon^4}{8} \right) \left( \frac{1}{4} \right) \left( \frac{1}{2} \right) \left( \int_0^{\pi/2} 3d\theta \right) \right) \\
&= 4a \left( \left( -\frac{\varepsilon^4}{8} \right) \left( \frac{1}{4} \right) \left( \frac{1}{2} \right) (3\theta) \Big|_0^{\pi/2} \right) \\
&= 4a \left( \left( -\frac{\varepsilon^4}{8} \right) \left( \frac{1}{4} \right) \left( \frac{1}{2} \right) \left( 3 \frac{\pi}{2} - 0 \right) \right) \\
&= 2\pi a \left( \left( \frac{-\varepsilon^4}{64} \right) (3) \right) \\
&= 2\pi a \left( \left( \frac{-\varepsilon^4}{3} \right) \left( \frac{1*3}{2*4} \right)^2 \right)
\end{aligned} \tag{C.14}$$

$S_4$  is represented as follows:

$$\begin{aligned}
S_4 &= 4a \left( \frac{\left( \frac{-1}{2} \left( \frac{1}{2} - 1 \right) \right) \left( \frac{1}{2} - 2 \right) \int_0^{\pi/2} (\varepsilon^2 \sin^2 \theta)^3 d\theta}{3!} \right) \\
&= 4a \left( \frac{\left( \frac{-3}{8} \right) \int_0^{\pi/2} (\varepsilon^2 \sin^2 \theta)^3 d\theta}{6} \right) \\
&= 4a \left( \left( \frac{-\varepsilon^6}{16} \right) \int_0^{\pi/2} (\sin^2 \theta)^3 d\theta \right)
\end{aligned} \tag{C.15}$$

$$\begin{aligned}
(\sin^2 \theta)^3 &= \left( \frac{1 - \cos(2\theta)}{2} \right)^3 = \left( \frac{1 - \cos(2\theta)}{2} \right)^2 \left( \frac{1 - \cos(2\theta)}{2} \right) \\
&= \left( \frac{1 - 2\cos(2\theta) + \cos^2(2\theta)}{4} \right) \left( \frac{1 - \cos(2\theta)}{2} \right) \\
&= \left( \frac{1}{8} \right) (1 - 2\cos(2\theta) + \cos^2(2\theta)) (1 - \cos(2\theta)) \quad (C.16) \\
&= \left( \frac{1}{8} \right) (1 - 2\cos(2\theta) + \cos^2(2\theta) \\
&\quad - \cos(2\theta) + 2\cos^2(2\theta) - \cos^3(2\theta)) \\
&= \left( \frac{1}{8} \right) (1 - 3\cos(2\theta) + 3\cos^2(2\theta) - \cos^3(2\theta))
\end{aligned}$$

Substituting Eq. (C.16) into Eq. (C.15),  $S_4$  yields:

$$\begin{aligned}
S_4 &= 4a \left( \left( \frac{-\varepsilon^6}{16} \right) \int_0^{\pi/2} (\sin^2 \theta)^3 d\theta \right) \\
&= 4a \left( \left( \frac{-\varepsilon^6}{16} \right) \left( \frac{1}{8} \right) \int_0^{\pi/2} (1 - 3\cos(2\theta) + 3\cos^2(2\theta) - \cos^3(2\theta)) d\theta \right) \\
&= 4a \left( \left( \frac{-\varepsilon^6}{16} \right) \left( \frac{1}{8} \right) \int_0^{\pi/2} (1 + 3\cos^2(2\theta) - \cos^3(2\theta)) d\theta \right) \quad (C.17)
\end{aligned}$$

where  $\int_0^{\pi/2} \cos(2\theta) d\theta = 0$ ,  $\int_0^{\pi/2} \cos(4\theta) d\theta = \frac{1}{4} [\sin 4\theta]_0^{\pi/2} = 0$

$$\begin{aligned}
\cos^3(2\theta) &= \cos^2(2\theta)\cos(2\theta) = \frac{1+\cos 4\theta}{2}\cos 2\theta \\
&= \frac{1}{2}\cos 2\theta + \frac{1}{2}\cos 4\theta\cos 2\theta \\
&= \frac{1}{2}\cos 2\theta + \frac{1}{2}\times\frac{1}{2}[\cos(4\theta+2\theta)+\cos(4\theta-2\theta)] \quad (\text{C.18}) \\
&= \frac{1}{2}\cos 2\theta + \frac{1}{4}(\cos 6\theta + \cos 2\theta) \\
&= \frac{3}{4}\cos 2\theta + \frac{1}{4}\cos 6\theta
\end{aligned}$$

$$\begin{aligned}
\int_0^{\pi/2} \cos^3(2\theta)d\theta &= \frac{3}{4}\int_0^{\pi/2} \cos(2\theta)d\theta + \frac{1}{4}\int_0^{\pi/2} \cos(6\theta)d\theta \\
&= \frac{3}{8}[\sin 2\theta]_0^{\pi/2} + \frac{1}{24}[\sin 6\theta]_0^{\pi/2} = 0
\end{aligned} \quad (\text{C.19})$$

From Eq. (C.19), Eq. (C.17) is reduced to:

$$\begin{aligned}
S_4 &= 4a\left(\left(\frac{-\varepsilon^6}{128}\right)\left(\int_0^{\pi/2} d\theta\right) + \left(\frac{3}{2}\right)\left(\int_0^{\pi/2} (\cos(4\theta)+1) d\theta\right)\right) \\
&= 4a\left(\left(\frac{-\varepsilon^6}{128}\right)\left(\int_0^{\pi/2} (1) d\theta\right) + \left(\frac{3}{2}\right)\left(\int_0^{\pi/2} (1) d\theta\right)\right) \\
&= 4a\left(\left(\frac{-\varepsilon^6}{128}\right)\left((\theta)_0^{\pi/2}\right) + \left(\frac{3}{2}\right)\left((\theta)_0^{\pi/2}\right)\right) \\
&= 4a\left(\left(\frac{-\varepsilon^6}{128}\right)\left(\frac{\pi}{2}-0\right) + \left(\frac{3}{2}\right)\left(\frac{\pi}{2}-0\right)\right) \\
&= 4a\left(\left(\frac{-\varepsilon^6}{128}\right)\left(\frac{5\pi}{4}\right)\right) = 2\pi a\left(\left(\frac{-\varepsilon^6}{128}\right)\left(\frac{5}{2}\right)\right) \\
&= 2\pi a\left(\left(\frac{-\varepsilon^6}{1}\right)\left(\frac{5}{256}\right)\right) = 2\pi a\left(\left(\frac{-\varepsilon^6}{5}\right)\left(\frac{1*3*5}{2*4*6}\right)^2\right) \quad (\text{C.20})
\end{aligned}$$

Therefore, perimeter of an ellipse of Eq. (C.3), Eq. (C.9), Eq. (C.14), and Eq. (C.20), is obtained as follows:

$$p = 2\pi a \left[ 1 - \frac{\varepsilon^2}{(1)} \left( \frac{1}{2} \right)^2 - \left( \frac{\varepsilon^4}{3} \right) \left( \frac{1*3}{2*4} \right)^2 - \left( \frac{\varepsilon^6}{5} \right) \left( \frac{1*2*5}{2*4*6} \right)^2 + \dots \right] \quad (C.21)$$

$$\varepsilon = \text{eccentricity} = \sqrt{1 - \left( \frac{b^2}{a^2} \right)}$$

Adding higher terms in Eq. (C.21) yields:

$$p = 2\pi a \left[ 1 - \frac{\varepsilon^2}{(1)} \left( \frac{1}{2} \right)^2 - \left( \frac{\varepsilon^4}{3} \right) \left( \frac{1*3}{2*4} \right)^2 - \left( \frac{\varepsilon^6}{5} \right) \left( \frac{1*3*5}{2*4*6} \right)^2 - \left( \frac{\varepsilon^8}{7} \right) \left( \frac{1*3*5*7}{2*4*6*8} \right)^2 - \left( \frac{\varepsilon^{10}}{9} \right) \left( \frac{1*3*5*7*9}{2*4*6*8*10} \right)^2 - \dots \right] \quad (C.22)$$

For a normalized ellipse, the following equations is reduced as:

$$\varepsilon^2 = 1 - \frac{b^2}{a^2} = 1 - \frac{(1-h)^2}{(1+h)^2} = \frac{4h}{(1+h)^2} \quad \text{and} \quad h = \frac{a-b}{a+b} \quad (C.23)$$

The Gauss-Kummer series [77] of ellipse perimeter via the intuitive approximation scheme is outlined as follows:

$$p = \pi(a+b) \left[ 1 + \left( \frac{1}{2} \right)^2 h^2 + \left( \frac{1}{2*4} \right)^2 h^4 + \left( \frac{1*3}{2*4*6} \right)^2 h^6 + \left( \frac{1*3*5}{2*4*6*8} \right)^2 h^8 + \dots \right] \quad (C.24)$$

By analogy with the radius of the circle, the effective radius of the ellipse is defined as  $r = p / 2\pi$ . Two natural estimates for  $r$  are linear mean  $r_1$  and quadratic mean  $r_2$  of semi-axes as follows:

$$r_1 = \frac{a+b}{2}, \quad r_2 = \left( \frac{a^2 + b^2}{2} \right)^{1/2} \quad (\text{C.25})$$

By using examples of  $a=4/3$  and  $b=2/3$ , the values of  $r$  are shown in Table C.1

Since  $r_1$  underestimates  $r$  and  $r_2$  overestimates  $r$  in Table C.1, their linear mean  $r_3$  and quadratic mean  $r_4$  are retrieved as follows:

$$r_3 = \frac{r_1 + r_2}{2}, \quad r_4 = \left( \frac{r_1^2 + r_2^2}{2} \right)^{1/2} \quad (\text{C.26})$$

Both  $r_3$  and  $r_4$  are underestimated in Table C.1.

Instead of dealing with linear and quadratic means, next consider the 3/2 mean as

$$r' = \left( \frac{a^{3/2} + b^{3/2}}{2} \right)^{2/3} \quad (\text{C.27})$$

Table C.1 Values of  $r$  for  $a=4/3$  and  $b=2/3$

Effective Radius	Values
$r_1$	1.02797628
$r_2$	1.05409255
$r_3$	1.02704628
$r_4$	1.02740233
$r'$	1.02778514

As shown in Table C.1 that  $r'$  is underestimated, but it is better than the others (only about  $\frac{(r_1 - r')}{r'} \times 100\% = 0.0186\%$  less than  $r$ ).

To explore the  $3/2$  mean, the ellipse is normalized to be  $a+b=2$ . By setting  $a=1+h=4/3$  and  $b=1-h=2/3$  ( $h=1/3$ ). By averaging the binomial expansions  $(1+h)^{3/2}$  and  $(1-h)^{3/2}$ ,  $r'$  is obtained as follows:

$$\begin{aligned} r' &= \left( 1 + \frac{3}{8}h^2 + \frac{3}{128}h^4 + \frac{3}{1024}h^6 + \dots \right)^{2/3} \\ &= 1 + c_1h^2 + c_2h^4 + c_3h^6 + \dots \end{aligned} \quad (C.28)$$

where  $c_1, c_2, c_3$  are undetermined coefficients.

By cubing both sides of Eq. (C.23),  $c_1=1/4$ ,  $c_2=0$  and  $c_3=1/192$  are obtained. Hence

$$r' = 1 + \frac{1}{4}h^2 + \frac{1}{192}h^6 + \dots \quad (C.29)$$

$h^4$  term in  $r'$  is considered by adding the small difference between  $r(r_1, r_2, r_3, r_4)$  and  $r'$ . The difference is  $r-r' \cong k_1h^4$ . By using the data of C1 and  $h=1/3$ ,  $k_1 \cong 1/64.59$  is obtained. This is close enough to  $1/64$ , so it leads to the assumption that

$$r = r' + k_1h^4 = 1 + \frac{1}{4}h^2 + \frac{1}{64}h^4 + k_2h^6 + \dots \quad (C.30)$$

Repeating the numerical estimation,  $k_2 \cong 1/245$ , which is close to another perfect square,  $1/256$ . Thus, the refined assumption for the effective radius of a normalized ellipse is

$$r = 1 + \left(\frac{1}{2}\right)^2 h^2 + \left(\frac{1}{8}\right)^2 h^4 + \left(\frac{1}{16}\right)^2 h^6 + \dots \quad (\text{C.31})$$

The coefficients of Eq. (C.28) is recognized as the squares of the expansion of  $(1+x)^{1/2}$ .

Considering the fifth term Eq. (C.31), the following equation can be obtained as:

$$r = 1 + \left(\frac{1}{2}\right)^2 h^2 + \left(\frac{1}{8}\right)^2 h^4 + \left(\frac{1}{16}\right)^2 h^6 + \left(\frac{1}{128}\right)^2 h^8 + \dots \quad (\text{C.32})$$

Without normalization, the following equation can be obtained as:

$$p = \pi(a+b) \left\{ 1 + \frac{1}{4}h^2 + \frac{1}{64}h^4 + \frac{1}{256}h^6 + \frac{1}{16,384}h^8 + \dots \right\} \quad (\text{C.33})$$

$$\approx \pi(a+b) \left[ 1 + \left(\frac{1}{2}\right)^2 h^2 \right]$$